UNIVERSITY OF CALIFORNIA
SANTA CRUZ

IMPACTS OF OXYGEN VACANCIES IN TITANIUM DIOXIDE-SUPPORTED METAL NANOPARTICLES IN THE OXYGEN REDUCTION REACTION AND THE CARBON ELECTROOXIDATION REACTION

A dissertation submitted in partial satisfaction
of the requirements for the degree of

DOCTOR OF PHILOSOPHY

In

CHEMISTRY

by

Samantha Sweeney

December 2018

The Dissertation of Samantha Sweeney is approved:

_____
Professor Shaowei Chen, Advisor

_____
Professor Ilan Benjamin, Chair

_____
Professor Jin Zhang

_____
Lori Kletzer
Vice Provost and Dean of Graduate Studies

Table of Contents

Chapter 6. Summary and Outlook

List of Figures

List of Tables

Abstract

Impacts of oxygen vacancies in titanium dioxide-supported metal nanoparticles in the oxygen reduction reaction and the carbon electrooxidation reaction

by

Samantha Sweeney

With the current energy demands, the burning of fossil fuels is causing many issues, such as global warming, therefore many researchers are looking into replacing the current methods with electrical energy storage devices. One such device is the fuel cell, where the oxidized fuel provides energy to power things, such as cars. However, the reaction in the cathode compartment, the oxygen reduction reaction (ORR), has driven up the price of the fuel cell due to the high catalyst loading needed to achieve efficiencies suitable for industry. In addition, the most common commercial catalyst is platinum nanoparticles deposited on activated carbon nanoparticles. Platinum is rare and expensive and the major contributor to the high cost. The platinum nanoparticles can also detach, move, or change size dependent on reaction conditions. Finally, platinum is easily poisoned by carbon monoxide. Improving platinum's tolerance for CO will be discussed in chapter 5. The activated carbon nanoparticles are not stable at the operation voltage of fuel cells and therefore constant catalyst replacement lowers their recyclability and shelf-life. Therefore, an alternative to this system is needed.

Transition-metal oxides offer an interesting alternative to the activated carbon because of their stability. TiO_2 in particular is abundant and relatively inexpensive.

However, due to its semiconducting properties, it has poor activity for electrochemical reactions. The activity can be enhanced with the deposition of nanoparticles, specifically gold due to the strong metal support interactions. However, this is still not sufficient to replace platinum. The creation of oxygen vacancies in titanium dioxide can influence the binding energy of oxygen and the activity of the overall nanocomposite. Their impact is discussed in chapters 2 and 3. Finally, the activity can be altered by doping the TiO_2 and in chapter 4 nitrogen doping will be discussed. Overall, these defects will be explored throughout this dissertation and how the kinetics of electrochemical reactions will be affected.

Dedication

To my fiancé

David Mori

your support over the years has been the driving force for this work

and to my parents and sister

Dennis Sweeney, Linda Sweeney, and Alexandra Sweeney

for teaching me to follow my dreams

and to Jesus my personal savior

through whom of all of this is made possible.

Acknowledgement

I would first like to acknowledge the members of my dissertation committee. First, my advisor Professor Shaowei Chen for giving me the idea to start this work, for showing me how awesome electrochemistsry is, his mentorship throughout these projects, and for the external experiences I would not have gotten anywhere else. I would also like to thank Professor Ilan Benjamin for chairing my dissertation committee. Finally, I would like to thank Professor Jin Zhang for encouraging me to pursue research that would give me the best training in my future steps.

A big thanks to the members of the Chen lab, past and present for all the laughter and mentorship. A big thanks to Chris Deming for teaching me all that I know now about these projects and for doing XPS and TEM work for some of the projects. Thank you to Gabby Lu for doing the rest of the TEM work for these projects. XPS and TEM were done at Molecular Foundry of the Lawrence Berkeley National Laboratory and the National Center for Electron Microscopy respectively. Thank you to Graham Roseman for his assistance in EPR, Al'Lester Allen for his assistance in Raman, and Jesse Hauser for his assistance in XRD.

Finally, thank you to my cohort, the Zhang lab, the Ayzner lab, and the Oliver lab for the laughs, support, and inspiration.

Chapter 1

Current Fuel Cell Catalyst Research and the Degradation of Carbon Support: Why TiO_2 is an Interesting Alternative

1.1 Fuel Cell Operation and Bottleneck of ORR

With ever increasing energy demands, there has been extensive research on more sustainable devices. One of such devices is the fuel cell; a device that converts a fuel directly into electrical energy as opposed to combustion devices that go through multi-step conversions and release harmful byproducts. In this process, the fuel is passed through the anode where it is oxidized, and the electron are released to power something. Finally the electrons will flow back to the cathode where they will reduce oxygen into water.[1]

There are several types of fuel cells each being classified by the electrolyte and operation temperature. Alkaline fuel cells employ the use of KOH as the electrolyte and operate below 100°C. These fuel cells have been used in space, especially in the Apollo missions. Polymer electrolyte fuel cells have a proton exchange membrane as their electrolyte. These operate in the temperature range of 60-120°C and were the first to be used in space. The direct methanol fuel cell is a subset of the polymer electrolyte fuel cell (PEMFC), but with methanol as the fuel and slightly higher operation temperatures. The phosphoric acid fuel cells have phosphoric acid as their electrolyte and have been the most commercialized being used in stationary power plants. The

molten carbonate fuel cell operates at a much higher temperature with LiK or LiNa carbonate as the electrolyte. Because of the high temperature, the kinetics of the electrochemical reactions are much faster and poisoning byproducts are not as common since they don't bind to the surface too strongly. Finally the solid oxide fuel cell involves a solid oxide as the electrolyte also operating at high temperatures.[2]

Polymer electrolyte fuel cells in particular are an interesting option because they operate at lower temperatures, they have high power densities, and they have an easy scale-up which is important for industrial applications. Currently, they are used in transportation, stationary power generation, and portable power generation. Transportation has become an important area to use fuel cells because of the potential of lower gas emissions when hydrogen is used as the fuel. Honda, Mercedes, Toyota, Hyundai, and Riversimple all have models on the market. However, over time the polymer membrane degrades causing the device lifetime to decrease. In addition, the cost of the fuel cell remains high because of the large amount of platinum catalyst needed to have the fuel cell run efficiently.[3] Figure 1.1 shows a projection chart from the DOE. While there has been significant progress in this area, there still needs to be improvement. This improvement comes from reducing the cost of the catalysts in fuel cell reactions.

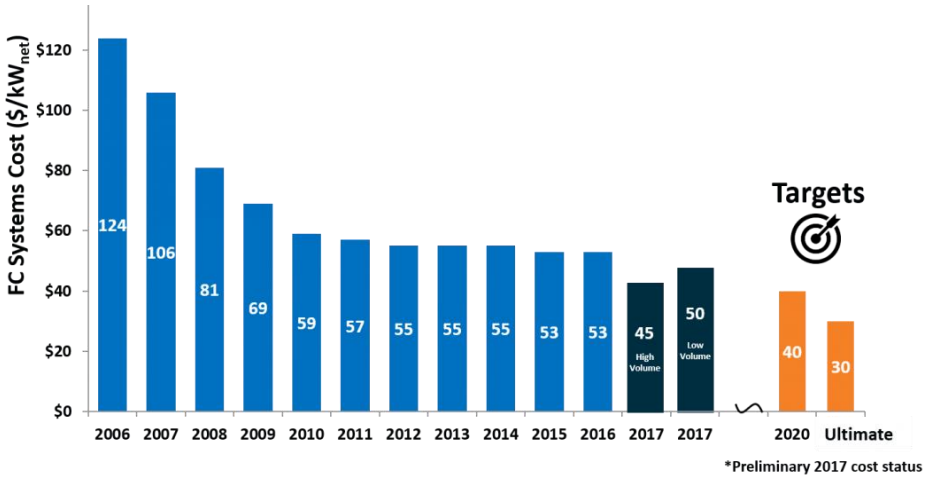

Figure 1.1 Modulated fuel cell system cost over time. Taken from *DOE Hydrogen and Fuel Cells Program Record 17007: Fuel Cell System Cost—2017*.

In Figure 1.2, a schematic is shown with the reactions that occur in PEMFC's. First, hydrogen gas is injected into the anode compartment where it is oxidized. The resulting electrons are used for electrical energy and the protons travel across the membrane into the cathode compartment. The two combine in the cathode compartment where the electrons will reduce oxygen into water. In Equation 1.1, the hydrogen oxidation reaction is shown.

$$\tfrac{1}{2}\,H_2 + * \rightarrow H^* \qquad (1.1)$$

(* denotes a surface site)

The main catalyst for this reaction is platinum, with very fast kinetics. A major breakthrough with decreasing the loading for the anode is using platinum nanoparticles

where the voltage loss is less than 5 mV for a loading of 0.05 mg/cm^2. Therefore, much of the research is devoted to the cathode reaction, the oxygen reduction reaction (ORR).[4,5] In this reaction, more much platinum is needed to produce comparable efficiencies to internal combustion engines. However, as stated earlier, this drives the overall cost of the fuel cell up. Another problem is that platinum has a very low abundance and mass production of this metal would deplete available resources and cause for costly recycling processes. Finally, the reaction has a complex mechanism making alternative sources to platinum harder to find. The overall equation for the ORR is shown in Equation 1.2

$$2O_2 + 4e^- + 4H^+ \rightarrow 2H_2O \qquad (1.2)$$

Overall, this reaction has 4 electron transfer steps with two main pathways: the direct pathway where O_2 is directly converted to water and a series of 2 electron transfer steps with hydrogen peroxide as a byproduct. In general the direct pathway is favored because hydrogen peroxide degrades catalysts and the membrane and decreases the overall potential output of the cell.[6]

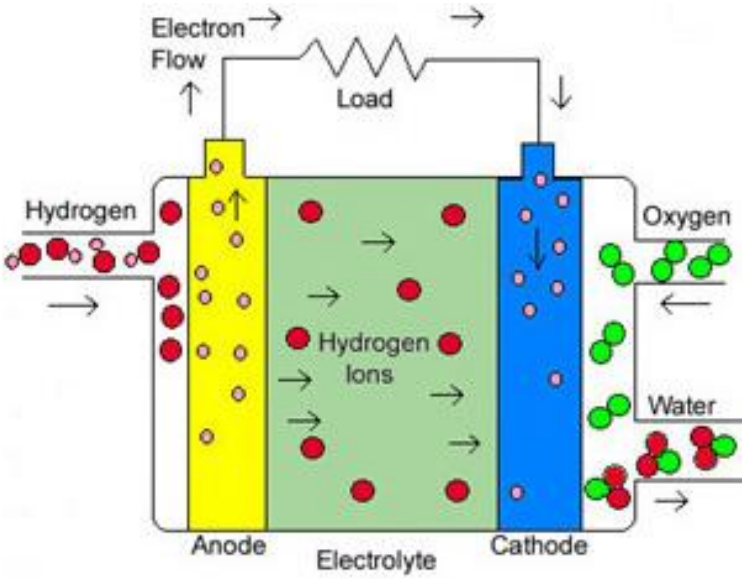

Figure 1.2 Schematic of reactions that occur polymer electrolyte membrane fuel cells. Taken from http://americanhistory.si.edu/fuelcells/basics.htm

1.2 Degradation of carbon black and use of TiO_2 in ORR

To enhance the kinetics for the ORR, platinum nanoparticles are deposited onto a high surface area support to enhance conductivity. Typically, carbon black is used as the support in current fuel cell devices. Two problems have become apparent with carbon black as the support. 1) At the operation voltage, platinum dissolution occurs decreasing the cell overall potential. 2) The carbon black support has been shown to be unstable and cause loss in electrochemical surface area over time. Carbon black instability is shown in conversion of the carbon to carbon dioxide and detachment of platinum nanoparticles.[7] These mechanisms are further shown in Figure 1.3. In Chapter 4, more detail will be given to catalyst degradation by carbon monoxide.

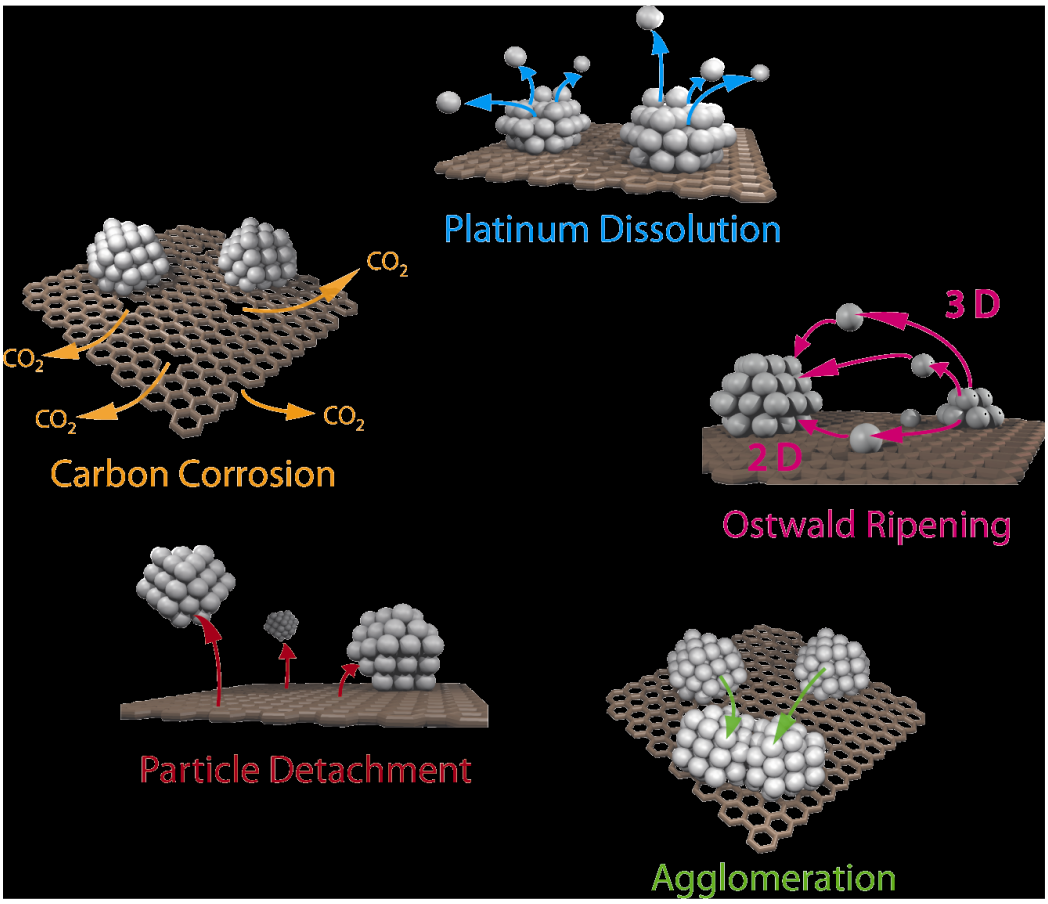

Figure 1.3 Simplified representation of suggested degradation mechanisms for platinum particles on a carbon support in fuel cells.[8]

There have been some studies replacing carbon black with other carbon-based supports. In a study done by Molina-Garcia and Rees, $NaBH_4$ was used to reduce platinum nanoparticles on carbon black, multi-walled carbon nanotubes, graphene oxide, and reduced graphene oxide. Their goal was to understand the performance of all the supports on platinum nanoparticles for the ORR. Overall, the results showed that platinum nanoparticles deposited on carbon black showed the best activity

because of the most positive onset potential, most positive half wave potential, highest electrons transferred, highest electrochemical surface area, and highest kinetic current. In addition, on the other supports, the surface groups seem to affect the ORR activity.[9] Therefore, finding an alternative to the carbon support important to enhance the kinetics of the ORR.

TiO_2 is an interesting candidate because of its stability and high abundance. It has also been looked at as a catalyst alone. In a study done by Mirshekari and Shirvanian, TiO_2 nanoparticles of different sizes were studied as electrocatalysts for the ORR. The smaller particles seemed to have higher amounts of aggregation due to their higher surface energies. Because of this the nanoparticles with 30 nm diameters seemed have the highest activity. The biggest draw to these particles were their stability. The particles were cycled 5000 times and the ORR currents increased.[10] In another study done by Cabello and coworkers, used a facile method, one that takes 20 s, to synthesize anatase TiO_2 nanoparticles. With this synthesis method, they controlled monodispersity in particle size and synthesis yield. The particles were then deposited on graphite electrodes and used as catalysts for the oxygen reduction reaction. These particles showed good activity for hydrogen peroxide production.[11]

A problem is using TiO_2 as a catalyst for the ORR because of its low conductivity due its semiconductor properties. An enhancement of the activity can be done by the deposition of metal nanoparticles onto TiO_2 creating a strong-metal-support-interaction (SMSI).[12] Ando et al. deposited platinum nanoparticles onto titanium dioxide matrix in cup-stacked carbon nanotubes (Pt NPs/TiO_2/CSCNT). This

nanocomposite was then used as a catalyst for the ORR. It was shown that the strong SMSIs between the Pt and TiO_2 enhanced the activity and durability of the catalyst compared to that of CSCNTs only as a support.[13] In another study done by Deng and coworkers, PtAu alloy nanoparticles were deposited onto TiO_2 nanowires and the nanocomposite was coated with a carbon shell. This combined structure proved to be more stable and more active than Pt/C because of the SMSIs and the altering of the d-band with gold.[14]

1.3 Oxygen Vacancies in TiO_2

The structure of oxygen vacancies in the crystal structure of TiO_2 is shown in Figure 1.4. The vacancy is represented by an oxygen missing from the crystal lattice. The extra electrons are donated to the adjacent Ti^{4+} to create Ti^{3+} interstitials. Oxygen vacancies have been used to further enhance the ORR and other reactions by changing the properties of TiO_2 especially in photocatalysis.[15] In this section, I will summarize current synthesis methods of introducing oxygen vacancies into TiO_2 and resulting properties of TiO_2. Then in Chapter 3, the effects on electrocatalytic activity towards the ORR will be looked into.

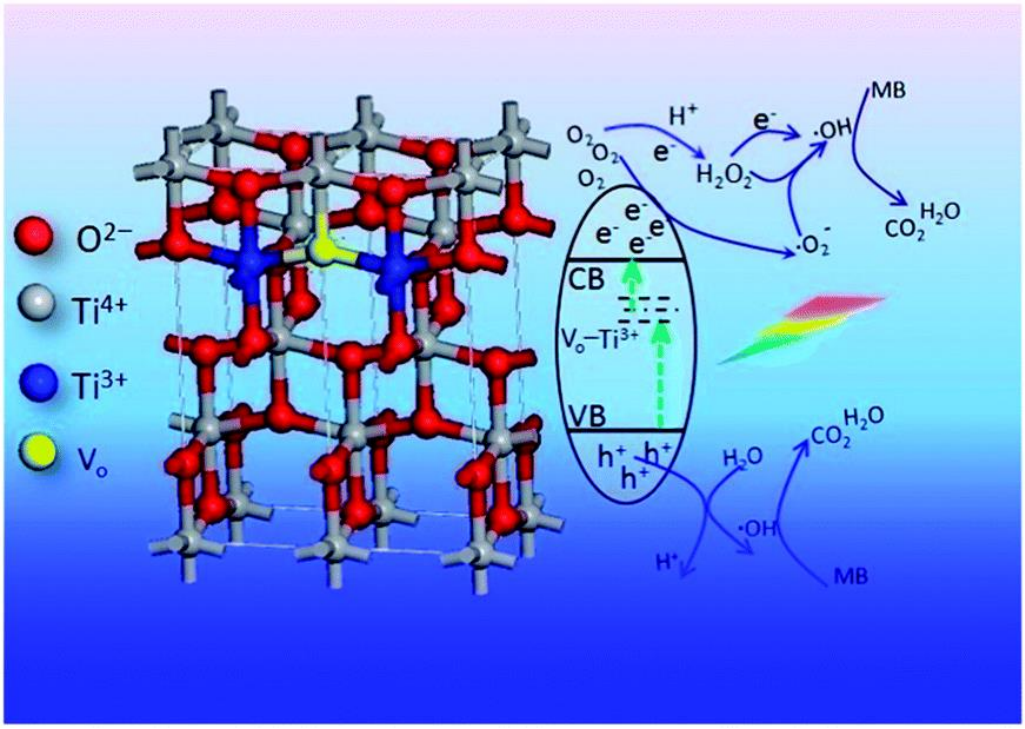

Figure 1.4 Illustration of the energy bands for Ti^{3+} self-doped TiO_{2-x} with high oxygen vacancy concentration and the photoinduced charge transfer processes.[16]

1.3.1 Synthetic Approaches to Produce Oxygen Vacancies in TiO_2

(i) Hydrogen Thermal Treatment. Several groups have used H_2 to reduce the surface of TiO_2 to create oxygen vacancies.[17-22] In this method, the as prepared TiO_2 is heated to a certain temperature in a hydrogen atmosphere and surface oxygen atoms are removed thus creating oxygen vacancies. In a study done by Liu et al., the temperature of the hydrogen treatment was changed from 120 – 700 °C and the degradation of sulfosalicylic acid was studied. The temperature seemed to have an effect on photocatalytic activity and the mechanistic formation of the oxygen vacancies.[20] Morgan and Watson used theoretical calculations to compare the

formation of oxygen vacancies in anatase and rutile TiO_2. Overall, they found that oxygen vacancies are more easily formed in anatase TiO_2 than rutile TiO_2.[23]

(ii) High Energy Particle Bombardment. Another method employs high energy particles that preferentially desorb oxygen ions from TiO_2 surfaces. This method has been shown to preferentially form oxygen vacancies and minimizes damage to the surface when electrons are used as the particle source.[24-27] Ar^+ has also been used to create oxygen vacancies, but defects other than oxygen vacancies can be created and some of these defects are not at the surface. These kinds of defects tend to be irreversible.[28,29]

(iii) Formation During Catalytic and Photocatalytic Reactions. During catalysis, the surface oxygens of TiO_2 will participate in the reaction and cause an oxidation thereby causing a surface oxygen vacancy.[30-32] Panayotov and Morris were able to see an example of this by showing the burning of a methoxy group with a surface oxygen in the TiO_2, as shown in Figure 1.5.[30]

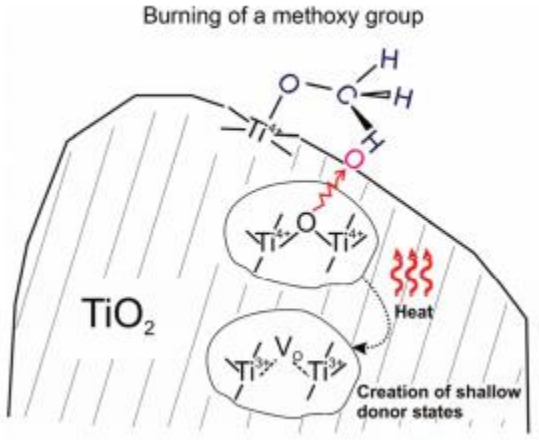

Figure 1.5 Schematic diagram illustrating thermally activated bridging lattice oxygen leaving behind Ti^{3+}-VO-Ti^{3+} donors. Reprinted with permission.[30]

(iv) Thermal Treatment under Oxygen Deficient Atmosphere. The final method that has been reported is annealing TiO_2 at higher temperatures (>400°C) in a low-oxygen environment (He, N_2, or Ar environment) or under vacuum. A problem with this method is that once the TiO_2 is exposed to air, the oxygen vacancies can slowly disappear.[28,33-35] Wu and van de Krol employed this facile method to study the selective photoreduction of NO to N_2. They found that further doping TiO_2 with Fe^{3+} can enhance the selectivity and stability of the oxygen vacancies.[36]

1.3.2 Properties of TiO_2 with Oxygen Vacancies

(i) Geometric structure. A missing oxygen in the lattice causes changes to the geometric structure. Because there is now a new "stress" on the structure, bonds will be shortened/lengthened to accommodate this new stress.[23,37] This has been shown in Raman[38] and electron diffraction results.[21]

(ii) Electronic structure. As shown before in Figure 1.4, an oxygen vacancy is characterized by a missing oxygen from the lattice of the TiO_2. This results in one or two electrons becoming localized by replacing the missing O^{2-} charge and thus stabilizing the structure.[39] In Figure 1.6, the band gap structure of TiO_2 with an oxygen vacancy is shown. A state forms below the conduction band allowing for a decrease in the band gap and thereby increasing photocatalytic activity and conductivity.[40] The

electrons can also localize around Ti forming Ti^{3+} states, thus creating energy states below conduction band. If there is some doping, the dopants can create states above the valence band.[41]

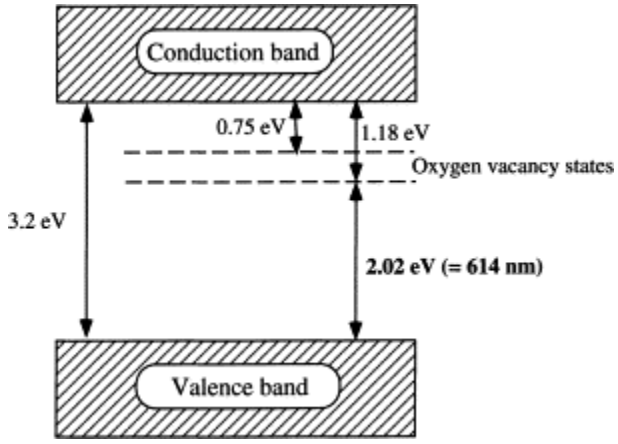

Figure 1.6 A proposed band structure model for the anatase TiO_2 with oxygen vacancies.[40] Reprinted with permission from Elsevier.

(iii) Optical Properties. As stated earlier, due to the wide band gap of TiO_2, this material can only absorb light in the UV-region. For certain applications, this is not helpful. When oxygen vacancies are introduced into TiO_2, local states are created below the conduction band (as shown in Figure 1.6) and thereby creating some absorption in the visible range. Ti^{3+} can also produce the same effect.[42]

(iv) O_2 adsorption. The creation of oxygen vacancies can affect the adsorption energy of certain probe molecules, for instance molecular oxygen. Oxygen does not easily adsorb onto a neutral TiO_2 surface. However, once oxygen vacancies are created, the surface becomes more negative thereby allowing for better adsorption of oxygen.[43]

1.4 Doping in TiO_2

Doping of TiO_2 is another way to alter the conductivity and thus change the activity of TiO_2.[44] In TiO_2, two different kinds of doping can happen: cation and anion doping. For cation doping, the Ti^{4+} is replaced by another metal. Domen and coworkers have shown that doping TiO_2 with a trivalent cation, facilitates the formation of oxygen vacancies without the formation of Ti^{3+} ions. In contrast, when Ti^{4+} is replaced with a pentavalent ion, Ti^{3+} is mainly formed instead of oxygen vacancies.[45] In anion doping, the O^{2-} is replaced by another heteroatom. Overall, this can alter the conductivity and band structure of TiO_2. More detail will be given in Chapter 4.

1.5 Summary

Fuel cells are a very interesting energy storage device that provide a competitive alternative to the car engine. However, their commercialization is bottlenecked due to sluggish kinetics of the oxygen reduction reaction. In addition, the breakdown of the activated carbon nanoparticle support drives up the cost of the fuel cell and lowers the overall efficiency of the fuel cell. An alternative support that has been proposed is TiO_2 because it is stable, cost effective, and abundant. However, because it is a semi-conductor, its lower conductivity to carbon causes it to perform worse than carbon. By creating oxygen vacancies and adding dopants to the TiO_2, the conductivity can be enhanced and therefore, the activity towards the oxygen reduction reaction can be

enhanced. This dissertation strives to understand the impact these defects play in electrochemical reactions.

1.6 References

(1) Sharaf, O. Z.; Orhan, M. F.: An overview of fuel cell technology: Fundamentals and applications. *Renew Sust Energ Rev* **2014**, *32*, 810-853.

(2) Carrette, L.; Friedrich, K. A.; Stimming, U.: Fuel Cells - Fundamentals and Applications. *Fuel Cells* **2001**, *1*, 5-39.

(3) Wang, Y.; Chen, K. S.; Mishler, J.; Cho, S. C.; Adroher, X. C.: A review of polymer electrolyte membrane fuel cells: Technology, applications, and needs on fundamental research. *Appl Energ* **2011**, *88*, 981-1007.

(4) Holton, O. T.; Stevenson, J. W.: The Role of Platinum in Proton Exchange Membrane Fuel Cells Evaluation of platinum's unique properties for use in both the anode and cathode of a proton exchange membrane fuel cell. *Platin Met Rev* **2013**, *57*, 259-271.

(5) Sheng, W. C.; Gasteiger, H. A.; Shao-Horn, Y.: Hydrogen Oxidation and Evolution Reaction Kinetics on Platinum: Acid vs Alkaline Electrolytes. *J Electrochem Soc* **2010**, *157*, B1529-B1536.

(6) Sui, S.; Wang, X. Y.; Zhou, X. T.; Su, Y. H.; Riffatc, S.; Liu, C. J.: A comprehensive review of Pt electrocatalysts for the oxygen reduction reaction: Nanostructure, activity, mechanism and carbon support in PEM fuel cells. *J Mater Chem A* **2017**, *5*, 1808-1825.

(7) Schonvogel, D.; Hulstede, J.; Wagner, P.; Kruusenberg, I.; Tammeveski, K.; Dyck, A.; Agert, C.; Wark, M.: Stability of Pt Nanoparticles on Alternative Carbon Supports for Oxygen Reduction Reaction. *J Electrochem Soc* **2017**, *164*, F995-F1004.

(8) Meier, J. C.; Galeano, C.; Katsounaros, I.; Witte, J.; Bongard, H. J.; Topalov, A. A.; Baldizzone, C.; Mezzavilla, S.; Schuth, F.; Mayrhofer, K. J. J.: Design criteria for stable Pt/C fuel cell catalysts. *Beilstein J Nanotech* **2014**, *5*, 44-67.

(9) Molina-Garcia, M. A.; Rees, N. V.: Effect of catalyst carbon supports on the oxygen reduction reaction in alkaline media: a comparative study. *Rsc Adv* **2016**, *6*, 94669-94681.

(10) Mirshekari, G. R.; Shirvanian, A. P.: Electrochemical behavior of titanium oxide nanoparticles for oxygen reduction reaction environment in PEM fuel cells. *Mater Today Energy* **2018**, *9*, 235-239.

(11) Cabello, G.; Davoglio, R. A.; Pereira, E. C.: Microwave-assisted synthesis of anatase-TiO_2 nanoparticles with catalytic activity in oxygen reduction. *J Electroanal Chem* **2017**, *794*, 36-42.

(12) Naldoni, A.; Riboni, F.; Marelli, M.; Bossola, F.; Ulisse, G.; Di Carlo, A.; Pis, I.; Nappini, S.; Malvestuto, M.; Dozzi, M. V.; Psaro, R.; Selli, E.; Dal Santo, V.: Influence of TiO_2 electronic structure and strong metal-support interaction on plasmonic Au photocatalytic oxidations. *Catal Sci Technol* **2016**, *6*, 3220-3229.

(13) Ando, F.; Tanabe, T.; Gunji, T.; Tsuda, T.; Kaneko, S.; Takeda, T.; Ohsaka, T.; Matsumoto, F.: Improvement of ORR Activity and Durability of Pt Electrocatalyst Nanoparticles Anchored on TiO_2/Cup-Stacked Carbon Nanotube in Acidic Aqueous Media. *Electrochim Acta* **2017**, *232*, 404-413.

(14) Deng, X. T.; Yin, S. F.; Wu, X. B.; Sun, M.; Xie, Z. Y.; Huang, Q. Z.: Synthesis of PtAu/TiO_2 nanowires with carbon skin as highly active and highly stable electrocatalyst for oxygen reduction reaction. *Electrochim Acta* **2018**, *283*, 987-996.

(15) Pan, X. Y.; Yang, M. Q.; Fu, X. Z.; Zhang, N.; Xu, Y. J.: Defective TiO_2 with oxygen vacancies: synthesis, properties and photocatalytic applications. *Nanoscale* **2013**, *5*, 3601-3614.

(16) Zhu, Q.; Peng, Y.; Lin, L.; Fan, C. M.; Gao, G. Q.; Wang, R. X.; Xu, A. W.: Stable blue TiO_2-x nanoparticles for efficient visible light photocatalysts. *J Mater Chem A* **2014**, *2*, 4429-4437.

(17) Chen, X. B.; Liu, L.; Yu, P. Y.; Mao, S. S.: Increasing Solar Absorption for Photocatalysis with Black Hydrogenated Titanium Dioxide Nanocrystals. *Science* **2011**, *331*, 746-750.

(18) Bagheri, S.; Julkapli, N. M.: Synergistic effects on hydrogenated TiO_2 for photodegradation of synthetic compounds pollutants. *Int J Hydrogen Energ* **2016**, *41*, 14652-14664.

(19) Jiang, X. D.; Zhang, Y. P.; Jiang, J.; Rong, Y. S.; Wang, Y. C.; Wu, Y. C.; Pan, C. X.: Characterization of Oxygen Vacancy Associates within Hydrogenated TiO_2: A Positron Annihilation Study. *J Phys Chem C* **2012**, *116*, 22619-22624.

(20) Liu, H.; Ma, H. T.; Li, X. Z.; Li, W. Z.; Wu, M.; Bao, X. H.: The enhancement of TiO_2 photocatalytic activity by hydrogen thermal treatment. *Chemosphere* **2003**, *50*, 39-46.

(21) Naldoni, A.; Allieta, M.; Santangelo, S.; Marelli, M.; Fabbri, F.; Cappelli, S.; Bianchi, C. L.; Psaro, R.; Dal Santo, V.: Effect of Nature and Location of Defects on Bandgap Narrowing in Black TiO_2 Nanoparticles. *J Am Chem Soc* **2012**, *134*, 7600-7603.

(22) Wang, G. M.; Wang, H. Y.; Ling, Y. C.; Tang, Y. C.; Yang, X. Y.; Fitzmorris, R. C.; Wang, C. C.; Zhang, J. Z.; Li, Y.: Hydrogen-Treated TiO_2 Nanowire Arrays for Photoelectrochemical Water Splitting. *Nano Lett* **2011**, *11*, 3026-3033.

(23) Morgan, B. J.; Watson, G. W.: Intrinsic n-type Defect Formation in TiO_2: A Comparison of Rutile and Anatase from GGA plus U Calculations. *J Phys Chem C* **2010**, *114*, 2321-2328.

(24) Wang, L. Q.; Baer, D. R.; Engelhard, M. H.; Shultz, A. N.: The adsorption of liquid and vapor water on TiO_2(110) surfaces: The role of defects. *Surf Sci* **1995**, *344*, 237-250.

(25) Eriksen, S.; Egdell, R. G.: Electronic Excitations at Oxygen Deficient TiO_2(110) Surfaces - a Study by Eels. *Surf Sci* **1987**, *180*, 263-278.

(26) Feibelman, P. J.; Knotek, M. L.: Reinterpretation of Electron-Stimulated Desorption Data from Chemisorption Systems. *Phys Rev B* **1978**, *18*, 6531-6539.

(27) Knotek, M. L.; Feibelman, P. J.: Ion Desorption by Core-Hole Auger Decay. *Phys Rev Lett* **1978**, *40*, 964-967.

(28) Thompson, T. L.; Yates, J. T.: TiO_2-based photocatalysis: Surface defects, oxygen and charge transfer. *Top Catal* **2005**, *35*, 197-210.

(29) Onda, K.; Li, B.; Petek, H.: Two-photon photoemission spectroscopy of TiO_2(110) surfaces modified by defects and O-2 or H2O adsorbates. *Phys Rev B* **2004**, *70*.

(30) Panayotov, D. A.; Morris, J. R.: Thermal Decomposition of a Chemical Warfare Agent Simulant (DMMP) on TiO_2: Adsorbate Reactions with Lattice Oxygen as Studied by Infrared Spectroscopy. *J Phys Chem C* **2009**, *113*, 15684-15691.

(31) Vedrine, J. C.; Coudurier, G.; Millet, J. M. M.: Molecular design of active sites in partial oxidation reactions on metallic oxides. *Catal Today* **1997**, *33*, 3-13.

(32) Wachs, I. E.; Jehng, J. M.; Ueda, W.: Determination of the chemical nature of active surface sites present on bulk mixed metal oxide catalysts. *J Phys Chem B* **2005**, *109*, 2275-2284.

(33) Nowotny, M. K.; Sheppard, L. R.; Bak, T.; Nowotny, J.: Defect chemistry of titanium dioxide: application of defect engineering in processing of TiO_2-based photocatalysts. *J Phys Chem C* **2008**, *112*, 5275-5300.

(34) Liu, L. J.; Zhao, C. Y.; Li, Y.: Spontaneous Dissociation of CO_2 to CO on Defective Surface of Cu(I)/TiO_2-x Nanoparticles at Room Temperature. *J Phys Chem C* **2012**, *116*, 7904-7912.

(35) Wu, Q. P.; Zheng, Q.; van de Krol, R.: Creating Oxygen Vacancies as a Novel Strategy To Form Tetrahedrally Coordinated Ti^{4+} in Fe/TiO_2 Nanoparticles. *J Phys Chem C* **2012**, *116*, 7219-7226.

(36) Wu, Q. P.; van de Krol, R.: Selective Photoreduction of Nitric Oxide to Nitrogen by Nanostructured TiO2 Photocatalysts: Role of Oxygen Vacancies and Iron Dopant. *J Am Chem Soc* **2012**, *134*, 9369-9375.

(37) Janotti, A.; Varley, J. B.; Rinke, P.; Umezawa, N.; Kresse, G.; Van de Walle, C. G.: Hybrid functional studies of the oxygen vacancy in TiO_2. *Phys Rev B* **2010**, *81*.

(38) Parker, J. C.; Siegel, R. W.: Raman Microprobe Study of Nanophase TiO_2 and Oxidation-Induced Spectral Changes. *J Mater Res* **1990**, *5*, 1246-1252.

(39) Pacchioni, G.: Oxygen vacancy: The invisible agent on oxide surfaces. *Chemphyschem* **2003**, *4*, 1041-1047.

(40) Nakamura, I.; Negishi, N.; Kutsuna, S.; Ihara, T.; Sugihara, S.; Takeuchi, E.: Role of oxygen vacancy in the plasma-treated TiO_2 photocatalyst with visible light activity for NO removal. *J Mol Catal a-Chem* **2000**, *161*, 205-212.

(41) Liu, G.; Li, F.; Wang, D. W.; Tang, D. M.; Liu, C.; Ma, X. L.; Lu, G. Q.; Cheng, H. M.: Electron field emission of a nitrogen-doped TiO_2 nanotube array. *Nanotechnology* **2008**, *19*.

(42) Serpone, N.: Is the band gap of pristine TiO_2 narrowed by anion- and cation-doping of titanium dioxide in second-generation photocatalysts? *J Phys Chem B* **2006**, *110*, 24287-24293.

(43) Lira, E.; Wendt, S.; Huo, P. P.; Hansen, J. O.; Streber, R.; Porsgaard, S.; Wei, Y. Y.; Bechstein, R.; Laegsgaard, E.; Besenbacher, F.: The Importance of Bulk Ti^{3+} Defects in the Oxygen Chemistry on Titania Surfaces. *J Am Chem Soc* **2011**, *133*, 6529-6532.

(44) Asahi, R.; Morikawa, T.; Irie, H.; Ohwaki, T.: Nitrogen-Doped Titanium Dioxide as Visible-Light-Sensitive Photocatalyst: Designs, Developments, and Prospects. *Chem Rev* **2014**, *114*, 9824-9852.

(45) Takata, T.; Domen, K.: Defect Engineering of Photocatalysts by Doping of Aliovalent Metal Cations for Efficient Water Splitting. *J Phys Chem C* **2009**, *113*, 19386-19388.

Chapter 2

Impacts of oxygen vacancies on the electrocatalytic activity of $AuTiO_2$ nanocomposites towards oxygen reduction

Abstract

Nanocomposites based on metal nanoparticles supported on oxide surfaces have been used extensively as effective catalysts for fuel cell electrochemistry. In this study, functional nanocomposites based on gold nanoparticles deposited onto TiO_2 colloids were prepared by a simple wet chemistry method, and subject to hydrothermal treatment at a controlled temperature in the presence of ascorbic acid. Transmission electron microscopic measurements showed that the gold nanoparticles (10-30 nm in diameter) were embedded within the TiO_2 matrix consisting of colloids of 5-10 nm in diameter and anatase crystalline structures, as evidenced in x-ray diffraction studies. Interestingly, electron paramagnetic resonance measurements showed the formation of oxygen vacancies after hydrothermal treatment and the concentrations of oxygen vacancies increased with the amount of ascorbic acid added. Consistent results were obtained in x-ray photoelectron spectroscopic measurements, which suggested partial charge transfer from gold to oxygen-deficient TiO_2. The Au:Ti atomic ratio in the nanocomposites was estimated to be ca. 11% and consistent among the series of samples. Electrochemically, the nanocomposites exhibited apparent electrocatalytic activity towards oxygen reduction reactions in alkaline media, which showed a peak-

shaped variation with the concentration of the oxygen vacancies. This was accounted for by the deliberate manipulation of the binding energy of oxygen species onto the nanocomposite surfaces. In addition, the $AuTiO_2$ nanocomposites exhibited markedly enhanced tolerance against methanol crossover, as compared to commercial Pt/C catalysts.

2.1 Introduction

Nanocomposites based on metal nanoparticles supported on oxide surfaces have been used extensively as effective catalysts for a wide range of chemical reactions, including fuel cell electrochemistry. In fact, such functional hybrid materials have been found to exhibit apparent electrocatalytic activity towards both oxidation of fuel molecules at the anode and reduction of oxygen at the cathode, with catalytic performances comparable, or even superior, to that of state-of-the art platinum catalysts.[1-4] This has been ascribed largely to the strong metal-support interactions.[5-9] For instance, Comotti and co-workers deposited gold nanoparticles on various metal oxides and found that the electrocatalytic activity towards CO oxidation varied with the oxide support, with $AuTiO_2$ identified as the best catalyst among the series.[10] In another study[11] Lin et al. prepared a series of $AuTiO_2$ nanocomposites and identified an optimal gold loading for maximal activity towards oxygen reduction reactions (ORR), which was accounted for by the dependence of surface OH concentration on gold contents. Similarly, Chen and co-workers deposited gold on SnO_2 nanoparticles, and observed that the gold loading played a vital role in the determination of the

electrocatalytic activity towards ORR.[12] With an increasing gold loading, the ORR evolved from a two-electron pathway to a four-electron one, and Tafel analysis showed that the optimal gold loading was ca. 1.9 at.%.[12]

In these earlier studies, it is generally difficult to control the deposition and dispersion of metal nanoparticles on the oxide surfaces.[13-15] Horvath et al.[16] employed two different methods to mitigate such an issue. In the first method, TiO_2 was deposited onto gold colloid surface by hydrolysis of a titanium-alkoxide precursor and the resulting core@shell nanostructures were then adsorbed onto a SiO_2 surface by electrostatic interactions. In the second method, gold colloids were grown onto the SiO_2 surface, and then a layer of TiO_2 was coated onto the composite by controlled hydrolysis. The resulting $AuTiO_2/SiO_2$ nanocomposites were much more stable than the $AuTiO_2$ counterparts, and their CO oxidation activity was markedly higher than the $AuSiO_2$ reference sample. This was attributed to the controlled growth of the $AuTiO_2$ interface.[16] In another study,[17] Ma and co-workers deposited SiO_2 onto $AuTiO_2$ nanocomposites, which also exhibited enhanced catalytic activity and stability for CO oxidation, as compared to $AuTiO_2$ alone. Similarly, Huang and co-workers successfully coated gold nanoparticles with ZrO_2 or TiO_2 through an assembly approach, and these "nanoreactors" were found to exhibit superior catalytic activity for CO oxidation, due to their porous structure and enhanced stability, as compared to the uncoated ones.[18]

However, metal oxides typically exhibit only low electrical conductivity, which is detrimental to the electron-transfer reactions on the catalyst surface. To increase

metal oxide conductivity, a number of methods have been reported in the literature. These include manipulation of the oxide crystallinity,[19,20] doping,[21-23] combination with carbon substrates,[24,25] and introduction of oxygen vacancies into the oxide structure.[26] Of these, Linh and co-workers carried out DFT calculations to examine the impacts of oxygen vacancies in TiO_2 on oxygen adsorption, and found that the formation of oxygen vacancies enhanced the adsorption of oxygen species because of an increase of the oxygen binding energy.[27] Aschauer and co-workers also showed that oxygen adsorption might be enhanced by defect electrons transferring in the TiO_2 surface band gap.[28] Thus, one immediate question arises. Will the ORR electrocatalytic activity be enhanced by the formation of oxygen vacancy in the oxide support?

Note that thus far experimental studies have been scarce that focus on the impacts of TiO_2 oxygen vacancies on the ORR activity of metal-TiO_2 nanocomposites. This is the primary motivation of the present study. Herein, we prepared a series of $AuTiO_2$ nanocomposites by colloidal chemistry, and the concentration of oxygen vacancy in TiO_2 was deliberately manipulated by hydrothermal heating[29] and ascorbic acid reduction,[30] and evaluated by electron paramagnetic resonance measurements. Electrochemical measurements showed that the nanocomposites exhibited apparent ORR activity in alkaline media, which displayed a volcano-shaped variation with the TiO_2 oxygen vacancies. The optimal nanocomposites were found to exhibit an ORR activity that was comparable to that of commercial platinum catalysts, along with enhanced tolerance against methanol crossover.

2.2 Experimental

2.2.1 Chemicals.

Titanium(IV)-tert-butoxide (97%, Sigma-Aldrich), hydrogen tetrachloroauric acid ($HAuCl_4$, Sigma-Aldrich), oleic acid (≥99%, Sigma-Aldrich), 3-chloroaniline (≥99.0%, Sigma-Aldrich), sodium borohydride (≥98%, Sigma-Aldrich), and ascorbic acid (99.0%, Sigma-Aldrich) were used as received. Solvents were purchased from typical commercial sources at their highest purity and used without further treatment. Water was supplied from a Barnstead Nanopure Water System (18.3 MΩ cm).

2.2.2 Preparation of TiO_2 nanoparticles.

TiO_2 nanoparticles were prepared by adopting a method reported previously.[31] In brief, titanium(IV)-tert-butoxide (0.182 g) was dissolved in 5 mL of water, and 0.791 g of 3-chloroaniline and 0.582 g of oleic acid were dissolved in 5 mL of toluene. Then the two solutions were added to a Teflon-lined autoclave and heated at 180°C for 12 h. A white precipitate was produced at the bottom of the autoclave which was collected by centrifugation, washed with methanol several times, and dried under vacuum, affording purified TiO_2 nanoparticles.

2.2.3 Preparation of $AuTiO_2$ nanocomposites.

$AuTiO_2$ nanocomposites were prepared by adopting a protocol described previously.[32] Experimentally, the TiO_2 nanoparticles prepared above (0.0755 g) were dispersed in 100 mL of tetrahydrofuran. Then a calculated amount of $HAuCl_4$ was

added, followed by dropwise addition of a cold aqueous solution of sodium borohydride (10 molar excess as compared to gold), leading to an immediate color change from yellow to purple, signifying the formation of gold nanoparticles. The solution was subject to magnetic stirring at room temperature for about 1 h, followed by removal of tetrahydrofuran by rotary evaporation. The purple precipitates were dried under vacuum and denoted as $AuTiO_2$-pre.

The obtained $AuTiO_2$-pre then underwent hydrothermal treatment in the presence of ascorbic acid to produce oxygen vacancies. In a typical experiment, about 50 mg of $AuTiO_2$-pre was added into a Teflon-lined autoclave, along with a calculated amount of ascorbic acid and 10 mL of water. The mixture was heated at 180°C for 12 h. Four samples were prepared at the ascorbic acid:gold molar ratios of 0.5:1, 1:1, 2:1, and 3:1. The corresponding nanocomposites were denoted as $AuTiO_2$-I, $AuTiO_2$-II, $AuTiO_2$-III, and $AuTiO_2$-IV, respectively.

2.2.4 Characterizations.

The sample morphologies were examined with a transmission electron microscope (TEM, Philips CM300) operated at 300 kV. X-ray photoelectron spectroscopic (XPS) measurements were carried out with a PHI 5400/XPS instrument equipped with an Al K_α source operated at 350 W and 10^{-9} Torr. Diffuse reflectance UV-vis spectra were acquired with a Perkin-Elmer Lambda 35 spectrometer. X-ray diffraction (XRD) measurements were performed with a Rigaku Miniflex powder

diffractometer using Cu K_α radiation with a Ni filter (λ = 0.154059 nm at 30 kV and 15 mA) that features a

detection limit of 0.04°.

2.2.5 Electron paramagnetic resonance (EPR).

For EPR measurements, samples were prepared by filling quartz EPR tubes (Wilmad, 4 mm outer diameter) with one centimeter of powdered materials and centering the sample in the cavity resonator for data collection. Spectra were recorded at room temperature with a Bruker EMX EPR spectrometer operating at the X-band frequency (~9.4 GHz) using an ER 4122SHQE resonator (Bruker). All spectra were recorded at a power of 1 mW, a modulation amplitude of 1 G, and a modulation frequency of 100 KHz. Signal intensity was calculated as the peak-to-peak amplitude (S') of the EPR signal and double integration of the recorded signal. Progressive power saturation experiments were performed by recording spectra at various microwave powers between 0.063 and 63 mW. The data were analyzed by plotting S' vs. the square root of the microwave power.

2.2.6 Electrochemistry.

Electrochemical experiments were carried out with a CHI 710 Electrochemical Workstation with a glassy-carbon disk and gold ring electrode, a platinum counter electrode, and a Ag/AgCl reference electrode. A catalyst ink was prepared by adding 10 mg of the $AuTiO_2$ nanocomposites prepared above and 40 mg of carbon black

dispersed in 500 mL of ethanol and 5 mL of Nafion (corresponding to a nanocomposite concentration of 20 wt.%). The ink was then dropcast onto the glassy carbon disk at a nanocomposite loading of ca. 20 mg, and dried in air before being immersed into electrolyte solutions for data acquisition. The Ag/AgCl electrode was calibrated against a reversible hydrogen electrode (RHE), and the potentials were all referred to this RHE electrode.

2.3 Results and Discussion

2.3.1 Structural and Optical Characterization.

Figure 2.1 depicts two representative TEM micrographs of the $AuTiO_2$-III nanocomposites. From panel (A), it can be seen that gold nanoparticles, which appeared as dark-contrast objects, were embedded within a low-contrast matrix of TiO_2 nanoparticles. The gold nanoparticles were somewhat polydisperse in size, ranging from 10 to 30 nm with an average diameter of 23.1 ± 5.2 nm, whereas the TiO_2 nanoparticles were much smaller, forming large-scale aggregates. From the high-resolution image in panel (B), one can see that the TiO_2 nanoparticles were markedly smaller at 5 to 10 nm in diameter, with well-defined lattice fringes where the interplanar spacing of 0.376 nm is consistent with that of anatase TiO_2 (101) planes (JCPDS no. 21-1272); and the gold nanoparticles were indeed in intimate contact with the TiO_2 nanoparticles, where the interplanar distance of 0.23 nm is in good agreement with the (111) crystalline planes of fcc Au (JCPDS no. 4-784). Consistent surface morphologies were observed with other $AuTiO_2$ nanocomposites in the series.

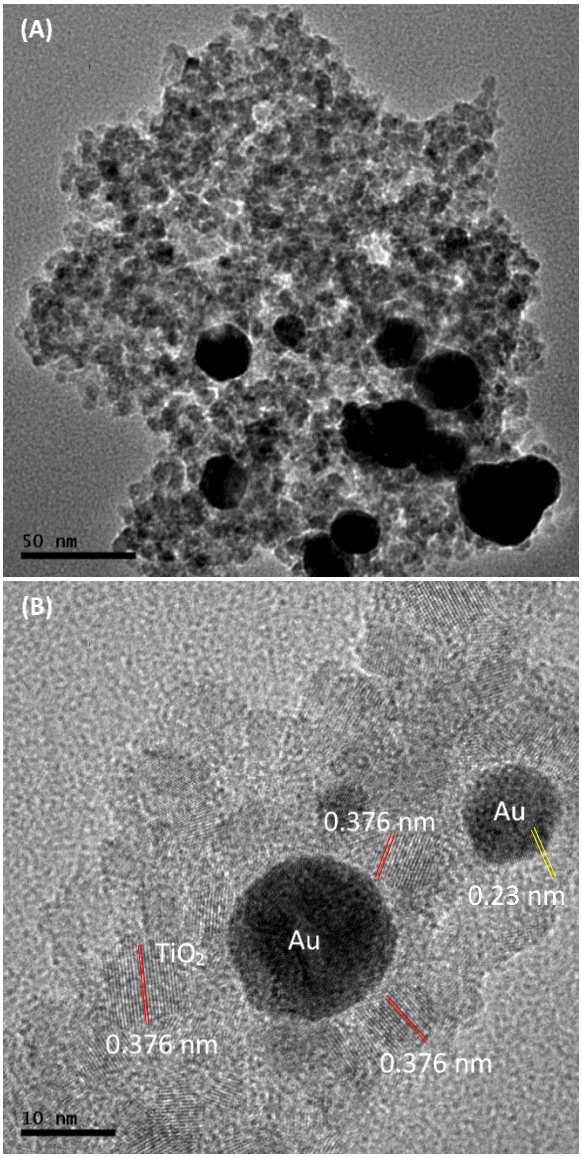

Figure 2.1 Representative TEM micrograph of $AuTiO_2$-III nanocomposites. Scale bars are (A) 50 nm and (B) 10 nm.

The structures of the $AuTiO_2$ nanocomposites were then characterized by XRD measurements. From Figure 2.2, one can see that prior to gold nanoparticle deposition, the TiO_2 nanoparticles exhibited a series of well-defined diffraction peaks at $2\theta = 25.3°$,

38.1°, 48.0°, 54.5°, and 63.0°, corresponding to the (101), (104), (200), (211), and (213) crystalline planes of anatase TiO_2 (JCPDS no. 21-1272), respectively.[33] After gold nanoparticle deposition, the gold diffraction features (JCPDS no. 4-784) can be clearly identified for all $AuTiO_2$ nanocomposites at $2\theta = 38.3°$ for Au(111), 44.2° for Au(200), 64.5° for Au(220) and 77.6° for Au(311);[34] and the TiO_2 (101) diffraction can also be resolved at $2\theta = 25.3°$, although it became increasingly broadened after hydrothermal treatment with the addition of an increasing amount of ascorbic acid, likely due to the formation of structural defects (oxygen vacancies), as manifested in XPS and EPR measurements (*vide infra*).

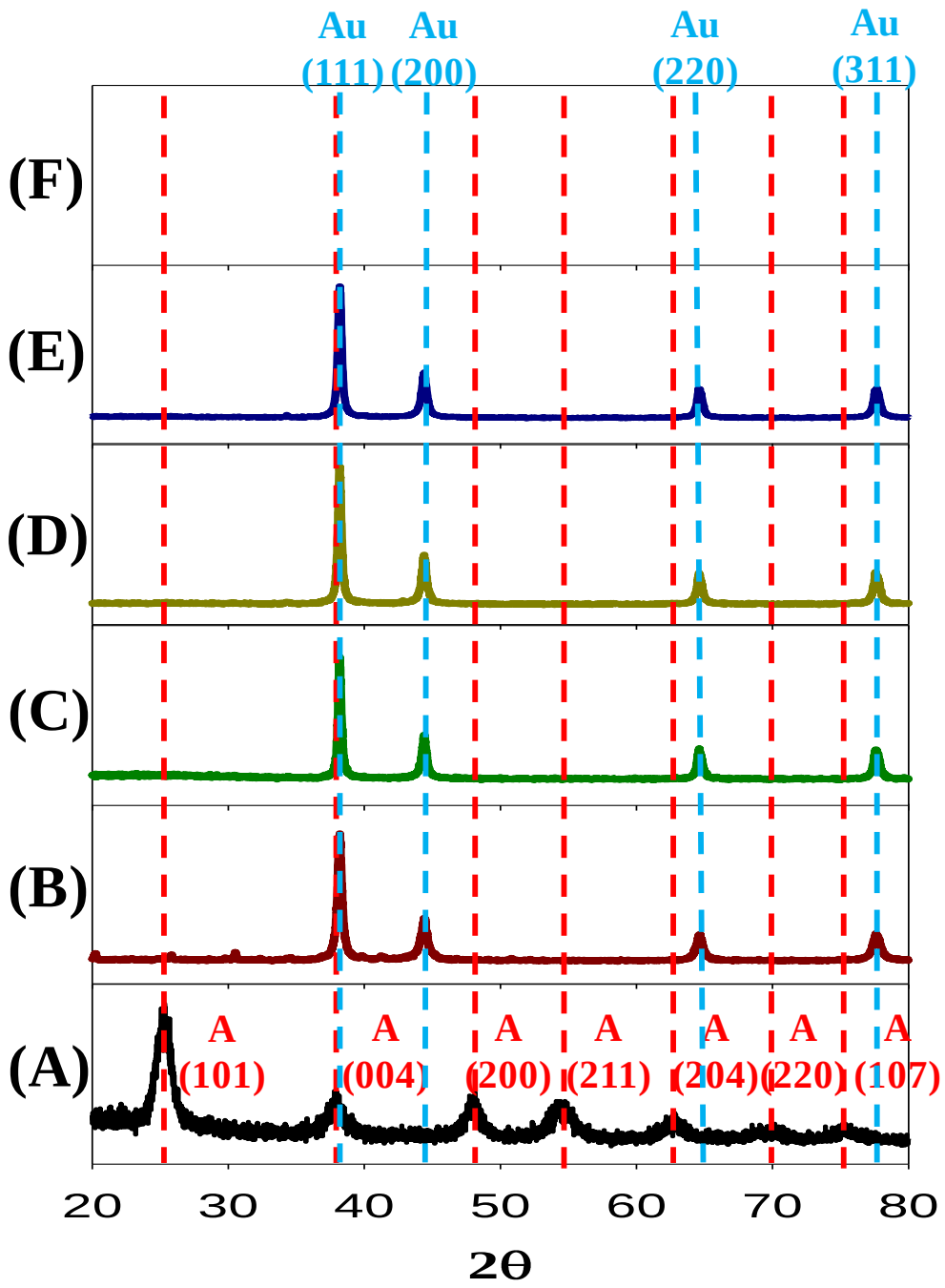

Figure 2.2 XRD spectra of TiO_2 and $AuTiO_2$ nanocomposites before and after hydrothermal treatment with ascorbic acid.

The formation of $AuTiO_2$ nanocomposites was further manifested in diffuse reflectance UV-vis measurements. From Figure 2.3, one can see that TiO_2 colloids alone exhibit only a largely featureless absorption profile, and the extension of absorption down to 700 nm suggests the possible formation of defects states that arose from structural defects,[35] considering the bandgap of anatase TiO_2 is about 3.2 eV.[36] After the deposition of gold nanoparticles onto TiO_2, the absorption was markedly enhanced in the visible range. In particular, the $AuTiO_2$ nanocomposites all exhibited a broad absorption peak centered at ca. 543 nm (marked by the dashed line). This can be ascribed to the surface plasmon resonance of gold nanoparticles[37] that were rather polydisperse in size and aggregated to some extent (Figure 2.1). The results also suggest a similar structure of the gold nanoparticles within the series of nanocomposites before and after hydrothermal treatment with the addition of various amounts of ascorbic acid.

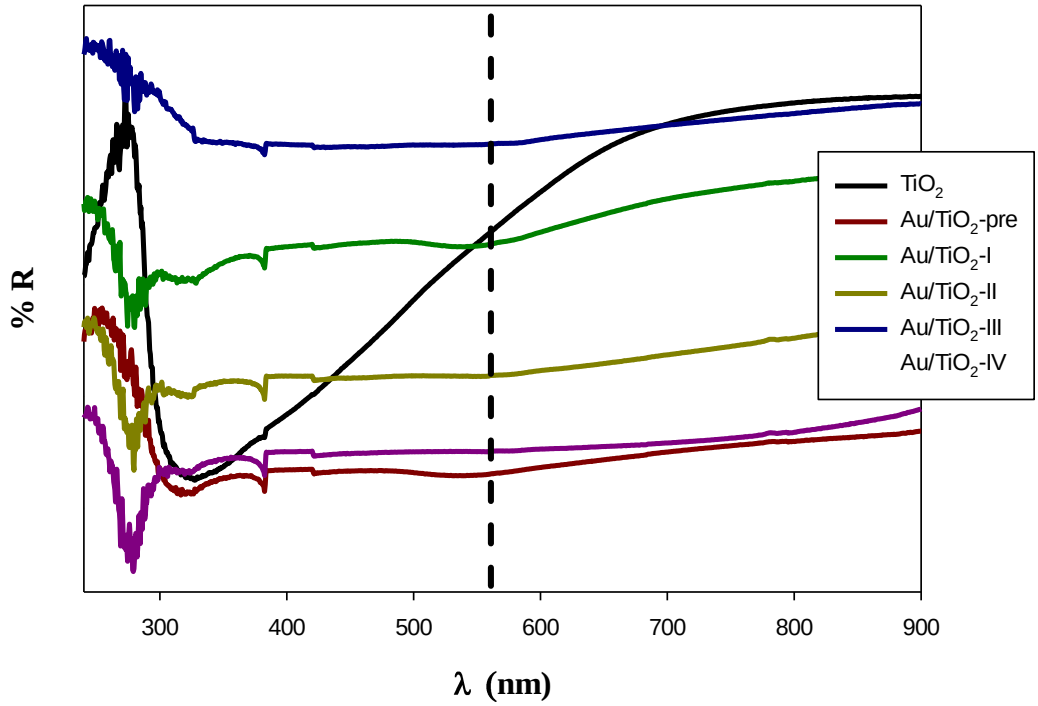

Figure 2.3 Diffuse reflectance UV-vis spectra of TiO_2 colloids and $AuTiO_2$ nanocomposites before and after hydrothermal treatment with ascorbic acid.

2.3.2 Characterization of Oxygen Vacancies.

However, the nanocomposites exhibited a clear variation of the concentration of oxygen vacancies with the amount of ascorbic acid added in hydrothermal treatment, as revealed in EPR measurements. Figure 2.4 depicts the EPR spectra of the series of $AuTiO_2$ nanocomposites. One can see that the prehydrothermal $AuTiO_2$-pre sample exhibited largely a featureless profile. In sharp contrast, after hydrothermal treatment with ascorbic acid, all nanocomposites showed a resonance transition centered at ca. 3370 G, with a corresponding g value of 2.003, which became increasingly intensified

with an increasing amount of ascorbic acid added. This may be ascribed to the formation of unpaired electrons being trapped at the TiO_2 surface, consistent with results reported in earlier studies,[26,30,35,38] due to partial reduction of Ti(IV) to Ti(III) by ascorbic acid.[30,39,40] Indeed, power saturation measurements of $AuTiO_2$-III (Figure 2.4) show that the peak-to-peak derivative signal (S') initially increased with the microwave power, reached a maximum at a power around 1 mW, and then decreased with a further increase of the microwave power, indicating that the signal reached saturation. The data was fitted to Eq. (2.1),

$$S' = K \frac{\sqrt{P}}{(1 + \frac{P}{P_{\frac{1}{2}}})^{b/2}} \quad (2.1)$$

where K is a constant, P is the incident microwave power, $P_{½}$ is the power at half saturation that is directly proportional to the spin-lattice (T_1) and spin-spin (T_2) relaxation rates,[41] and b is a factor between 1 (for an inhomogeneous line) and 3 (for a purely homogenous line).[42] A spin system that is easily saturated will have a low $P_{½}$ and a long relaxation rate. From

the fitting, $P_{½}$ was estimated to be only 0.52 mW; such a low $P_{½}$ value is characteristic of trapped oxygen radicals.[43-45]

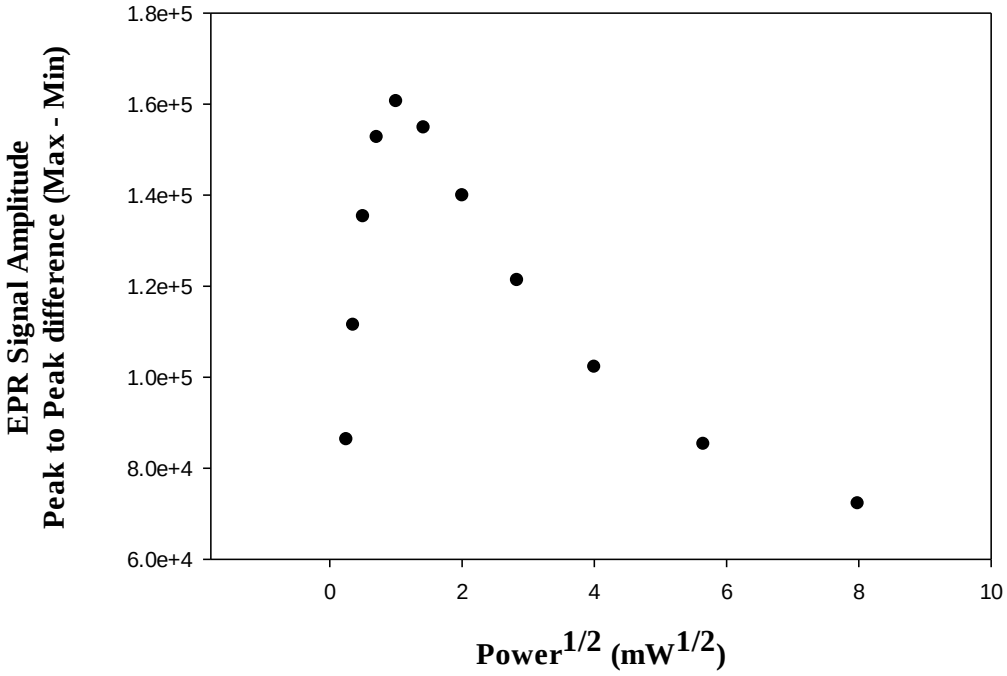

Figure 2.4 EPR power saturation curve for the $AuTiO_2$-III sample. Symbols are experimental data and line is fit by the equation $S' = K \frac{\sqrt{P}}{\left[1 + P/P_{1/2}\right]^{b/2}}$, with the fitting parameters of K = 3.669×10^5, $P_{½}$ = 0.5196 mW, and b = 1.5328.

Furthermore, one can see that the apparent oxygen vacancy concentration increased with the amounts of ascorbic acid added. This can be better manifested in the top inset to Figure 2.5 which compared the amplitude difference in the EPR signals among the series of $AuTiO_2$ samples, as well as in the bottom inset which depicts the double integration of the respective spectrum. Both of these may be exploited for a rough estimation of how many species are causing the resonance signals.[46] From the

results, one can see that the defect concentration (oxygen vacancies) increased in the order of $AuTiO_2$-pre ≤ $AuTiO_2$-II < $AuTiO_2$-I < $AuTiO_2$-III < $AuTiO_2$-IV.

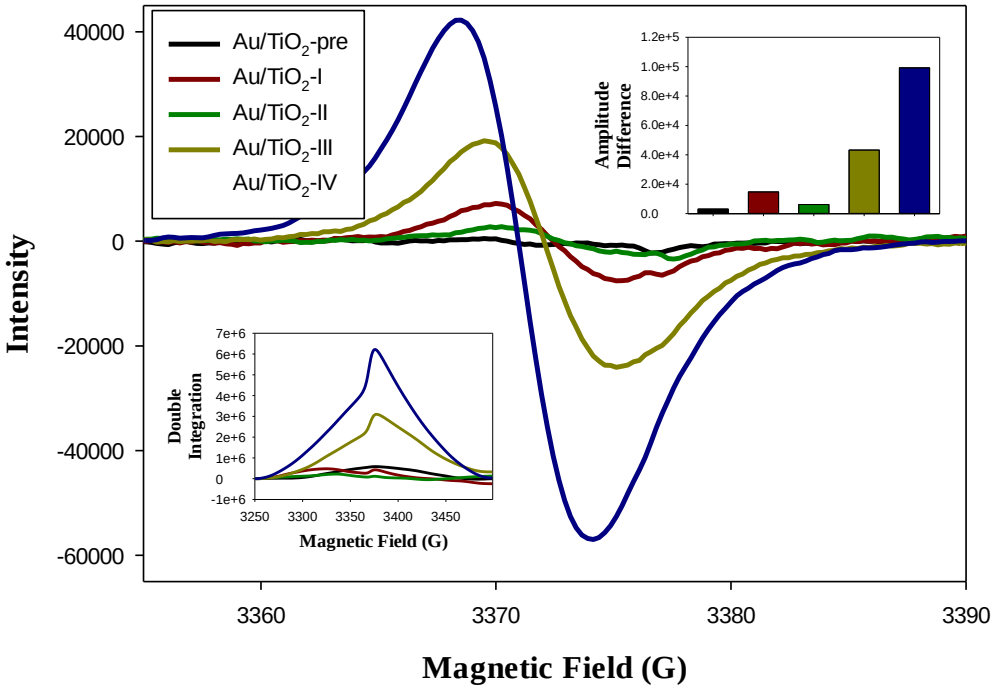

Figure 2.5 EPR spectra of the series of $AuTiO_2$ nanocomposites. Bottom inset is the double integration of the corresponding spectra, and top inset shows the variation of the amplitude difference with the ascorbic acid:gold feed ratio.

Further structural insights into the elemental compositions and valence states of the series of the $AuTiO_2$ nanocomposites were unravelled by XPS measurements. From the survey spectra (Figure 2.6), the Ti 2p, O 1s, and Au 4f electrons can be clearly

identified with the $AuTiO_2$ nanocomposites at around 458, 530, and 85 eV (along with C 1s electrons at 285 eV), respectively.

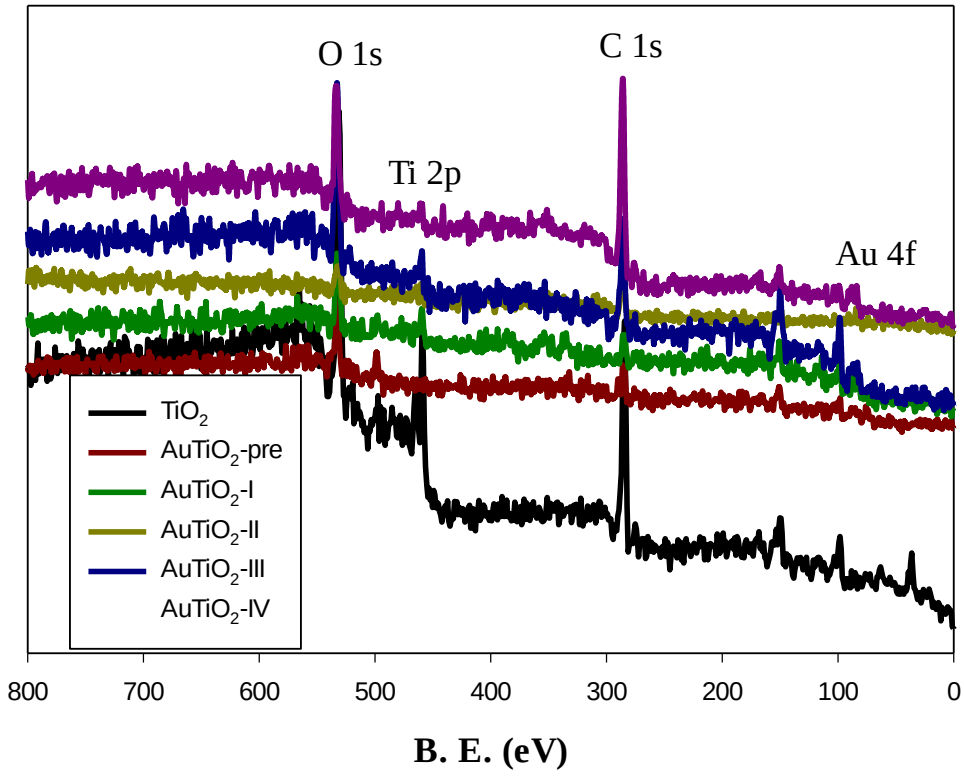

Figure 2.6 XPS survey spectra of TiO_2 and $AuTiO_2$ nanocomposites.

In high-resolution scans (Figure 2.7), one can see that for all $AuTiO_2$ nanocomposites (panels (B) to (E)) the Ti 2p electrons appeared as a doublet at the binding energies of around 458.7 and 464.5 eV with a peak separation of 5.8 eV, consistent with those in TiO_2 colloids (panel (A));[47] and for the $AuTiO_2$-III and $AuTiO_2$-IV samples, there were some apparent deviations from deconvolution fits at

around 460 eV (marked by the dashed circles), which might be ascribed to the Ti 2p½ electrons of Ti(III).[48] This is in good agreement with the EPR results where the concentrations of oxygen vacancies were markedly higher in these two samples than in the rest of the series (Figure 2.5). For O 1s electrons, all samples (including TiO_2 colloids) exhibited two peaks at the binding energies of 530.4 and 532.6 eV. The former may be assigned to oxygen in TiO_2 whereas the latter is most likely due to hydroxyl groups adsorbed on the TiO2 and/or Au surfaces.[49] For the Au 4f7/2 electrons, the binding energy was rather consistent for all $AuTiO_2$ nanocomposites at ca. 82.5 eV (with Au 4f5/2 at 86.3 eV), which was markedly lower than that (84.0 eV) typically observed with bulk gold and gold nanoparticles.[50] This signifies electron-rich gold, likely due to excess $NaBH_4$ used in nanoparticle synthesis as well as hydrothermal treatment in the presence of reductive ascorbic acid. Such a low binding energy for Au 4f electrons has been reported previously, for instance, with Au nanoparticles supported on TiO_2-MO_x (M = Fe, Co, Zn) and ascribed to effective charge transfer from the oxides to gold,[51] as well as with TiO_2-supported AuPd alloy nanoparticles that were subjected to a thermal treatment in a H_2 atmosphere.[52] For $AuTiO_2$-III and $AuTiO_2$-IV, the appreciable concentrations of oxygen vacancies (Figure 2.5) further enhanced the electron density on Au that likely facilitated the adsorption of hydroxyl groups, as evidenced by a second pair of Au 4f peaks at somewhat higher energies of 83.3 and 88.5 eV.[53] Furthermore, based on the integrated peak areas, the Au:Ti atomic ratio was found to be rather consistent at 11% for all the $AuTiO_2$ nanocomposites.

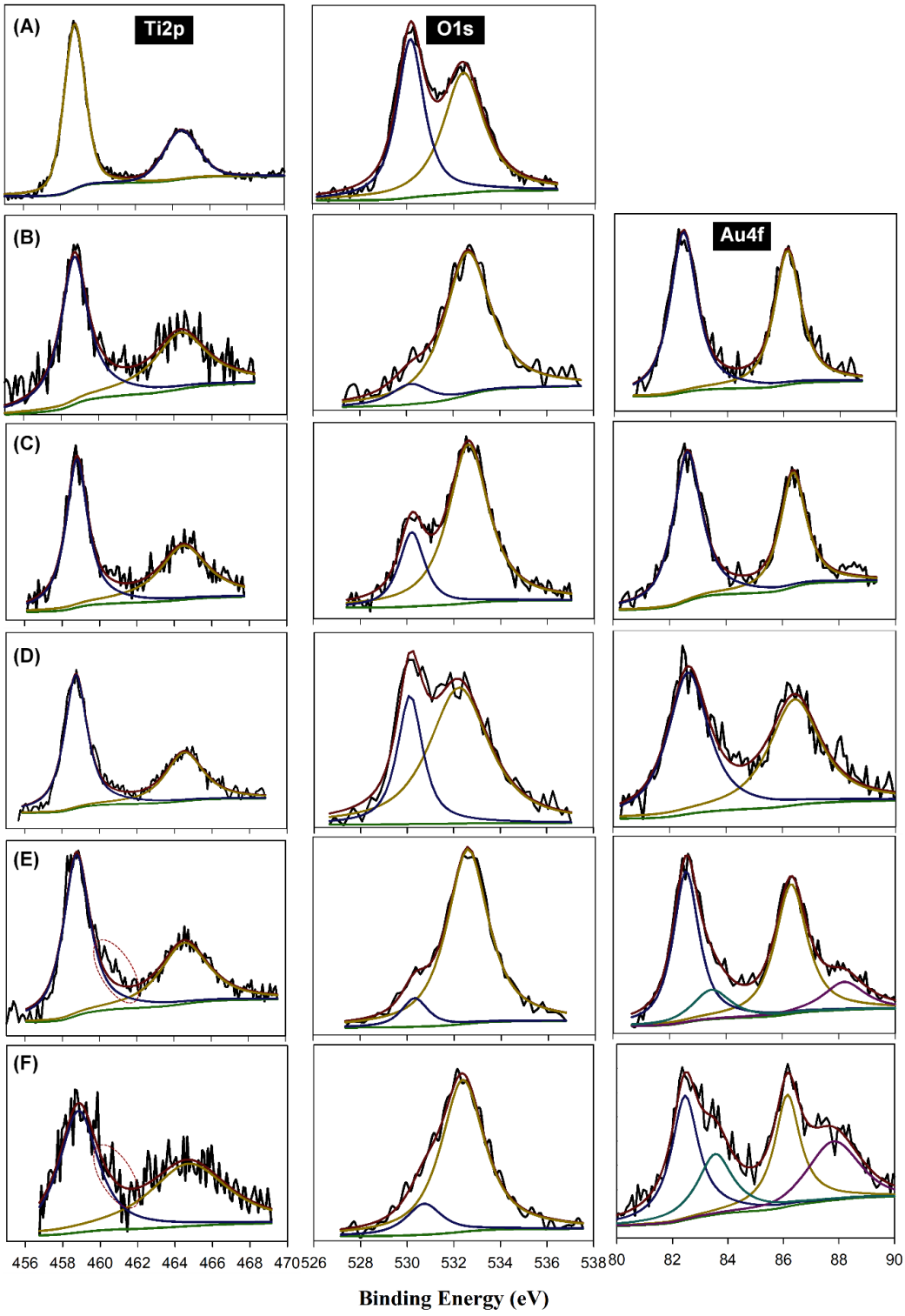
(A)
Ti2p
O1s
(B)
Au4f
(C)
(D)
(E)
(F)
456 458 460 462 464 466 468 470
526 528 530 532 534 536 538
80 82 84 86 88 90
Binding Energy (eV)

Figure 2.7 XPS spectra of Ti2p O1s and Au4f electrons of (A) TiO_2, (B) $AuTiO_2$-pre, (C) $AuTiO_2$-I, (D) $AuTiO_2$-II, (E) $AuTiO_2$-III, and (F) $AuTiO_2$-IV. Black curves are experimental data and colored curves are deconvolution fits. (For interpretation of the references to colour in this figure legend, the reader is referred to the web version of this article.)

2.3.3 Electrocatalytic activity for the ORR.

The electrocatalytic activity of the nanocomposites prepared above were then examined by electrochemical measurements in alkaline media. Figure 2.8 depicts the steady-state cyclic voltammograms of the nanocomposites loaded onto a glassy carbon electrode in a N_2-saturated 0.1 M NaOH solution at the potential scan rate of 100 mV s^{-1}. It can be seen that in contrast to TiO_2 colloids that exhibited only a featureless voltammetric profile due to double-layer capacitance charging,[19,32] the series of $AuTiO_2$ nanocomposites all showed a pair of voltammetric peaks, where the anodic peak at around +1.3 V can be ascribed to electrochemical oxidation of gold and the cathodic peak at ca. +1.0 V to the reduction of gold oxides. Furthermore, based on the integrated peak areas of gold oxide reduction, the effective electrochemical surface area was estimated to be rather consistent at 0.22 cm^2 for $AuTiO_2$-pre, 0.13 cm^2 for $AuTiO_2$-I, 0.12 cm^2 for $AuTiO_2$-II, 0.71 cm^2 for $AuTiO_2$-III, and 0.30 cm^2 for $AuTiO_2$-IV.[54]

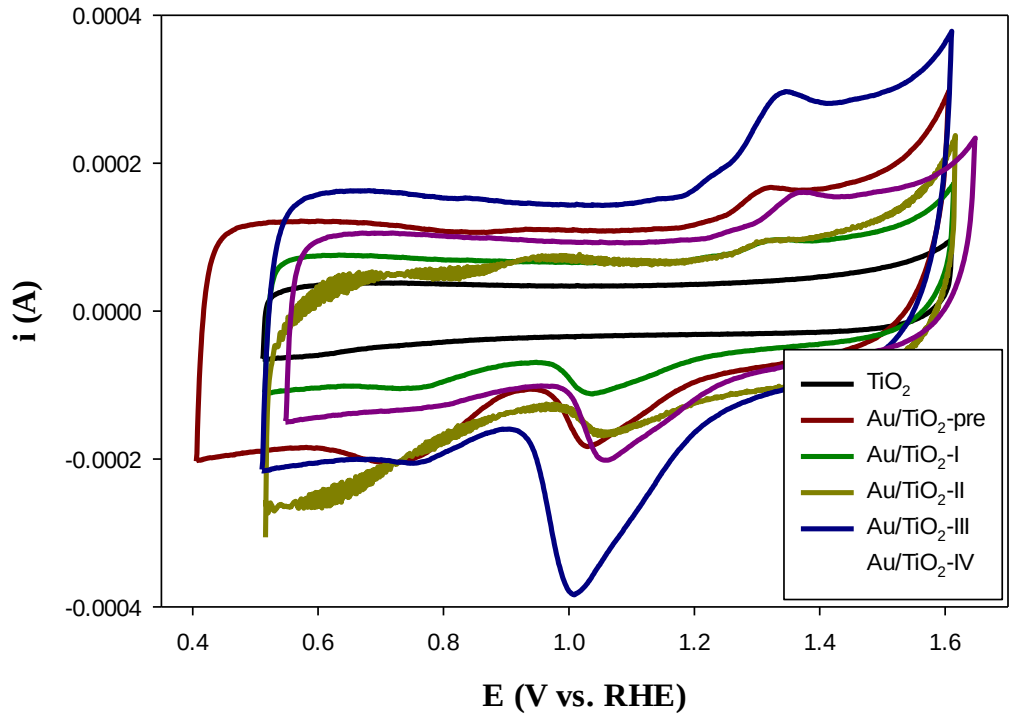

Figure 2.8 Cyclic voltammograms of a glassy carbon electrode modified with TiO_2 and $AuTiO_2$ nanocomposites in a nitrogen-saturated 0.1 M NaOH solution. Potential scan rate 100 mV/s. Catalyst loadings were all 20 g. Based on the integrated peak areas of gold oxide reduction, the effective electrochemical surface area was estimated to be 0.22 cm^2 for $AuTiO_2$-pre, 0.13 cm^2 for $AuTiO_2$-I, 0.12 cm^2 for $AuTiO_2$-II, 0.71 cm^2 for $AuTiO_2$-III, and 0.30 cm^2 for $AuTiO_2$-IV.

The $AuTiO_2$ nanocomposites were then evaluated for their electrocatalytic activity towards ORR. Figure 2.9(A) shows the RRDE measurements in an O_2 saturated 0.1 M NaOH solution at the rotation rate of 1600 rpm. One can see that for all samples, nonzero cathodic currents at the disk electrode emerged at sufficiently negative

electrode potentials, suggesting apparent electrocatalytic activity towards ORR, despite the relatively large size of the Au nanoparticles (Figure 2.1). However, the performance was markedly different among the series of samples. For instance, the onset potential for TiO_2 nanoparticles was estimated to be +0.73 V; yet for the $AuTiO_2$ nanocomposites, the onset potentials were far more positive by ca. 200 mV, at +0.92 V for $AuTiO_2$-pre, $AuTiO_2$-I and AuTiO2-II, and +0.95 V for $AuTiO_2$-III and $AuTiO_2$-IV, indicating marked enhancement of the catalytic performance by the incorporation of gold nanoparticles onto TiO_2. Significant discrepancy can also be seen in the diffusion limiting currents. For instance, at +0.60 V and 1600 rpm, the current density (J_m, voltammetric currents normalized to the composite loading) can be found at 2.67 A g^{-1} for TiO_2, but increased by more than two folds to 7.04 A g^{-1} for $AuTiO_2$-pre, 7.13 A g^{-1} for $AuTiO_2$-I, 7.46 A g^{-1} for $AuTiO_2$-II, 9.89 A g^{-1} for $AuTiO_2$-III, and 6.55 A g^{-1} for $AuTiO_2$-IV. Taken together, these results suggest that the $AuTiO_2$-III nanocomposites stood out as the best catalysts among the series.

Furthermore, by setting the ring electrode at +1.5 V, collection experiments showed that the ring currents were at least one order of magnitude lower than those at the disk,

indicating only a minimal amount of peroxide species were produced during oxygen reduction. In fact, the number of electron transfer (n) may be quantified by Eq. (2.2),

$$n = \frac{4I_D}{I_D + {I_R}/{N}} \tag{2.2}$$

where ID and IR are the voltammetric currents at the disk and ring electrodes, respectively, and N is the collection efficiency (0.40).[55] From panel (B), one can see that within the potential range of +0.4 to +1.0 V, the n values increase in the order of TiO_2 < $AuTiO_2$-pre < $AuTiO_2$-II < $AuTiO_2$-I < $AuTiO_2$-III < $AuTiO_2$-IV. For instance, at +0.60 V, n = 3.13 for TiO_2, 3.58 for $AuTiO_2$-pre, 3.68 for $AuTiO_2$-I, 3.54 for $AuTiO_2$-II, 3.71 for $AuTiO_2$-III, and 3.81 for $AuTiO_2$-IV, corresponding to a H_2O_2 yield of 34.8%, 16.8%, 12.8%, 18.4%, 11.6%, and 7.6% respectively. That is, with the formation of $AuTiO_2$ nanocomposites, the H_2O_2 yield decreased significantly and the ORR proceeded mostly by the four-electron reduction pathway, $O_2 + 2H_2O + 4e \rightarrow 4OH^-$.[11,56]

Further insights into the ORR electron transfer kinetics can be obtained from analysis and comparison of the Tafel plots, where the kinetic current density (J_k) was quantified by the y-axis intercepts of the respective Koutecky-Levich plots.[57] From panel (C), it can be seen that for all nanocomposite catalysts, the kinetic current densities increased with increasingly negative electrode potential, and within the potential range of +0.95 to +0.55 V, $AuTiO_2$-III exhibited the highest kinetic current density, whereas TiO_2 the lowest, with the rest of the samples showing similar activity in the intermediate range. For instance, at +0.90 V, the kinetic current density was only 0.40 A g^{-1} for $AuTiO_2$-I, 0.43 A g^{-1} for $AuTiO_2$-II, 0.70 A g^{-1} for $AuTiO_2$-pre, 0.71 A g^{-1} for $AuTiO_2$-IV, and 1.96 A g^{-1} for $AuTiO_2$-III (only minimal activity for TiO_2 at this potential).

In addition, one may note that the Tafel slope of the series of sample was actually very close at 110 mV dec^{-1} for TiO_2, 158 mV dec^{-1} for $AuTiO_2$-pre, 136 mV dec^{-1} for $AuTiO_2$-I, 136 mV dec^{-1} for $AuTiO_2$-II, 114 mV dec^{-1} for $AuTiO_2$-III, and 134 mV dec^{-1} for $AuTiO_2$-IV. This implies a similar ORR mechanism for this series of $AuTiO_2$ catalysts where the rate-determining step was likely the first electron reduction of oxygen.[11,12]

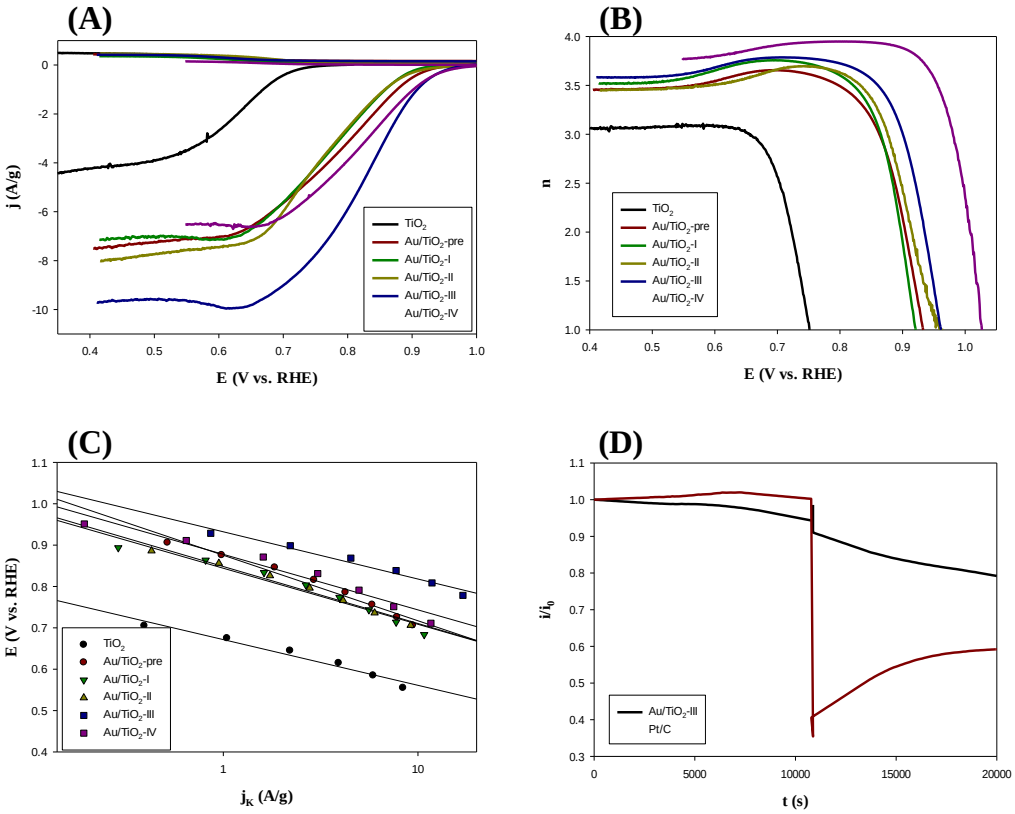

Figure 2.9 (A) RRDE voltammograms of a glassy carbon electrode modified with TiO_2 and $AuTiO_2$ nanocomposites in an oxygen-saturated 0.1 M NaOH solution. Potential scan rate 10 mV s^{-1} and rotation rate 1600 rpm. Catalyst loadings 20 mg of composite.

(B) Variation of the number of electron transfer (n) with electrode potential. Data were obtained from the voltammograms in panel (A). (C) Tafel plots of the various nanocomposite catalysts. (D) Chronoamperometric profiles of $AuTiO_2$-III and Pt/C catalysts in an oxygen-saturated 0.1 M NaOH solution at the electrode potential of +0.60 V, where 1 M methanol was injected into the electrolyte solution at t = 3 h.

For metal/metal oxide nanocomposites,[11,12] it has been known that the electronic interactions at the interface likely play a key role in determining the bonding interactions with oxygen species and hence the ORR activity. In the present study, the discrepancy of the ORR performances observed above may be accounted for by the impacts of oxygen vacancies on the adsorption of oxygen intermediates on the composite surfaces. The $AuTiO_2$-III and $AuTiO_2$-IV samples, which exhibited markedly higher ORR activity than other samples in the series, also showed significantly higher concentrations of oxygen vacancies (Figure 2.5). This most likely led to enhanced adsorption of oxygen species onto the nanocomposites, due to partial charge transfer to Au from oxygen-deficient TiO_2 (Figure 2.7).[58] Importantly, the results presented above suggest an optimal concentration of oxygen vacancies for maximal ORR activity, as manifested by the $AuTiO_2$-III sample which stood out as the best catalyst among the series. This may be accounted for by the fact that whereas oxygen vacancies enhanced bonding interactions between oxygen and the nanocomposites, too strong binding would actually diminish the ORR performance, as manifested by the so-called volcano plot.[59]

It should be noted that the ORR performance of the $AuTiO_2$ nanocomposites observed above was markedly enhanced in comparison with similar composite catalysts that were not treated hydrothermally with ascorbic acid (Table 2.1), within the context of onset potential, n value, and kinetic current density. This suggests that controlled formation of oxygen vacancies may be exploited as a unique, powerful parameter in the deliberate manipulation of the nanocomposite ORR activity.[11,12] Notably, the electrocatalytic activity of $AuTiO_2$-III was rather comparable to that of commercial Pt/C catalysts.[1,2] In addition, the $AuTiO_2$ nanocomposites and Pt/C both exhibited excellent stability, where the ORR currents remained virtually invariant after continuous operation at +0.60 V for ca. 3 h, as depicted in panel (D). One can also see that $AuTiO_2$ showed much better tolerance against methanol poisoning than Pt/C. For instance, upon the injection of 1 M methanol into the electrolyte solution, the ORR current at the Pt/C catalysts dropped by ca. 60% whereas only a 4% decrease was observed with $AuTiO_2$-III.

Table 2.1 Summary of ORR activity of metal-TiO_2 nanocomposites in previous studies

Sample	**E_{onset} (V vs. RHE)**	**n**	**Activity**	**Ref.**
Au/TiO_2	+0.88	3.72	63.7 A/m^2 @ +0.70 V vs. RHE	11
Au/SnO_2	+1.06	4.1	4.1 A/m^2 @ +0.70 V vs. RHE	12
$Au/TiO_2/C$	+0.82	3.0	2.0 A/m^2 @ +0.74 V vs RHE	60
TiO_2	+0.70	-	-	19
$Pt/Cr\text{-}TiO_2$	+0.90	-	4.50 A/m^2 @ +0.9 V vs. RHE	21

Pt/TiO_2@C	+0.95	-	0.1 A/m^2 @ +1 V vs. RHE	24
$CuHC10/TiO_2$	+0.75	3.69	12.38 A/m^2 @ +0.70 V vs. RHE	32
Pt/TiO_2-C	+0.80	-	1.47 A/m^2 @ +0.80 V vs. RHE	61
Pt/TiO_2 mesoporous film	+1.00	-	3.86 A/g @ +0.81 V vs. RHE	62
Au coatings on TiO_2 substrates	+0.95	-	10.1 A/m^2 @ +0.66 V vs. RHE	63
Au/TiO_2	+1.04	-	10 A/m^2 @ +0.74 V vs. RHE	56
Au/CoO_x	+0.90	4	1.4 A @ +0.6 V vs. RHE	64
$Au/Gd_{0.3}Ce_{0.7}O_{1.9}$	+0.80	3.5-3.8	100 A/m^2 @ +0.24 V vs RHE	65

2.4 Conclusions

In this study, gold-TiO_2 nanocomposites were prepared by chemical deposition of gold nanoparticles onto TiO_2 colloid surface. Hydrothermal treatment at a controlled temperature in the presence of ascorbic acid led to the generation of oxygen vacancies where the concentration varied with the amount of ascorbic acid added. This led to a deliberate manipulation of the electrocatalytic activity towards oxygen reduction in alkaline media. Voltammetric measurements showed that the nanocomposites with a relatively high concentration of oxygen vacancies exhibited the best ORR activity among the series, as a result of deliberate manipulation of the binding interactions of oxygen species on the nanocomposite surfaces that was facilitated by partial charge transfer from oxygen-deficient TiO_2 to gold. The results further highlight the significance of metal-substrate interfacial interactions in the design and engineering of functional nanocomposites as effective catalysts for fuel cell electrochemistry.

2.5 References

(1) Wang YG, Yoon Y, Glezakou VA, Li J, Rousseau R. The role of reducible oxide-metal cluster charge transfer in catalytic processes: new insights on the catalytic mechanism of CO oxidation on Au/TiO_2 from ab initio molecular dynamics. *J Am Chem Soc.* **2013**; *135*, 10673-83.

(2) Liu X, Liu MH, Luo YC, Mou CY, Lin SD, Cheng H, et al. Strong metal-support interactions between gold nanoparticles and ZnO nanorods in CO oxidation. *J Am Chem Soc*. **2012**; 134, 10251-8.

(3) Jaksic MM, Botton GA, Papakonstantinou GD, Nan FH, Jaksic JM. Primary oxide latent storage and spillover enabling electrocatalysts with reversible oxygen electrode properties and the alterpolar revertible (PEMFC versus WE) cell. *J Phys Chem C*. **2014**; *118*, 8723-46.

(4) Sener T, Demirci UB, Gul OF, Ata A. Pd-MnO_2-Fe_2O_3/C as electrocatalyst for the formic acid electrooxidation. *Int J Hydrogen Energy*. **2015**; *40*, 6920-6.

(5) Duan ZY, Henkelman G. CO oxidation at the Au/TiO_2 boundary: the role of the Au/Ti 5c site. *ACS Catal*. **2015**; *5*, 1589-95.

(6) Widmann D, Behm RJ. Activation of molecular oxygen and the nature of the active oxygen species for CO oxidation on oxide supported Au catalysts. *Acc Chem Res*. **2014**; *47*, 740-9.

(7) Fu Q, Li WX, Yao YX, Liu HY, Su HY, Ma D, et al. Interface-confined ferrous centers for catalytic oxidation. *Science*. **2010**; *328*, 1141-4.

(8) Neophytides SG, Zafeiratos S, Papakonstantinou GD, Jaksic JM, Paloukis FE, Jaksic MM. Extended Brewer hypohyper-d-interionic bonding theory II. Strong metal-support interaction grafting of composite electrocatalysts. *Int J Hydrogen Energy*. **2005**; *30*, 393-410.

(9) Cheng NC, Liu J, Banis MN, Geng DS, Li RY, Ye SY, et al. High stability and activity of Pt electrocatalyst on atomic layer deposited metal oxide/nitrogen-doped graphene hybrid support. *Int J Hydrogen Energy*. **2014**; *39*, 15967-74.

(10) Comotti M, Li WC, Spliethoff B, Schuth F. Support effect in high activity gold catalysts for CO oxidation. *J Am Chem Soc*. **2006**; *128*, 917-24.

(11) Lin C, Song Y, Cao L, Chen S. Oxygen reduction catalyzed by Au-TiO_2 nanocomposites in alkaline media. *ACS Appl Mater Interfaces*. **2013**; *5*, 13305-11.

(12) Chen W, Ny D, Chen S. SnO_2-Au hybrid nanoparticles as effective catalysts for oxygen electroreduction in alkaline media. *J Power Sources*. **2010**; *195*, 412-8.

(13) Ma Z, Dai S. Chapter 1. Stabilizing gold nanoparticles by solid supports. In: Ma Z, Dai S, editors. "Heterogenous gold catalysts and catalysis." *Royal of Society of Chemistry*. **2014**. p. 1-26.

(14) Wu B, Zheng N. Surface and interface control of noble metal nanocrystals for catalytic and electrocatalytic applications. *Nano Today*. **2013**; *8*, 168-97.

(15) Melvin AA, Bharad PA, Illath K, Lawrence MP, Gopinath CS. Is there any real effect of low dimensional morphologies towards light harvesting? A case study of Au-rGO-TiO_2 nanocomposites. *ChemistrySelect*. **2016**; *5*, 917-23.

(16) Horvath A, Beck A, Sarkany A, Stefler G, Varga Z, Geszti O, et al. Silica-supported Au nanoparticles decorated by TiO_2: formation, morphology, and CO oxidation activity. *J Phys Chem B*. **2006**; *110*, 15417-25.

(17) Ma Z, Brown S, Howe JY, Overbury SH, Dai S. Surface modification of Au/TiO_2 catalysts by SiO_2 via atomic layer deposition. *J Phys Chem C*. **2008**; *112*, 9448-57.

(18) Huang X, Guo C, Zuo J, Zheng N, Stucky GD. An assembly route to inorganic catalytic nanoreactors containing sub-10-nm gold nanoparticles with anti-aggregation properties. *Small*. **2009**; *5*, 361-5.

(19) Kim J-H, Ishihara A, Mitsushima S, Kamiya N, Ota K-I. Catalytic activity of titanium oxide for oxygen reduction reaction as a non-platinum catalyst for PEFC. *Electrochim Acta*. **2007**; *52*, 2492-7.

(20) Cerri I, Nagami T, Davies J, Mormiche C, Vecoven A, Hayden B. Innovative catalyst supports to address fuel cell stack durability. *Int J Hydrogen Energy*. **2013**; 38, 640-5.

(21) Kim J-H, Chang S, Kim Y-T. Compressive strain as the main origin of enhanced oxygen reduction reaction activity for Pt electrocatalysts on chromium-doped titania support. *Appl Catal B Environ*. **2014**; *158-159*, 112-8.

(22) Wang N, Niu WH, Li LG, Liu J, Tang ZH, Zhou WJ, et al. Oxygen electroreduction promoted by quasi oxygen vacancies in metal oxide nanoparticles prepared by photoinduced chlorine doping. *Chem Commun*. **2015**; *51*, 10620-3.

(23) Myung JH, Shin TH, Huang XB, Carins G, Irvine JTS. Enhancement of redox stability and electrical conductivity by doping various metals on ceria, $Ce_{1-x}MxO_{2-delta}$ (M = Ni, Cu, Co, Mn, Ti, Zr). *Int J Hydrogen Energy*. **2015**; 40, 12003-8.

(24) Zana A, Rüdiger C, Kunze-Liebhäuser J, Granozzi G, Reeler NEA, Vosch T, et al. Core-shell TiO_2@C: towards alternative supports as replacement for high surface area carbon for PEMFC catalysts. *Electrochim Acta*. **2014**; *139*, 21-8.

(25) Esfandiar A, Irajizad A, Akhavan O, Ghasemi S, Gholami MR. Pd-WO_3/reduced graphene oxide hierarchical nanostructures as efficient hydrogen gas sensors. *Int J Hydrogen Energy*. **2014**; *39*, 8169-79.

(26) Pan X, Yang MQ, Fu X, Zhang N, Xu YJ. Defective TiO_2 with oxygen vacancies: synthesis, properties and photocatalytic applications. *Nanoscale*. **2013**; *5*, 3601-14.

(27) Linh NH, Nguyen TQ, Diño WA, Kasai H. Effect of oxygen vacancy on the adsorption of O_2 on anatase TiO_2(001): a DFT-based study. *Surf Sci*. **2015**; *633*, 38-45.

(28) Aschauer U, Chen J, Selloni A. Peroxide and superoxide states of adsorbed O_2 on anatase TiO_2(101) with subsurface defects. *Phys Chem Chem Phys*. **2010**; *12*, 12956-60.

(29) Zhu Q, Peng Y, Lin L, Fan C-M, Gao G-Q, Wang R-X, et al. Stable blue TiO_{2-x} nanoparticles for efficient visible light photocatalysts. *J Mater Chem A*. **2014**; *2*, 4429.

(30) Wajid Shah M, Zhu Y, Fan X, Zhao J, Li Y, Asim S, et al. Facile synthesis of defective TiO_{2-x} nanocrystals with high surface area and tailoring bandgap for visible-light photocatalysis. *Sci Rep* **2015**; *5*, 15804.

(31) Pan DC, Zhao NN, Wang Q, Jiang SC, Ji XL, An LJ. Facile synthesis and characterization of luminescent TiO_2 nanocrystals. *Adv Mater*. **2005**; *17*, 1991-5.

(32) Liu K, Song Y, Chen SW. Defective TiO_2-supported Cu nanoparticles as efficient and stable electrocatalysts for oxygen reduction in alkaline media. *Nanoscale*. **2015**; *7*, 1224-32.

(33) Antić Ž, Krsmanović RM, Nikolić MG, Marinović-Cincović M, Mitrić M, Polizzi S, et al. Multisite luminescence of rare earth doped TiO_2 anatase nanoparticles. *Mater Chem Phys*. **2012**; *135*, 1064-9.

(34) Nakamoto M, Yamamoto M, Fukusumi M. Thermolysis of gold(i) thiolate complexes producing novel gold nanoparticles passivated by alkyl groups. *Chem Commun*. **2002**, 1622-3.

(35) Pan XY, Xu Y-J. Fast and spontaneous reduction of gold ions over oxygen-vacancy-rich TiO_2: a novel strategy to design defect-based composite photocatalyst. *Appl Catal A Gen*. **2013**; *459*, 34-40.

(36) Dette C, Perez-Osorio MA, Kley CS, Punke P, Patrick CE, Jacobson P, et al. TiO_2 anatase with a bandgap in the visible region. *Nano Lett*. **2014**; *14*, 6533-8.

(37) Abd-Ellah M, Moghimi N, Zhang L, Thomas JP, McGillivray D, Srivastava S, et al. Plasmonic gold nanoparticles for ZnO-nanotube photoanodes in dye-sensitized solar cell application. *Nanoscale*. **2016**; *8*, 1658-64.

(38) Pan X, Xu Y-J. Defect-mediated growth of noble-metal (Ag, Pt, and Pd) nanoparticles on TiO_2 with oxygen vacancies for photocatalytic redox reactions under visible light. *J Phys Chem C*. **2013**; *117*, 17996-8005.

(39) Naldoni A, D'Arienzo M, Altomare M, Marelli M, Scotti R, Morazzoni F, et al. Pt and Au/TiO_2 photocatalysts for methanol reforming: role of metal nanoparticles in tuning charge trapping properties and photoefficiency. *Appl Catal B Environ*. **2013**; *130-131*, 239-48.

(40) Randorn C, Irvine JTS. Synthesis and visible light photoactivity of a high temperature stable yellow TiO_2 photocatalyst. *J Mater Chem*. **2010**; *20*, 8700.

(41) Altenbach C, Flitsch SL, Khorana HG, Hubbell WL. Structural studies on transmembrane proteins. 2. Spin labeling of bacteriorhodopsin mutants at unique cysteines. *Biochemistry*. **1989**; *28*, 7806-12.

(42) Galli C, MacArthur R, AbuSoud HM, Clark P, Stuehr DJ, Brudvig GW. EPR spectroscopic characterization of neuronal NO synthase. *Biochemistry*. **1996**; *35*, 2804-10.

(43) Ahmad R, Kuppusamy P. Theory, instrumentation, and applications of electron paramagnetic resonance oximetry. *Chem Rev*. **2010**; *110*, 3212-36.

(44) Baumann SO, Elser MJ, Auer M, Bernardi J, Husing N, Diwald O. Solid-solid interface formation in TiO_2 nanoparticle networks. *Langmuir*. **2011**; *27*, 1946-53.

(45) Pascutti PG, Ito AS. EPR study of melanin protein-interaction - photoinduced free-radicals and progressive microwave-power saturation. *J Photochem Photobiol B Biol*. **1992**; *16*, 257-66.

(46) Judeikis HS. Errors in the evaluation of moments of a paramagnetic resonance line. *J Appl Phys*. **1964**; *35*, 2615.

(47) Palanisamy B, Babu CM, Sundaravel B, Anandan S, Murugesan V. Sol-gel synthesis of mesoporous mixed Fe_2O_3/TiO_2 photocatalyst: application for degradation of 4-chlorophenol. J Hazard Mater **2013**; *252-253*, 233-42.

(48) Wang Y, Sun H, Tan S, Feng H, Cheng Z, Zhao J, et al. Role of point defects on the reactivity of reconstructed anatase titanium dioxide (001) surface. *Nat Commun*. **2013**; *4*, 2214.

(49) Zoulalian V, Zurcher S, Tosatti S, Textor M, Monge S, Robin JJ. Self-assembly of poly(ethylene glycol)-poly(alkyl phosphonate) terpolymers on titanium oxide surfaces: synthesis, interface characterization, investigation of nonfouling properties, and long-term stability. *Langmuir*. **2010**; *26*, 74-82.

(50) Melvin AA, Illath K, Das T, Raja T, Bhattacharyya S, Gopinath CS. M-Au/TiO_2 (M = Ag, Pd, and Pt) nanophotocatalyst for overall solar water splitting: role of interfaces. *Nanoscale*. **2015**; *7*, 13477-88.

(51) Chang FW, Yu HY, Roselin LS, Yang HC, Ou TC. Hydrogen production by partial oxidation of methanol over gold catalysts supported on TiO_2-MO_x (M = Fe, Co, Zn) composite oxides. *Appl Catal A. Gen*. **2006**; *302*, 157-67.

(52) Morad M, Sankar M, Cao EH, Nowicka E, Davies TE, Miedziak PJ, et al. Solvent-free aerobic oxidation of alcohols using supported gold palladium nanoalloys prepared by a modified impregnation method. *Catal Sci Technol*. **2014**; *4*, 3120-8.

(53) Yang K, Zhang YF, Li Y, Huang P, Chen X, Dai WX, et al. Insight into the function of alkaline earth metal oxides as electron promoters for Au/TiO_2 catalysts used in CO oxidation. *Appl Catal B Environ*. **2016**; *183*, 206-15.

(54) Trasatti S, Petrii OA. Real surface-area measurements in electrochemistry. *Pure Appl Chem*. **1991**; *63*, 711-34.

(55) Zhou ZY, Kang XW, Song Y, Chen SW. Enhancement of the electrocatalytic activity of Pt nanoparticles in oxygen reduction by chlorophenyl functionalization. *Chem Commun*. **2012**; *48*, 3391-3.

(56) Jašin D, Abu-Rabi A, Mentus S, Jovanović D. Oxygen reduction reaction on spontaneously and potentiodynamically formed Au/TiO_2 composite surfaces. *Electrochim Acta*. **2007**; *52*, 4581-8.

(57) Hu PG, Song Y, Chen LM, Chen SW. Electrocatalytic activity of alkyne-functionalized AgAu alloy nanoparticles for oxygen reduction in alkaline media. *Nanoscale*. **2015**; *7*, 9627e36.

(58) Tan S-j, Wang B. Active sites for adsorption and reaction of molecules on rutile TiO_2(110) and anatase TiO_2(001) surfaces. *Chin J Chem Phys*. **2015**; *28*, 383-95.

(59) Sabatier P. Announcement. Hydrogenation and dehydrogenation for catalysis. *Ber Dtsch Chem Ges*. **1911**; *44*, 1984-2001.

(60) dos Reis, F. V. E.; Antonin, V. S.; Hammer, P.; Santos, M. C.; Camargo, P. H. C. *J Catal*. **2015**; *326*, 100- 106.

(61) Ruiz-Camacho, B.; Martínez-Álvarez, O.; Rodríguez-Santoyo, H. H.; Granados-Alejo, V. *J Electroanal Chem*. **2014**; *725*, 19-24.

(62) Huang, D.; Zhang, B.; Bai, J.; Zhang, Y.; Wittstock, G.; Wang, M.; Shen, Y. *Electrochim Acta*. **2014**, *130*, 97-103.

(63) Baez, V. B.; Pletcher, D. *J Electroanal Chem*. **1994**, *377*, 231-240.

(64) Lin, H.; Tang, W.; Kleiman-Shwarsctein, A.; McFarland, E. W. *J Electrochem Soc*. **2008**, *155*, B200-B206.

(65) Jin, C.; Cao, X. C.; Lu, F. L.; Yang, Z. R.; Yang, R. Z. *ACS Appl Mater Interfaces*. **2014**, *6*, 847-853.

Chapter 3

Impacts of the transition metal oxide support for oxygen reduction reaction

Abstract

In metal nanoparticle/oxide nanocomposites, the reducibility of the support plays an important role in determining the activity of the entire system. There is a general understanding that reducible oxides are far more reactive than nonreducible oxides because of the presence of defects sites or oxygen vacancies. Typically, these defects cause a stronger interaction between the metal nanoparticle and the reducible oxide making them better candidates for fuel cell reactions. They also will cause a partial charge transfer to the metal nanoparticle, which causes a lower binding energy of gas molecules in electrocatalysis. In this study we looked at the role of the support in studying gold nanoparticles photo-deposited on different oxide materials. We synthesized TiO_2 nanoparticles and SiO_2 nanoparticles and deposited gold nanoparticles of different sizes using different irradiation times. The structure of the nanocomposites was determined using TEM and XRD. TEM showed that Au/TiO_2 30 min sample was composed of two regions with anatase TiO_2 and Au facets. XRD mainly showed Au peaks and showing that the gold tended to be smaller on the SiO_2 samples. Oxygen vacancies were studied Raman, EPR, and XPS which afforded that they were caused by Au deposition and a partial charge transfer to the Au occurred on

the TiO_2 samples. The SiO_2 samples however have no indication of a defect/reduced state. The contribution of the oxygen vacancies was studied during ORR catalysis using RRDE and Tafel analysis. Overall, because of the oxygen vacancies, the TiO_2 samples out-performed the SiO_2 samples.

3.1 Introduction

Recently, there is an increase in research in fuel cells, however due to the sluggish kinetics of the oxygen reduction reaction at the cathode, the commercialization of these devices has been hindered. In addition, the current most effective catalyst is platinum which is very rare and expensive. Therefore, new catalysts are needed to replace platinum.[1] Nanocomposites based on metal nanoparticles supported on transition metal oxide surfaces have been used extensively as effective catalysts for the oxygen reduction reaction as well. This has been ascribed largely to the strong metal-support interactions.[2-7] They are a good replacement for the commercial activated carbon supports because of their stability under harsh conditions whereas the carbon supports will oxidize and loose electrochemical surface area over time.[8]

Previous studies have shown that the interaction between the metal nanoparticle and the support can affect catalytic activity.[9] For instance, Li and coworkers demonstrated that gold atoms have different favorable binding patterns on anatase and brookite TiO_2. This affects the growth of nanoparticles on the surface and therefore the catalytic activity towards CO oxidation.[10] Lui et al. showed that by changing the crystal

facet of TiO_2, catalytic activity towards CO oxidation changes because the facet dictates the activation of O_2.[11]

Whereas there has been some advancement in studying the metal-support interactions through electron microscopy[12], there is still some information needed to deduce the interaction between metal nanoparticles and transition metal oxide supports during catalysis and electrocatalysis. This interaction has shown to affect the kinetics of the oxygen reduction reaction. Lin et al. prepared a series of $AuTiO_2$ nanocomposites and identified an optimal gold loading for maximal activity towards oxygen reduction reactions (ORR), which was accounted for by the dependence of surface OH concentration on gold contents.[13] In addition, Sweeney et al. synthesized Au/TiO_2 nanocomposites with varying concentrations of oxygen vacancies and determined an optimal concentration of oxygen vacancies that influenced the binding of oxygen to the Au/TiO_2 interface.[7]

Oxygen-deficient oxides have been shown to improve the oxygen reduction reaction in past studies. Ji et al. deposited platinum nanoparticles oxygen vacancy-treated TiO_2 nanofibers and the onset potential for the oxygen reduction reaction increased and the stability for the reaction improved.[14] Xu et al. deposited platinum nanoparticles on cerium oxide nanoparticles with a lot of oxygen vacancies in the CeO_2 nanoparticles. The mass activity improved by 50% and it proved to be more durable than Pt/C.[15]

In addition to manipulating the support, the reducibility of the support has played a role in metal deposition and catalysis. Fang and coworkers made a series of

gold nanoclusters supported on different oxides and studied the effect of temperature on size of particles and the catalytic efficiency towards two organic reactions. It was shown that the gold nanoclusters supported by TiO_2 samples showed no increase in particle size after heat treatment and showed the highest catalytic activity towards the two organic reactions.[16] Lu and coworkers treated samples of Degussa P25 powder with H_2 at room temperature to understand structural and defective changes in the samples. They did this using XRD, FT-IR, Raman and UV-vis, and TEM. They were able to show that the resulting structures formed a core-shell structure with good photocatalytic activity.[17]

However, there is needed a deeper understanding of how the oxide influences the reactivity of deposited nanoparticles. Because reaction conditions such as heat can change the size of gold nanoparticles, we needed a synthesis method that allows us to control the size of gold nanoparticles on both types of supports. We chose photodeposition because it allows us to control both the size of gold nanoparticles and oxygen vacancies in oxide supports. Pan and Xu were able to show the formation of oxygen vacancies under UV light in an oxygen-rich environment.[18] Herein, we report on the role of the support in the interaction between gold nanoparticles and two supports: TiO_2 nanoparticles (a reducible oxide) and SiO_2 (a non-reducible oxide) in the oxygen reduction reaction.

3.2 Experimental

3.2.1 Materials.

Titanium(IV)-tert-butoxide (97%, Sigma-Aldrich), gold(III) chloride ($AuCl_3$, Sigma-Aldrich), oleic acid (≥99%, Sigma-Aldrich), 3-chloroaniline (≥99.0%, Sigma-Aldrich), and tetraethyl orthosilicate (98%, Acros Organics). Solvents were purchased from typical commercial sources at their highest purity and used without further treatment. Water was supplied from a Barnstead Nanopure Water System (18.3 MΩ cm).

3.2.2 Synthesis of TiO_2 nanoparticles.

Synthesis has been modified from a previous study[19], and has been used in a previous publication.[7] In brief, 0.0503 mL of 3-chloroaniline, was dissolved in 5 mL of milliq water and placed in a Teflon-lined autoclave. 0.090 mL of Ti(IV)-*tert*-butoxide and 0.050 mL of oleic acid were dissolved in toluene and added to the same Teflon-lined autoclave. The bi-phasic reaction was heated at 180°C for 12 h. The liquids were evaporated under rotary evaporation, and the brown solid was washed extensively with methanol. The brown solid was then dried under vacuum and used as prepared.

3.2.3 Synthesis of SiO_2 nanoparticles.

Synthesis of SiO_2 was performed by modifying a previous method.[20] In brief, 25 mL of ethanol was dissolved in 100 mL of milliq water. This solution was sonicated for 10 min. Then, 0.965 mL of tetraorthosilicate was added to the mixture and this was sonicated for 20 min. Finally, 56 mL of ammonia hydroxide was added, and the mixture

was sonicated for 60 min. The solution was evaporated off under rotary evaporation and followed by washing with water. The white powder was then vacuum dried and used as prepared.

3.2.4 Photo-deposition of gold on oxides.

A reaction flask/condenser was attached and secured to a water cooling system with a shaker. Then 5 mg of the oxide was added to the flask followed by 20 mL of 10 mM $AuCl_3$. The shaker was turned on to evenly disperse the oxide particles. Then 0.2 mL of methanol was added, and the reaction was irradiated with 100 W of UV-light at 365 nm. The reaction was allowed to proceed for 10 min and 30 min (samples are designated as such). The precipitate was centrifuged down, washed with water, and vacuum dried and further used for experiments.

3.2.5 Characterization.

The sample morphologies were examined with a transmission electron microscope (TEM, Philips CM300) operated at 300 kV. X-ray photoelectron spectroscopic (XPS) measurements were carried out with a PHI 5400/XPS instrument equipped with an Al K_α source operated at 350 W and10^{-9} Torr. Diffuse reflectance UV-vis spectra were acquired with a Perkin-Elmer Lambda 35 spectrometer. EPR measurements were prepared by packing a glass capillary tube and sealing off the open end with a Bunsen burner. The capillary was placed in the quartz EPR tube (Wilmad, 4 mm outer diameter). Spectra were recorded at room temperature with a Bruker EMX

EPR spectrometer operating at the X-band frequency (~9.4 GHz) using an ER 4122SHQE resonator (Bruker). All spectra were recorded at a power of 1 mW, a modulation amplitude of 1 G, and a modulation frequency of 100 KHz. Signal intensity was normalized to mass of sample added to the capillary tube.[7] X-ray diffraction (XRD) measurements were performed with a Rigaku Miniflex powder diffractometer using Cu Kα radiation with a Ni filter (λ = 0.154059 nm at 30 kV and 15 mA) that features a detection limit of 0.04°. Raman characterization was performed on an inVia Renishaw Raman spectrometer using a HPNIR diode laser operated at 785 nm, HeNe ion excitation source operated at 663 nm, and Argon ion excitation source operated at 514 nm.

3.2.6 Electrochemistry.

Electrochemical experiments were carried out with a CHI 710 Electrochemical Workstation with a glassy-carbon disk and gold ring electrode, a platinum counter electrode, and a Ag/AgCl reference electrode. A catalyst ink was prepared by adding the Au/oxide nanocomposites prepared above and 4 times the amount of oxide of carbon black dispersed in a calculated amount of ethanol and 1% of mL of ethanol of Nafion (corresponding to a nanocomposite concentration of 20 wt.%). The ink was then dropcast onto the glassycarbon disk at a nanocomposite loading of ca. 20 mg, and dried in air before being immersed into electrolyte solutions for data acquisition. The Ag/AgCl electrode was calibrated against a reversible hydrogen electrode (RHE), and the potentials were all referred to this RHE electrode.

3.3 Results and Discussion

3.3.1 Structural Characterization.

Representative images of the structural morphology of the Au/TiO_2 30 min sample as portrayed through TEM and HRTEM measurements are shown in Figure 3.1 (A) – (D). Figures 3.1 (A) and (B) shows two main regions in the sample: one of lower electron density with less defined particles and one of higher electron density with more defined particles. The lower electron density region can be ascribed to the TiO_2 nanoparticles which are aggregated with an average size around 25 nm. The higher electron density area can be ascribed to gold nanoparticles with an average size of around 5 nm. Both regions however show aggregation of particles. In Figure 3.1 (C), the HRTEM image of the lower electron density area shows lattice fringes at 0.37 nm which corresponds to the (101) facet for anatase TiO_2.[21-23] Looking at an HRTEM image of the higher electron density area (Figure 3.1 (D)), there appears to be lattice fringes with a value of 0.224 nm which corresponds to the Au (111) facet.[23-25]

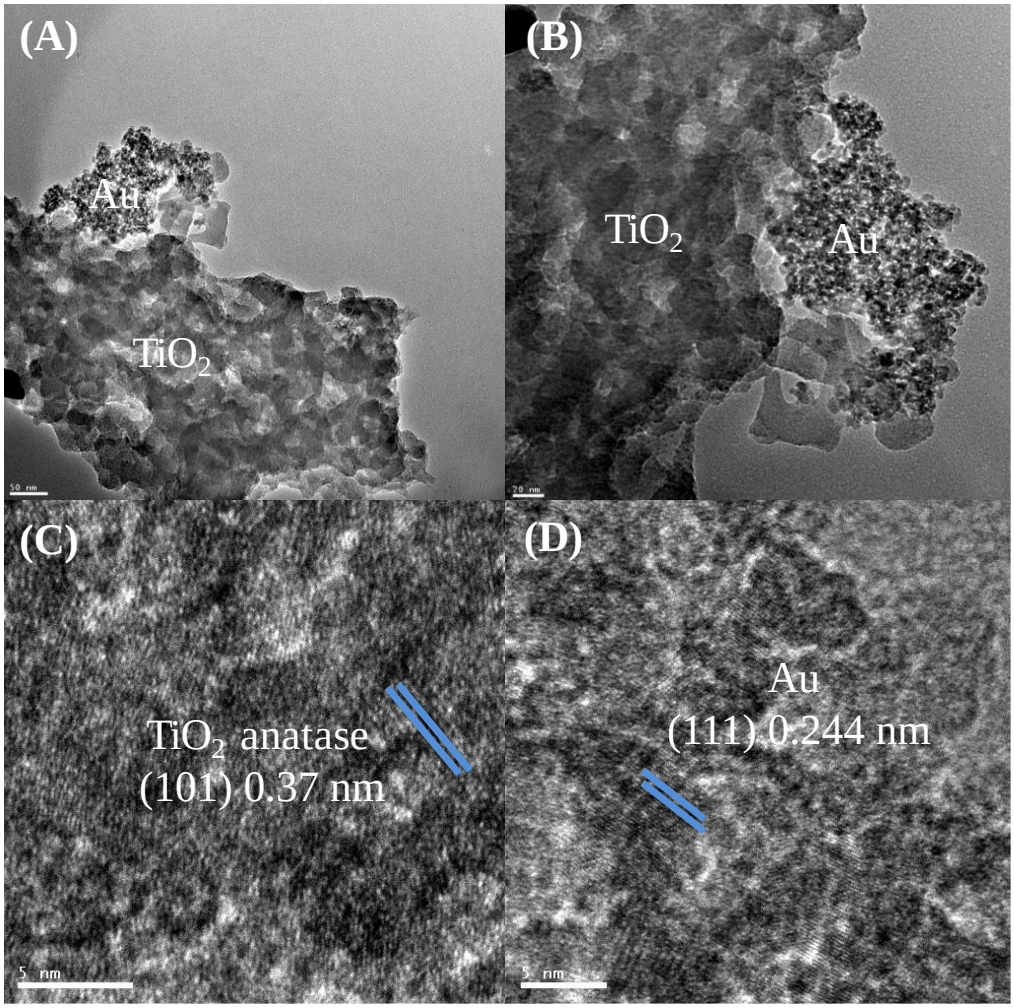

Figure 3.1 (A) and (B) - TEM images of Au/TiO_2 30 min sample, **(C)** HRTEM image of TiO_2 region of Au/TiO_2 30 min sample, and **(D)** HRTEM image of Au region of Au/TiO_2 30 min sample.

Structural assignments were further manifested in power x-ray diffractions measurements (Figure 3.2). One peak for SiO_2 nanoparticles is found at 22.7° which is attributed to amorphous silicon dioxide.[26] TiO_2 nanparticles show peaks at 25.2, 38.0, 48.0, 54.7, and 62.8° which correspond to the (101), (004), (200), (211), and (220)

facets of anatase TiO_2 respectively (JCPDS Card no. 21-1272). When gold is deposited onto the oxides, the peaks for TiO_2 and SiO_2 disappear and peaks are shown at 38.0, 44.5, 64.6, 77.4, and 81.9° which correspond to the (111), (200), (220), (311), and (222) facets of Au respectively (JCPDS Card No. 4-784). From the Debye Scherrer equation, the particle sizes were estimated to be 5.4 nm, 24.2 nm, 19.7 nm, 22.4, and 14.1 nm for TiO_2, Au/TiO_2 30 min, Au/TiO_2 10 min, Au/SiO_2 30 min, and Au/SiO_2 10 min samples respectively. The size of SiO_2 was not able to be determined because of the large peak broadening from the particles.[27] The discrepancy between the TiO_2 nanoparticle size from TEM and XRD measurements is potentially due to the discrepancy between the grain size (measured by TEM) and coherent scattering domain size (measured by XRD).[28] As the photodeposition time increases, the gold particle size increases. However, it seems that the average size of the gold nanoparticles is slightly smaller on the SiO_2 compared to those on the TiO_2. This could be due to gold have a stronger affinity to defects and nucleate and grow from solely the defects instead of the rest of the surface.[29,30]

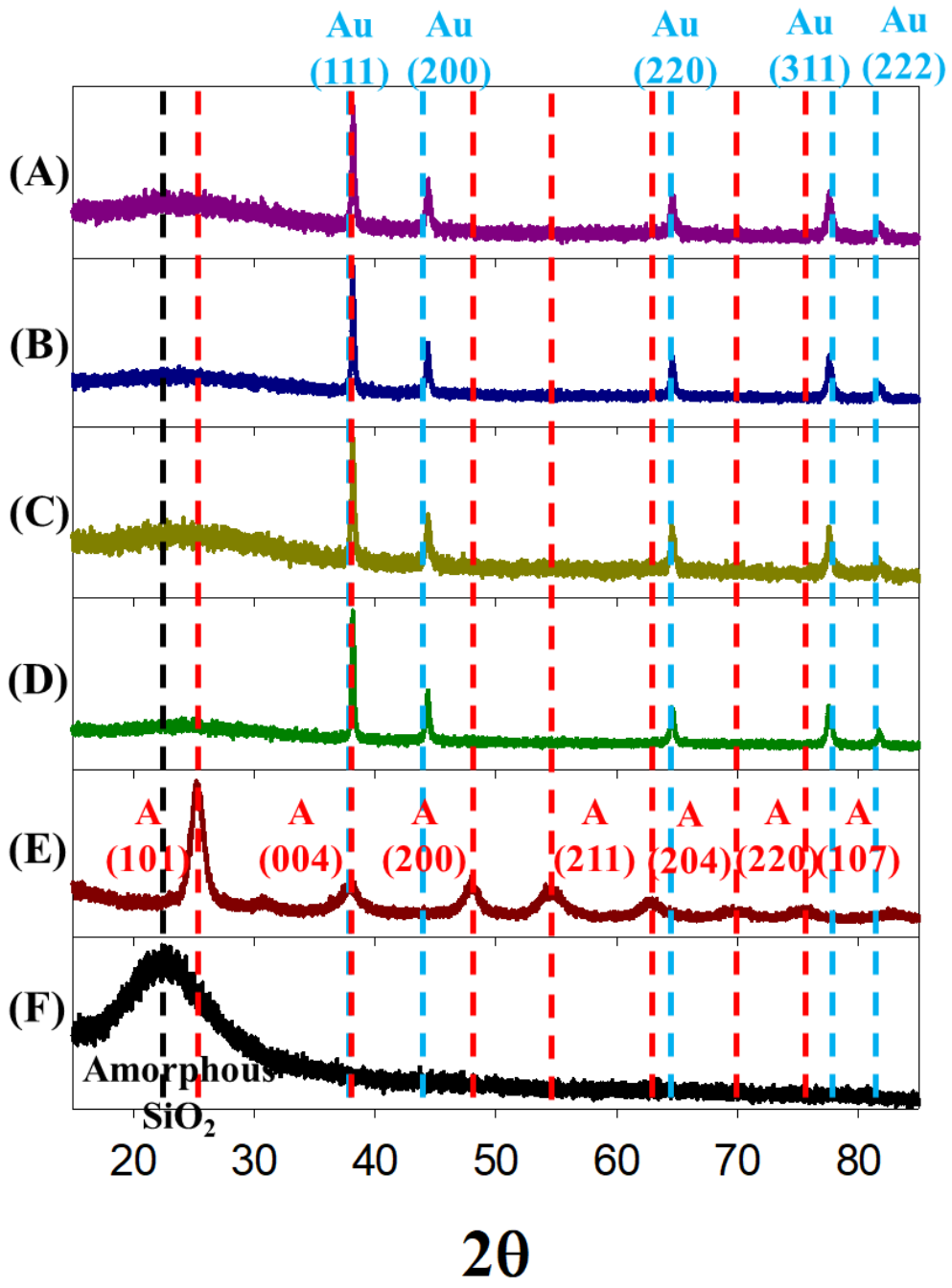

Figure 3.2 Powder x-ray diffraction of **(A)** Au/SiO_2 10 min, **(B)** Au/SiO_2 30 min, **(C)** Au/TiO_2 10 min, **(D)** Au/TiO_2 30 min, **(E)** TiO_2, and **(F)** SiO_2.

Raman measurements were done because substrate peaks were not shown after gold deposition in XRD measurements more information was needed on structural change due to the interaction between gold and the oxides. Figure 3.3 is a Raman spectrum of all the samples. The SiO_2 samples do not show sufficient signal, except for the Au/SiO_2 10 min sample which shows peaks at 270, 1170, and 1300 cm^{-1} which are ascribed to vibrations in the silica network.[31] Bare TiO_2 nanoparticles show peaks at 407, 520, and 635 cm^{-1} which can attributed to the O-Ti-O bending mode, and the one and two dimensional Ti-O stretching modes of anatase crystal structure respectively.[32] The Au/TiO_2 30 min and Au/TiO_2 10 min samples both show these peaks indicating that the gold does not change the crystal structure of the TiO_2 that much. However, two new peaks appear at 443 and 710 cm^{-1} after the gold is deposited onto the TiO_2. This has previously been prescribed to titanate peaks which could show the partial negative charge due to the formation of Ti^{3+} species (see XPS).[33] These peaks are not present in the SiO_2 samples indicating that photodeposition does not induce defects into the SiO_2 lattice (see XPS).

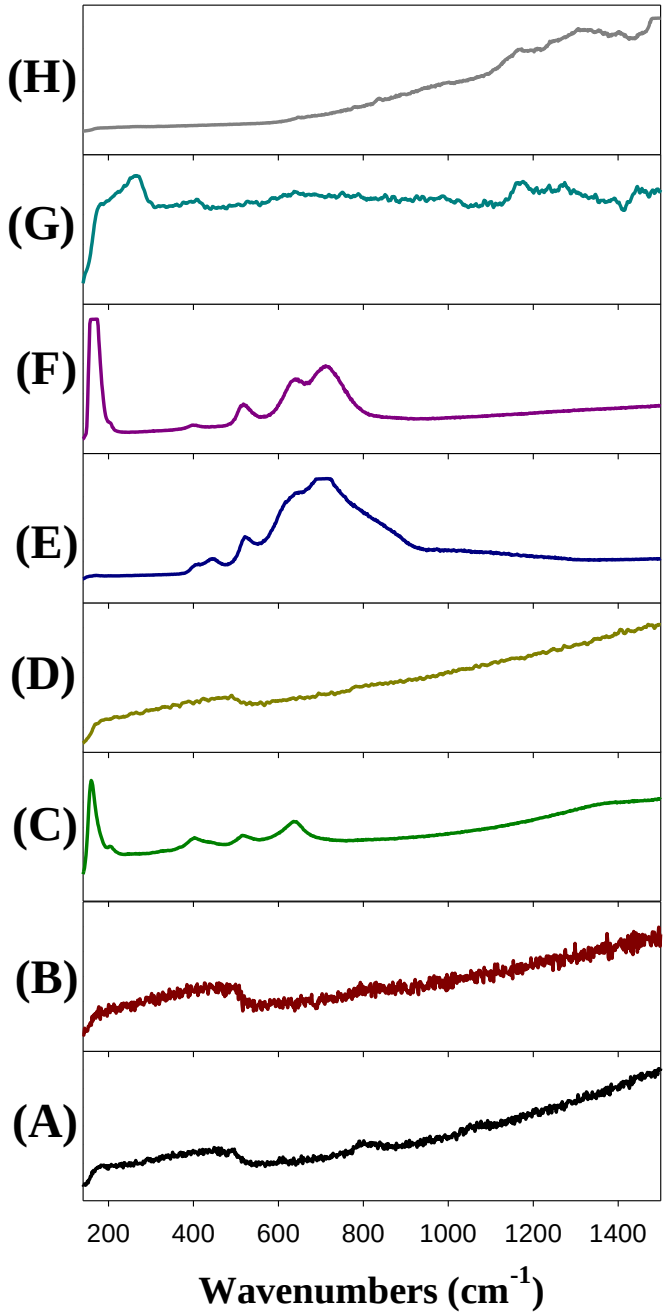

Figure 3.3 Raman spectra of all samples **(A)** 514 nm, **(B)** 663 nm, **(C)** TiO_2, **(D)** SiO_2, **(E)** Au/TiO_2 30 min, **(F)** Au/TiO_2 10 min, **(G)** Au/SiO_2 30 min, and **(H)** Au/SiO_2 10 min

3.3.2 Electronic Characterization.

The optical properties of the Au/oxide samples were tested with diffuse reflectance measurements (Figure 3.4). TiO_2 nanoparticles have an exponential decay absorption profile. This is due to the presence of defects in the TiO_2 nanoparticles (see EPR and XPS data).[34,35] A peak also appears around 450 nm which could possibly be due to the luminescence properties of TiO_2.[36] When gold is deposited onto the samples, there seems to be a red shift in this peak to around 475 nm and a small peak at 590 nm which is due to the surface plasmon resonance of gold.[37] The Au_SiO_2 samples seem to have no peaks and no exponential decay because the SiO_2 substrate has no absorption in the visible range.[38]

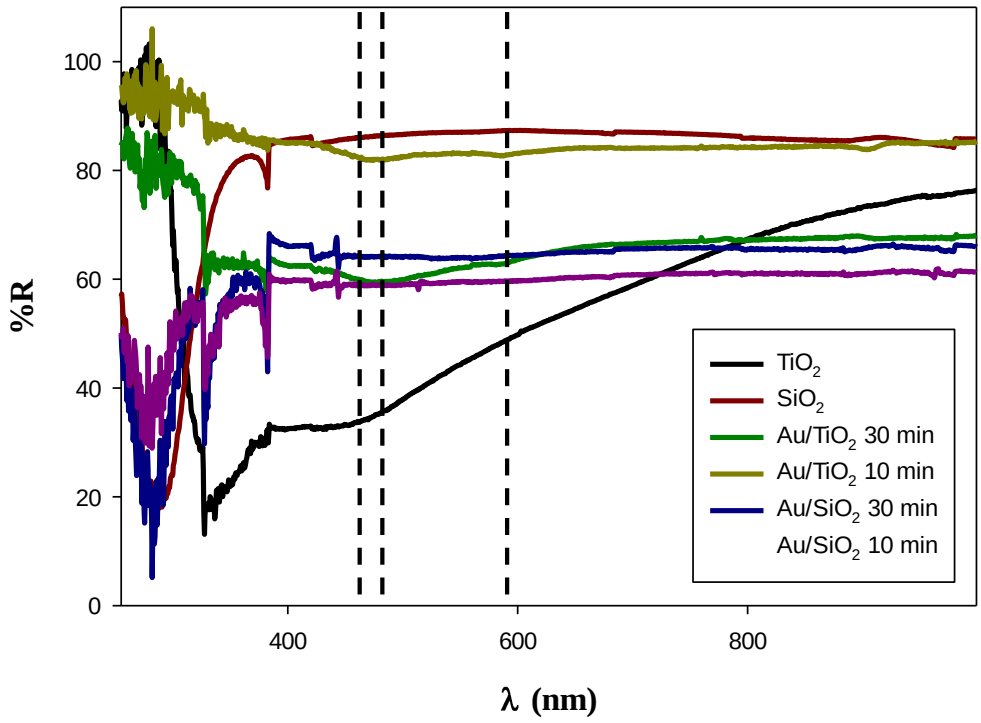

Figure 3.4 DRS of all samples.

The presence of oxygen vacancies was determined using EPR measurements (Figure 3.5). TiO_2 nanoparticles have a peak at 3375 G which corresponds to a g value of 2.0013. This peak is due to the presence of oxygen vacancies where an electron becomes trapped in the vacancy and produces a signal similar to that of an oxygen radical.[39,40] The SiO_2 nanoparticles have no signal because they have no oxygen vacancies. This is due to the fact that Si only has one oxidation state, 4^+.[41] This data verifies the reducibility of TiO_2 and non-reducibility of SiO_2. Once the gold is deposited on SiO_2, there seems to be no EPR signal. This means that gold does not generate oxygen generate oxygen vacancies in SiO_2. However, when the gold is

deposited on the TiO_2, the signal disappears. This could be due to the high conductivity of the gold and the presence of oxygen weakening the oxygen vacancy signal.[42] These limitations do not affect XPS results and we were able to see the presence of gold-induced defects.

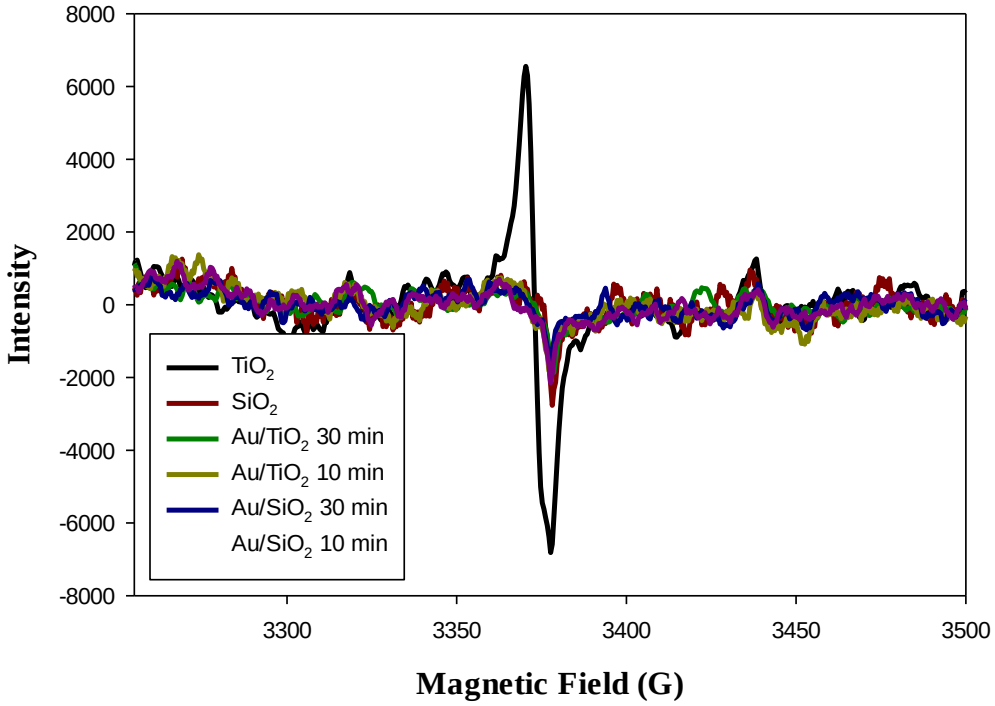

Figure 3.5 EPR of all samples.

Electronic characterizations and effect of photodeposition on the oxides were further studied using XPS (Figure 3.6). Peaks appeared at ~85, ~100, ~285, ~460, and 530 eV which correspond to the elements Au, Si, C, Ti, and O respectively.[43,44]

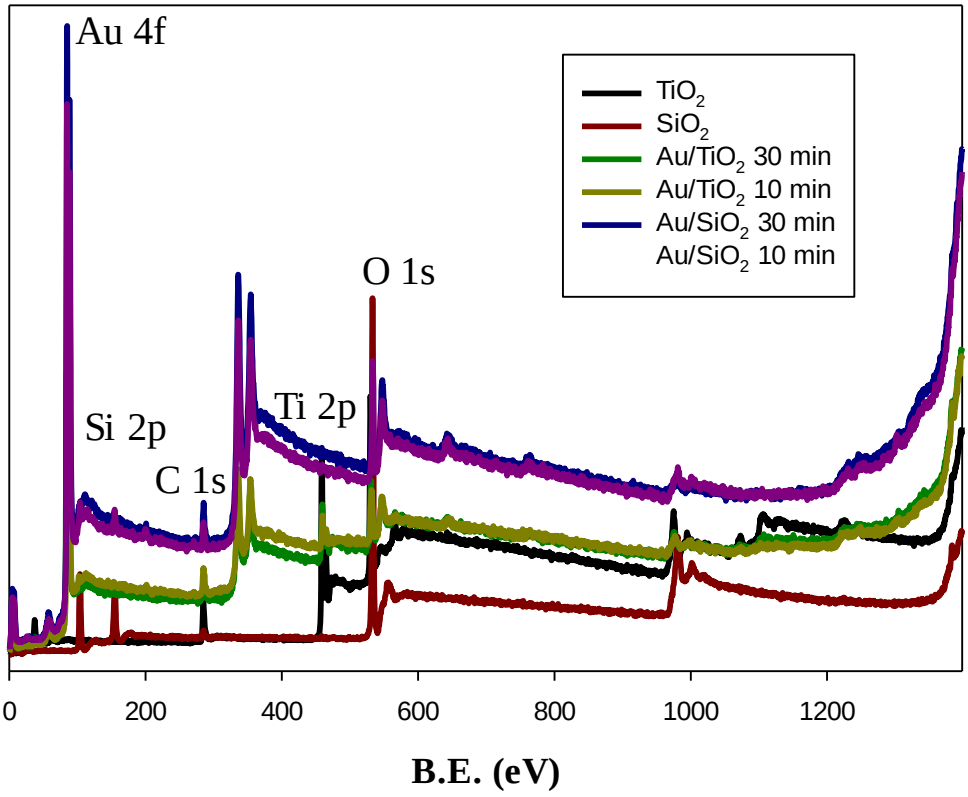

Figure 3.6 XPS survey spectra of all samples.

Figure 3.7 shows the high-resolution scans of Au 4f (left column), O 1s (middle column), and Ti 2p (right column) of TiO_2 nanoparticles and Au/TiO_2 samples. In the Au 4f high resolution spectrum both Au/TiO_2 samples have one pair of peaks present. The peak positions are 87.75 and 84.13 eV and 87.72 and 84.09 eV for Au/TiO_2 10 min and Au/TiO_2 30 min respectively. These peak positions seem to fall near Au^0 signifying that the photodeposition converted the Au^{3+} from $AuCl_3$ to Au^0.[45] In the high-resolution scan for the O 1s spectra, the TiO_2 samples have two peaks at 531.34 and 529.87 eV

for TiO_2, 532.23 and 530.74 eV for Au/TiO_2 30 min, and 532.55 and 531.19 eV for Au/TiO_2 10 min corresponding to surface adsorbed OH groups and lattice oxygen respectively.[46] The peak positions seem to blue shift after the photodeposition of gold whereas the photodeposition time increases, the binding energy increases. This could be due to the formation of oxygen vacancies in the TiO_2.[18] In high resolution Ti 2p scans, there appears to be a doublet for the bare TiO_2 nanoparticles and two sets of doublets when Au is deposited onto the surface. The peak positions are 463.83 eV and 458.13 eV for bare TiO_2; 464.95 eV, 459.18 eV, 463.80 eV, and 457.59 eV for Au/TiO_2 10 min; and 465.01 eV, 459.23 eV, 464.24 eV, and 457.66 eV for Au/TiO_2 30 min. The Ti^{4+} state occurs at ~465 and ~459 eV and the Ti^{3+} state occurs at ~463 and ~457 eV.[47] It seems that the bare TiO_2 started off at a reduced state with a mix of Ti^{4+} and Ti^{3+}. Once the gold is photo-deposited onto the TiO_2, there seems to be a blue-shift in the major peak where it falls near the binding energy of Ti^{4+} and the smaller pair of peaks fall near the Ti^{3+} state. The amount of Ti^{3+} is 0%, 11%, and 14% for TiO_2, Au/TiO_2 10 min, and Au/TiO_2 30 min respectively. The Ti^{3+} seems to increase slightly as the photodeposition time increases, therefore the photodeposition time affords more oxygen vacancy formation. In addition, the Ti peaks in the gold deposited samples have higher binding energies because of the charge transfer from Ti to Au which verifies the Au data.[48-50]

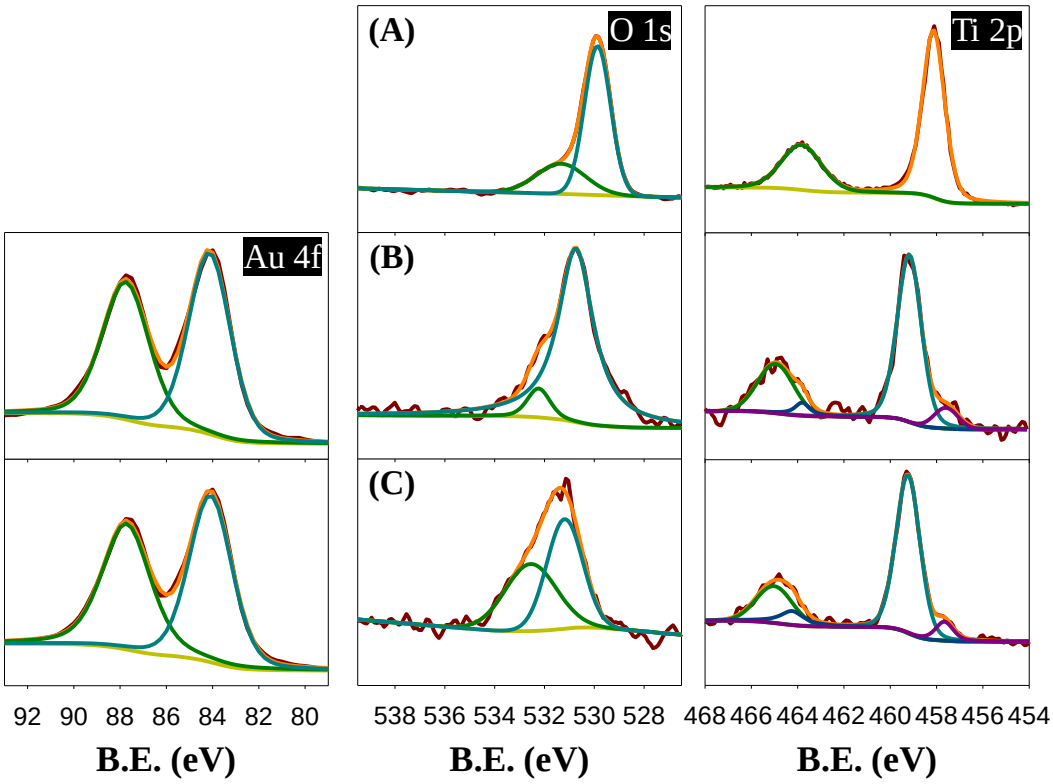

Figure 3.7 High resolution Au 4f, O 1s, and Ti 2p spectra of **(A)** TiO_2, **(B)** Au/TiO_2 30 min, and **(C)** Au/TiO_2 10 min

In contrast, Figure 3.8 shows the high-resolution spectra of the SiO_2 samples. In the left column, the high-resolution Au 4f spectra are shown with both samples have 1 pair of peaks at 87.72 and 84.09 eV for Au/SiO_2 10 min, and 87.81 and 84.19 eV for Au/SiO_2 30 min. These samples' peak positions are very similar to that of the TiO_2 samples meaning that these samples as well have reduced gold. In the middle column, the high resolution spectra for O 1s are shown with one peak for all samples at 533.07 eV for SiO_2, 532.63 eV for Au/SiO_2 30 min, and 533.23 eV for Au/SiO_2 10 min corresponding to lattice oxygen in the SiO_2 crystal lattice.[51] Finally, in the right column,

the high resolution Si 2p spectra are shown with one peak for all samples at 103.11, 102.87, and 103.02 eV corresponding to SiO_2, Au/SiO_2 30 min, and Au/SiO_2 10 min samples respectively that corresponds to lattice Si.[52,53] All of these peak positions are very similar to each meaning that there is no charge transfer in the SiO_2 samples.

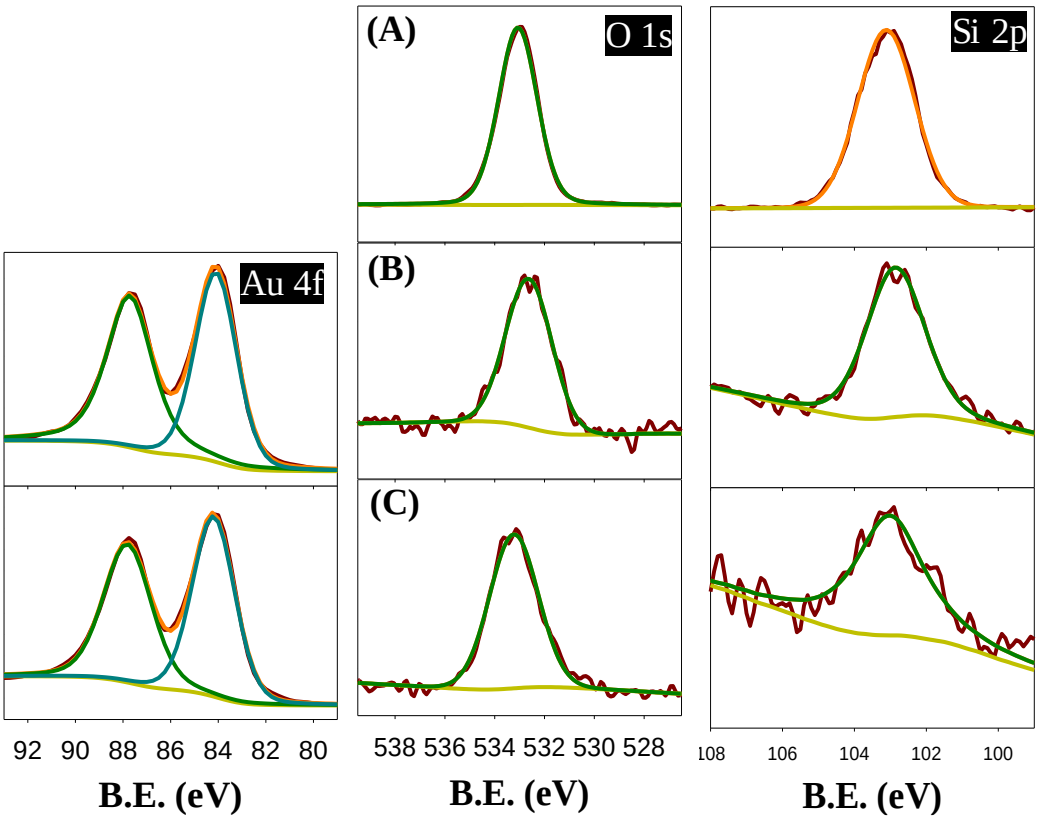

Figure 3.8 High resolution Au 4f, O 1s, and Si 2p spectra of **(A)** TiO_2, **(B)** Au/SiO_2 30 min, and **(C)** Au/SiO_2 10 min

3.3.3 Electrocatalytic Activity.

Cyclic voltammetry was performed in a N_2 saturated 0.1 M KOH solution at a scan rate of 10 mV/s (Figure 3.9). The reduction peak at 1 V vs. RHE is ascribed to the reduction of the AuO monolayer on the surface that formed at 1.3 V vs. RHE.[54,55] From this peak the electrochemical surface area can be calculated[56] to yield 0.1665, 0.2333, 0.0972, and 0.0726 cm^2 for Au/TiO_2 30 min, Au/TiO_2 10 min, Au/SiO_2 30 min, and Au/SiO_2 10 min respectively. The Au/TiO_2 10 min sample has the highest electrochemical surface area which contributes to its overall activity.[57] The defect data confirmed in the TiO_2 samples also contributes to the higher surface area.

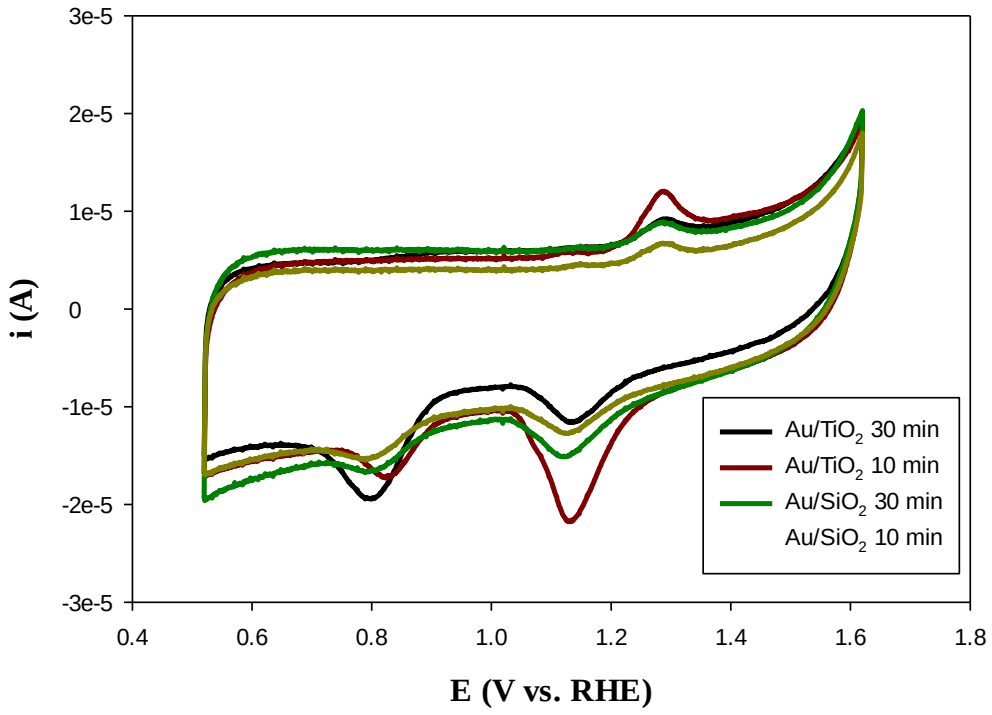

Figure 3.9 Steady-state cyclic voltammagrams of Au/oxide composites in N_2 saturated 0.1 M KOH solution at a scan rate of 10 mV/s.

This was further revealed in studying the oxygen reduction reaction by using RRDE measurements in an O_2 saturated 0.1 M KOH solution at a scan rate of 10 mV/s (Figure 3.10**)**. From the voltammagrams, the onset potential for the reaction is 0.90, 0.92, 0.88, 0.87 V vs. RHE for Au/TiO_2 30 min, Au/TiO_2 10 min, Au/SiO_2 30 min, and Au/SiO_2 10 min respectively with Au/TiO_2 10 min having the closest onset potential to the standard reduction potential of the conversion of O_2 to H_2O at 1.229 V vs. RHE.[58] All curves show apparent activity for the reaction with the ring current being 4x lower than the disk current in magnitude showing that the formation of hydrogen peroxide is the minor pathway. However, there is crossing of the disk current in all the samples showing that the mass transport is affecting the kinetics of the reaction decreasing the limiting current.[59,60]

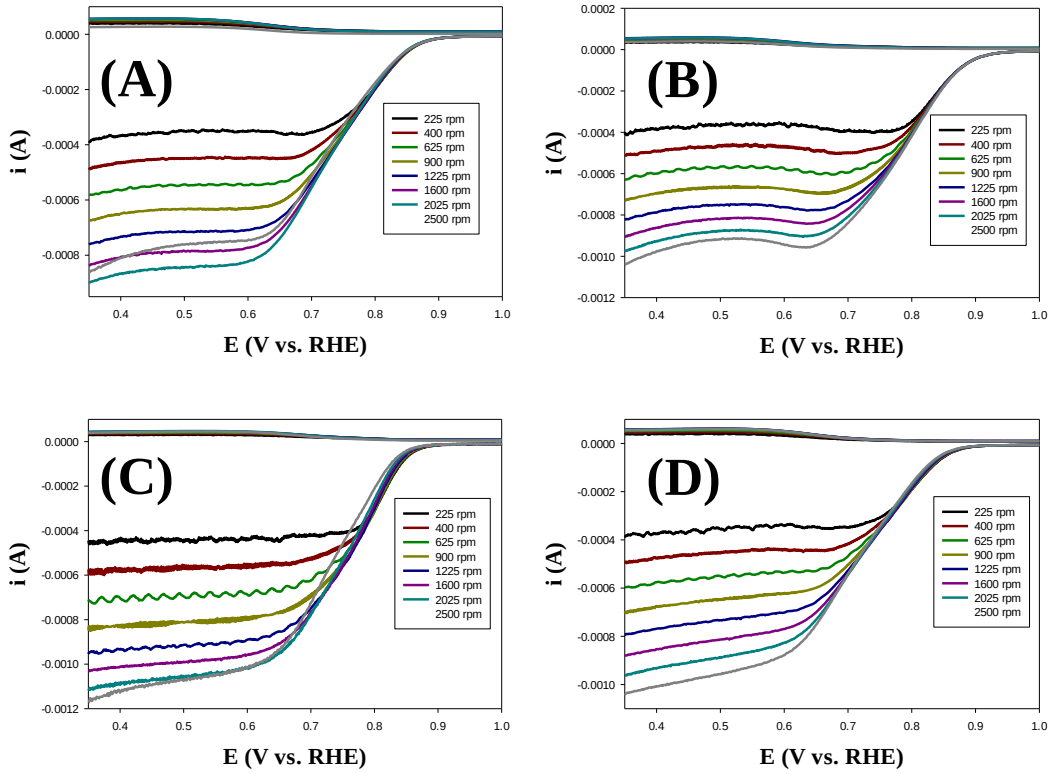

Figure 3.10 RRDE voltammagrams in O_2 saturated 0.1 M KOH at 10 mV/s a) Au/TiO_2 30 min b) Au/SiO_2 30 min e) Au/TiO_2 10 min f) Au/SiO_2 10 min

To determine the number of electrons transferred, the following Equation 3.1 was used:

$$n = \frac{4I_D}{I_D + \frac{I_R}{N}} \tag{3.1}$$

where I_D is the disk current, I_R is the ring current, and N is the collection efficiency at 0.41. The electrons transferred were plotted vs. disk potential in Figure 3.11 (A). The calculated electron transfer numbers are 3.8, 3.7, 3.7, and 3.6 for Au/TiO_2 30 min,

Au/TiO_2 10 min, Au/SiO_2 30 min, and Au/SiO_2 10 min respectively at their highest point a potential of 0.75 V vs. RHE. All numbers are very close to four so all samples perform the ORR mostly through the 4 electron pathway with Au/TiO_2 30 min being the closest to the 4 electron pathway.[61] These values confirm the differences in magnitude between the disk and ring currents for all the samples. Interestingly, the electrons transferred decreases as the potential becomes more negative for all the samples except Au/SiO_2 30 min sample. This behavior transpires from the RRDE voltammagrams showing crossing behavior and mass transfer effects. The kinetics of the reaction were further studied using Koutecky-Levich Analysis (Equation 3.2)

$$\frac{1}{i} = \frac{1}{i_K} + \frac{1}{i_D} \tag{3.2}$$

where i the measured current at 1600 rpm, i_K is the kinetic current, and i_D is the diffusion limited current approximated to the limiting current at 1600 rpm. The disk potential was plotted against the kinetic currents to form the Tafel Plot. From the Tafel Plot (Figure 3.11 (B)), a mass activity at 0.85 V vs. RHE is calculated to be 2.78 A/g, 9.31 A/g, 5.96 A/g, and 3.71 A/g for Au/TiO_2 10 min, Au/TiO_2 30 min, Au/SiO_2 10 min, and Au/SiO_2 30 min samples respectively with Au/TiO_2 30 min having the highest activity. From the Tafel Plots, the tafel slopes for the samples are -105, -100, -115, and -105 mV/dec for Au/TiO_2 10 min, Au/TiO_2 30 min, Au/SiO_2 10 min, and Au/SiO_2 30 min respectively. All of the Tafel slopes are close to the accepted value of -120 mV/dec which shows that the conversion of $O_2 + H^+/e^- + * \rightarrow OOH*$ is the rate-limiting step.[62] Combining all the results from the analysis it can be concluded that the Au/TiO_2 30

min sample has the highest electrocatalytic activity towards the oxygen reduction reaction.

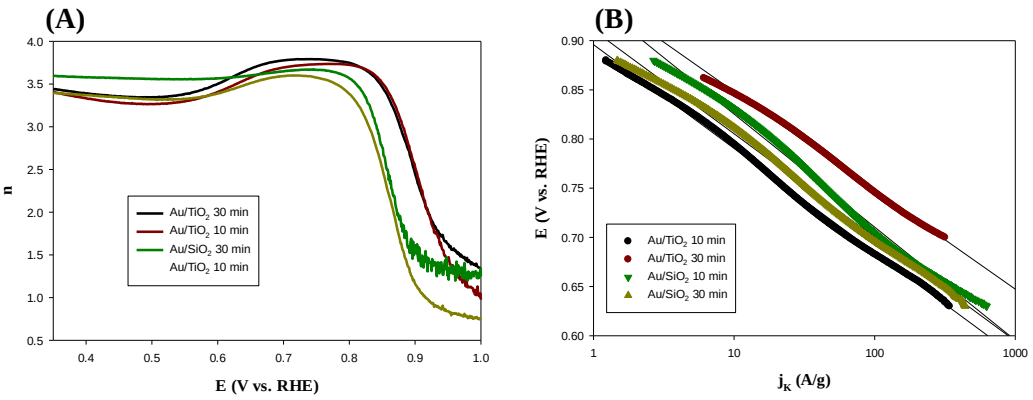

Figure 3.11 a) Electrons transferred plot b) Tafel plot. Inset: Specific activity @ 0.85 V vs. RHE of samples

The origin of the better activity for the TiO_2 samples stems from the presence of defects. A combination of Raman and XPS showed that Au/TiO_2 nanocomposites have strong interactions that creates the Ti^{3+} state which is the origin of ORR activity. It is interesting to note that the Au/SiO_2 composites do not show this defect state in both Raman and XPS data. Therefore, the surface remains unreduced and therefore, is not as reactive of a support as TiO_2. This is verified by the ORR data where the TiO_2 samples have a higher electrochemical surface area, onset potential, number of electrons transferred, and specific activity. Therefore, we have successfully demonstrated that the defects in oxides play a role in electrocatalysis.

3.4 Conclusions

The role of the support in electrocatalytic reactions is very important can affect the kinetics of these reactions. We have demonstrated here, that the results with TiO_2 as a support and SiO_2 as a support vary greatly because of the interaction that gold has with the different oxides because of their different reducibility capabilities. TiO_2 has two oxidation states, Ti^{4+} and Ti^{3+}, and the presence of these influences the activity. With an increasing amount of Ti^{3+}, the activity is enhanced as demonstrated here with Au/TiO_2 10 min being the best sample for oxygen reduction.

3.5 References

(1) Holton, O. T.; Stevenson, J. W.: The Role of Platinum in Proton Exchange Membrane Fuel Cells Evaluation of platinum's unique properties for use in both the anode and cathode of a proton exchange membrane fuel cell. *Platin Met Rev* **2013**, *57*, 259-271.

(2) Duan, Z. Y.; Henkelman, G.: CO Oxidation at the Au/TiO_2 Boundary: The Role of the Au/Ti-5c Site. *Acs Catal* **2015**, *5*, 1589-1595.

(3) Widmann, D.; Behm, R. J.: Activation of Molecular Oxygen and the Nature of the Active Oxygen Species for CO Oxidation on Oxide Supported Au Catalysts. *Accounts Chem Res* **2014**, *47*, 740-749.

(4) Fu, Q.; Li, W. X.; Yao, Y. X.; Liu, H. Y.; Su, H. Y.; Ma, D.; Gu, X. K.; Chen, L. M.; Wang, Z.; Zhang, H.; Wang, B.; Bao, X. H.: Interface-Confined Ferrous Centers for Catalytic Oxidation. *Science* **2010**, *328*, 1141-1144.

(5) Neophytides, S. G.; Zafeiratos, S.; Papakonstantinou, G. D.; Jaksic, J. M.; Paloukis, F. E.; Jaksic, M. M.: Extended Brewer hypo-hyper-d-interionic bonding theory II. Strong metal-support interaction grafting of composite electrocatalysts. *Int J Hydrogen Energy* **2005**, *30*, 393-410.

(6) Cheng, N. C.; Liu, J.; Banis, M. N.; Geng, D. S.; Li, R. Y.; Ye, S. Y.; Knights, S.; Sun, X. L.: High stability and activity of Pt electrocatalyst on atomic layer deposited metal oxide/nitrogen-doped graphene hybrid support. *Int J Hydrogen Energy* **2014**, *39*, 15967-15974.

(7) Sweeney, S. W.; Roseman, G.; Deming, C. P.; Wang, N.; Nguyen, T. A.; Millhauser, G. L.; Chen, S. W.: Impacts of oxygen vacancies on the electrocatalytic activity of $AuTiO_2$ nanocomposites towards oxygen reduction. *Int J Hydrogen Energy* **2016**, *41*, 18005-18014.

(8) Meier, J. C.; Galeano, C.; Katsounaros, I.; Witte, J.; Bongard, H. J.; Topalov, A. A.; Baldizzone, C.; Mezzavilla, S.; Schuth, F.; Mayrhofer, K. J. J.: Design criteria for stable Pt/C fuel cell catalysts. *Beilstein J Nanotech* **2014**, *5*, 44-67.

(9) Guczi, L.; Beck, A.; Paszti, Z.: Gold catalysis: Effect of particle size on reactivity towards various substrates. *Catal Today* **2012**, *181*, 26-32.

(10) Li, W. K.; Chu, L. N.; Gong, X. Q.; Lu, G. Z.: A comparative DFT study of adsorption and catalytic performance of Au nanoparticles at anatase and brookite TiO_2 surfaces. *Surf Sci* **2011**, *605*, 1369-1380.

(11) Liu, L. C.; Gu, X. R.; Cao, Y.; Yao, X. J.; Zhang, L.; Tang, C. J.; Gao, F.; Dong, L.: Crystal-Plane Effects on the Catalytic Properties of Au/TiO_2. *Acs Catal* **2013**, *3*, 2768-2775.

(12) Liu, J. Y.: Advanced Electron Microscopy of Metal-Support Interactions in Supported Metal Catalysts. *Chemcatchem* **2011**, *3*, 934-948.

(13) Lin, C.; Song, Y.; Cao, L. X.; Chen, S. W.: Oxygen Reduction Catalyzed by Au-TiO_2 Nanocomposites in Alkaline Media. *Acs Appl Mater Inter* **2013**, *5*, 13305-13311.

(14) Ji, Y.; Cho, Y. I.; Jeon, Y.; Lee, C.; Park, D. H.; Shul, Y. G.: Design of active Pt on TiO_2 based nanofibrous cathode for superior PEMFC performance and durability at high temperature. *Appl Catal B-Environ* **2017**, *204*, 421-429.

(15) Xu, F.; Wang, D. Q.; Sa, B. S.; Yu, Y.; Mu, S. C.: One-pot synthesis of Pt/CeO_2/C catalyst for improving the ORR activity and durability of PEMFC. *Int J Hydrogen Energy* **2017**, *42*, 13011-13019.

(16) Fang, J.; Li, J. G.; Zhang, B.; Yuan, X.; Asakura, H.; Tanaka, T.; Teramura, K.; Xie, J. P.; Yan, N.: The support effect on the size and catalytic activity of thiolated Au-25 nanoclusters as precatalysts. *Nanoscale* **2015**, *7*, 6325-6333.

(17) Lu, H. Q.; Zhao, B. B.; Pan, R. L.; Yao, J. F.; Qiu, J. H.; Luo, L.; Liu, Y. C.: Safe and facile hydrogenation of commercial Degussa P25 at room temperature with enhanced photocatalytic activity. *Rsc Adv* **2014**, *4*, 1128-1132.

(18) Pan, X. Y.; Xu, Y. J.: Fast and spontaneous reduction of gold ions over oxygen-vacancy-rich TiO_2: A novel strategy to design defect-based composite photocatalyst. *Appl Catal a-Gen* **2013**, *459*, 34-40.

(19) Pan, D. C.; Zhao, N. N.; Wang, Q.; Jiang, S. C.; Ji, X. L.; An, L. J.: Facile synthesis and characterization of luminescent TiO_2 nanocrystals. *Adv Mater* **2005**, *17*, 1991-+.

(20) Rao, K. S.; El-Hami, K.; Kodaki, T.; Matsushige, K.; Makino, K.: A novel method for synthesis of silica nanoparticles. *J Colloid Interf Sci* **2005**, *289*, 125-131.

(21) Qiu, L.; Wang, Y.; Pang, D. D.; Ouyang, F.; Zhang, C. L.; Cao, G.: Characterization and Catalytic Activity of Mn-Co/TiO_2 Catalysts for NO Oxidation to NO_2 at Low Temperature. *Catalysts* **2016**, *6*.

(22) Wu, J. M.; Shih, H. C.; Tseng, Y. K.; Hsu, C. L.; Tsay, C. Y.: Synthesizing and comparing the photocatalytic activities of single-crystalline TiO_2 rutile nanowires and mesoporous anatase paste. *J Electrochem Soc* **2007**, *154*, H157-H160.

(23) Yu, Y.; Wen, W.; Qian, X. Y.; Liu, J. B.; Wu, J. M.: UV and visible light photocatalytic activity of Au/TiO_2 nanoforests with Anatase/Rutile phase junctions and controlled Au locations. *Sci Rep-Uk* **2017**, *7*.

(24) Chang, C. C.; Wu, H. L.; Kuo, C. H.; Huang, M. H.: Hydrothermal Synthesis of Monodispersed Octahedral Gold Nanocrystals with Five Different Size

Ranges and Their Self-Assembled Structures. *Chem Mater* **2008**, *20*, 7570-7574.

(25) Mott, D.; Thuy, N. T. B.; Aoki, Y.; Maenosono, S.: Aqueous synthesis and characterization of Ag and Ag-Au nanoparticles: addressing challenges in size, monodispersity and structure. *Philos T R Soc A* **2010**, *368*, 4275-4292.

(26) Tzounis, L.; Contreras-Caceres, R.; Schellkopf, L.; Jehnichen, D.; Fischer, D.; Cai, C. Z.; Uhlmann, P.; Stamm, M.: Controlled growth of Ag nanoparticles decorated onto the surface of SiO_2 spheres: a nanohybrid system with combined SERS and catalytic properties. *Rsc Adv* **2014**, *4*, 17846-17855.

(27) Burton, A. W.; Ong, K.; Rea, T.; Chan, I. Y.: On the estimation of average crystallite size of zeolites from the Scherrer equation: A critical evaluation of its application to zeolites with one-dimensional pore systems. *Micropor Mesopor Mat* **2009**, *117*, 75-90.

(28) Kursun, C.; Gogebakan, M.: Characterization of nanostructured Mg-Cu-Ni powders prepared by mechanical alloying. *J Alloy Compd* **2015**, *619*, 138-144.

(29) Chen, M. S.; Goodman, D. W.: The structure of catalytically active gold on titania. *Science* **2004**, *306*, 252-255.

(30) Worz, A. S.; Heiz, U.; Cinquini, F.; Pacchioni, G.: Charging of Au atoms on TiO_2 thin films from CO vibrational spectroscopy and DFT calculations. *J Phys Chem B* **2005**, *109*, 18418-18426.

(31) Alessi, A.; Agnello, S.; Buscarino, G.; Gelardi, F. M.: Raman and IR investigation of silica nanoparticles structure. *J Non-Cryst Solids* **2013**, *362*, 20-24.

(32) Du, J. M.; Zhang, J. S.; Kang, D. J.: Controlled synthesis of anatase TiO_2 nano-octahedra and nanospheres: shape-dependent effects on the optical and electrochemical properties. *Crystengcomm* **2011**, *13*, 4270-4275.

(33) Shi, J. J.; Mahr, C.; Murshed, M. M.; Zielasek, V.; Rosenauer, A.; Gesing, T. M.; Baumer, M.; Wittstock, A.: A versatile sol-gel coating for mixed oxides on nanoporous gold and their application in the water gas shift reaction. *Catal Sci Technol* **2016**, *6*, 5311-5319.

(34) Dalai, S.; Pakrashi, S.; Kumar, R. S. S.; Chandrasekaran, N.; Mukherjee, A.: A comparative cytotoxicity study of TiO_2 nanoparticles under light and dark conditions at low exposure concentrations. *Toxicol Res-Uk* **2012**, *1*, 116-130.

(35) Kumar, S.; Verma, N. K.; Singla, M. L.: Size Dependent Reflective Properties of TiO_2 Nanoparticles and Reflectors Made Thereof. *Dig J Nanomater Bios* **2012**, *7*, 607-619.

(36) Jing, L. Q.; Sun, X. J.; Cai, W. M.; Xu, Z. L.; Du, Y. G.; Fu, H. G.: The preparation and characterization of nanoparticle TiO_2/Ti films and their photocatalytic activity. *J Phys Chem Solids* **2003**, *64*, 615-623.

(37) Lang, X. Y.; Qian, L. H.; Guan, P. F.; Zi, J.; Chen, M. W.: Localized surface plasmon resonance of nanoporous gold. *Appl Phys Lett* **2011**, *98*.

(38) Selvaggi, R.; Tarpani, L.; Santuari, A.; Giovagnoli, S.; Latterini, L.: Silica nanoparticles assisted photodegradation of acridine orange in aqueous suspensions. *Appl Catal B-Environ* **2015**, *168*, 363-369.

(39) Zhang, Z.; Tan, X.; Yu, T.; Jia, L. X.; Huang, X.: Time-dependent formation of oxygen vacancies in black TiO_2 nanotube arrays and the effect on photoelectrocatalytic and photoelectrochemical properties. *Int J Hydrogen Energ* **2016**, *41*, 11634-11643.

(40) Zhu, Q.; Peng, Y.; Lin, L.; Fan, C. M.; Gao, G. Q.; Wang, R. X.; Xu, A. W.: Stable blue TiO_{2-x} nanoparticles for efficient visible light photocatalysts. *J Mater Chem A* **2014**, *2*, 4429-4437.

(41) Bruckner, A.: In situ electron paramagnetic resonance: a unique tool for analyzing structure-reactivity relationships in heterogeneous catalysis. *Chem Soc Rev* **2010**, *39*, 4673-4684.

(42) He, W. W.; Liu, Y. T.; Wamer, W. G.; Yin, J. J.: Electron spin resonance spectroscopy for the study of nanomaterial-mediated generation of reactive oxygen species. *J Food Drug Anal* **2014**, *22*, 49-63.

(43) Liu, H. Y.; Yang, W.; Wang, M. X.; Xiao, L.; Liu, S. T.: Fabrication of lotus-like Au@TiO_2 nanocomposites with enhanced gas-sensing properties. *Sensor Actuat B-Chem* **2016**, *236*, 490-498.

(44) Levchuk, I.; Sillanpaa, M.; Guillard, C.; Gregori, D.; Chateau, D.; Parola, S.: TiO_2/SiO_2 porous composite thin films: Role of TiO_2 areal loading and

modification with gold nanospheres on the photocatalytic activity. *Appl Surf Sci* **2016**, *383*, 367-374.

(45) Li, X. Z.; Li, F. B.: Study of Au/Au^{3+}-TiO_2 photocatalysts toward visible photooxidation for water and wastewater treatment. *Environ Sci Technol* **2001**, *35*, 2381-2387.

(46) Fan, C. Y.; Chen, C.; Wang, J.; Fu, X. X.; Ren, Z. M.; Qian, G. D.; Wang, Z. Y.: Black Hydroxylated Titanium Dioxide Prepared via Ultrasonication with Enhanced Photocatalytic Activity. *Sci Rep-Uk* **2015**, *5*.

(47) Hashimoto, S.; Tanaka, A.: Alteration of Ti 2p XPS spectrum for titanium oxide by low-energy Ar ion bombardment. *Surf Interface Anal* **2002**, *34*, 262-265.

(48) Porsgaard, S.; Jiang, P.; Borondics, F.; Wendt, S.; Liu, Z.; Bluhm, H.; Besenbacher, F.; Salmeron, M.: Charge State of Gold Nanoparticles Supported on Titania under Oxygen Pressure. *Angew Chem Int Edit* **2011**, *50*, 2266-2269.

(49) Radnik, R.; Mohr, C.; Claus, P.: On the origin of binding energy shifts of core levels of supported gold nanoparticles and dependence of pretreatment and material synthesis. *Phys Chem Chem Phys* **2003**, *5*, 172-177.

(50) Su, Y. S.; Lee, M. Y.; Lin, S. D.: XPS and DRS of Au/TiO_2 catalysts: effect of pretreatment. *Catal Lett* **1999**, *57*, 49-53.

(51) Alam, A. U.; Howlader, M. M. R.; Deen, M. J.: Oxygen Plasma and Humidity Dependent Surface Analysis of Silicon, Silicon Dioxide and Glass for Direct Wafer Bonding. *Ecs J Solid State Sc* **2013**, *2*, P515-P523.

(52) Gross, T.; Ramm, M.; Sonntag, H.; Unger, W.; Weijers, H. M.; Adem, E. H.: An XPS Analysis of Different SiO_2 Modifications Employing a C 1s as Well as an Au 4f7/2 Static Charge Reference. *Surf Interface Anal* **1992**, *18*, 59-64.

(53) Zhao, X. F.; Han, P.; Scott, S.; Legally, M.: Influence of Surface and Interface Properties on the Electrical Conductivity of Silicon Nanomembranes. *Adv Mater Res-Switz* **2012**, *383-390*, 7220-+.

(54) Cherevko, S.; Topalov, A. A.; Zeradjanin, A. R.; Katsounaros, I.; Mayrhofer, K. J. J.: Gold dissolution: towards understanding of noble metal corrosion. *Rsc Adv* **2013**, *3*, 16516-16527.

(55) Mahesh, I.; Sarkar, A.: Electrochemical Study of Oxygen Reduction on a Carbon-Supported Core-Shell Platinum-Gold Electrocatalyst with Tuneable Gold Surface Composition. *Chemelectrochem* **2016**, *3*, 836-845.

(56) Trasatti, S.; Petrii, O. A.: Real Surface-Area Measurements in Electrochemistry. *J Electroanal Chem* **1992**, *327*, 353-376.

(57) Sheng, W. C.; Zhuang, Z. B.; Gao, M. R.; Zheng, J.; Chen, J. G. G.; Yan, Y. S.: Correlating hydrogen oxidation and evolution activity on platinum at different pH with measured hydrogen binding energy. *Nat Commun* **2015**, *6*.

(58) Norskov, J. K.; Rossmeisl, J.; Logadottir, A.; Lindqvist, L.; Kitchin, J. R.; Bligaard, T.; Jonsson, H.: Origin of the overpotential for oxygen reduction at a fuel-cell cathode. *J Phys Chem B* **2004**, *108*, 17886-17892.

(59) Meng, R.; Weber, S. G.: The rotating ring-disk electrochemistry of the copper(II) complex of thyrotropin-releasing hormone. *J Electroanal Chem* **2007**, *600*, 325-334.

(60) Hotchen, C. E.; Nguyen, H. V.; Fisher, A. C.; Frith, P. E.; Marken, F.: Hydrodynamic Microgap Voltammetry under Couette Flow Conditions: Electrochemistry at a Rotating Drum in Viscous Poly(ethylene glycol). *Chemphyschem* **2015**, *16*, 2789-2796.

(61) Zhang, L.; Li, H.; Zhang, J. J.: Kinetics of oxygen reduction reaction on three different Pt surfaces of Pt/C catalyst analyzed by rotating ring-disk electrode in acidic solution. *J Power Sources* **2014**, *255*, 242-250.

(62) Holewinski, A.; Linic, S.: Elementary Mechanisms in Electrocatalysis: Revisiting the ORR Tafel Slope. *J Electrochem Soc* **2012**, *159*, H864-H870.

Chapter 4

Understanding the Effects of Nitrogen Doping in TiO_2 as a Support for the Oxygen Reduction Reaction

Abstract

Fuel cells are an interesting electrical-based alternative. However, their commercialization is being hindered because of the sluggish kinetics of the cathode reaction, the oxygen reduction reaction (ORR). Currently, the commercial catalyst is Pt/C, but the low abundance of Pt and the degradation of the carbon cause this catalyst to be expensive and not that efficient. TiO_2 is looked at as a promising alternative, but the kinetics with this support are worse because of the low conductivity. Here, we doped the TiO_2 with nitrogen to increase conductivity and therefore enhance TiO_2's capability as a promising support for the ORR. We also attempted to control the change in nitrogen doping to see the effect on activity using hydrothermal heating with ascorbic acid. However, there was no trend to be found and the hydrothermal heating with ascorbic acid seemed to worsen the activity for the ORR.

4.1 Introduction

Nanocomposites based on metal nanoparticles supported on oxide surfaces have been used extensively as effective catalysts for a wide range of chemical reactions, including fuel cell electrochemistry. In fact, such functional hybrid materials have been

found to exhibit apparent electrocatalytic activity towards both oxidation of fuel molecules at the anode and reduction of oxygen at the cathode, with catalytic performances comparable, or even superior, to that of state-of-the art platinum catalysts [1-3]. This has been ascribed largely to the strong metal-support interactions [4-6]. For instance, Comotti and co-workers deposited gold nanoparticles on various metal oxides and found that the electrocatalytic activity towards CO oxidation varied with the oxide support, with $AuTiO_2$ identified as the best catalyst among the series [7]. In another study [8], Lin et al. prepared a series of $AuTiO_2$ nanocomposites and identified an optimal gold loading for maximal activity towards oxygen reduction reactions (ORR), which was accounted for by the dependence of surface OH concentration on gold contents. Similarly, Chen and co-workers deposited gold on SnO_2 nanoparticles, and observed that the gold loading played a vital role in the determination of the electrocatalytic activity towards ORR [9]. With an increasing gold loading, ORR evolved from the two-electron pathway to the four-electron one, and Tafel analysis showed that the optimal gold loading was ca. 1.9 at.% [9].

However, TiO_2 is a semiconductor and that causes a decrease in the activity for the ORR. Recently, nitrogen doped TiO_2 has become an interesting material to study especially in the realm of photocatalysis.[10] The nitrogen doping, causes N 2p orbitals to fall at an energy above the valence band decreasing the band gap, which in turn increases conductivity. The nitrogen doping can happen in two ways: substitutional doping and interstitial doping. Substitutional doping occurs when the nitrogen replaces an oxygen in the lattice, creating a Ti-N bond. In interstitial doping, the nitrogen will

sit between two oxygens, creating a Ti-O-N bond. However, there seems to be a lack in the literature in how the kinds of nitrogen doping affect the activity of the nitrogen-doped TiO_2.[11-13]

For the first time, in this study we employed the use of nitrogen-doped TiO_2 as a support for gold nanoparticles in the ORR. We first synthesized the N-TiO_2 nanoparticles using a sol-gel method. Then gold nanoparticles were deposited onto the N-TiO_2 nanoparticles and subject to hydrothermal heating with ascorbic acid to control the change in the different types of nitrogen doping. Finally, the ORR kinetics were tested using RRDE measurements and Koutecky-Levich analysis.

4.2 Materials and Methods

4.2.1 Chemicals

Ti-tert-butoxide (97%, Sigma-Aldrich), butyric acid (99+, ACROS Organics), urea (Fisher), hydrogen tetrachloroauric acid ($HAuCl_4$, Sigma-Aldrich), sodium borohydride (≥98%, Sigma-Aldrich) and ascorbic acid (99.0%, Sigma-Aldrich) were purchased from their sources in their highest purity. Solvents were purchased from typical commercial sources at their highest purity and used without further treatment. Water was supplied from a Barnstead Nanopure Water System (18.3 MΩ cm).

4.2.2 Synthesis of N-TiO_2 Nanoparticles

N-TiO_2 nanoparticles were synthesized using a literature sol-gel method.[14] First, 0.5021 g of ti-tert-butoxide was dissolved in 100 mL of acetic acid and stirred for

15 min. Then, 0.3968 g of butyric acid dissolved in 10 mL of Nanopure water and added to the solution and stirred for 2 h. Then 1 g of urea dissolved in 20 mL of Nanopure water and added to the solution and stirred for another 2 hr. Then, the pH was adjusted to 10 with 200 mL of ammonium hydroxide and stirred for 3 h at 60°C. The reaction was cooled down and the formed white precipitate was filtered off and dispersed in Nanopure water and heated to 60°C for 3 h. The white precipitate was filtered off, washed with ethanol, dried, and calcined in air at 400°C for 5 h. The as-formed nitrogen doped TiO_2 nanoparticles were used and labeled as N-TiO_2. TiO_2 nanoparticles were made using the same procedure except without the addition of the aqueous urea step and labeled as TiO_2.

4.2.3 Synthesis of Au/N-TiO_2 and Au/TiO_2 Nanocomposites

Gold nanoparticles were deposited onto the oxide materials using a wet chemical reduction method.[15,16] About 0.01 g of N-TiO_2 or TiO_2 was dispersed in 50 mL of THF. Then about 0.025 g of $HAuCl_4$ was added to the suspension. Then a cold aqueous solution of about 0.03 g of $NaBH_4$ dissolved in as little Nanopure water as possible was added dropped wise to the suspension which then proceeded to turn purple. The reaction stirred for 1 h at room temperature. Then, the purple precipitates were collected, washed with methanol, and vacuum dried to afford Au/N-TiO_2 and Au/TiO_2 nanocomposites.

4.2.4 Change in the Different Kinds of Nitrogen Doping

The Au/N-TiO_2 were further treated using a hydrothermal method to control the kinds of nitrogen doping.[15,17] About 0.1 g of Au/N-TiO_2 and 0.166 g of ascorbic acid were dissolved in Nanopure water and added to a Teflon-lined autoclave and reacted for 12 h at 140, 160, 180, and 200°C and were named as such. The black precipitates were collected, washed with water, and vacuum dried to afford Au/N-TiO_2 140, Au/N-TiO_2 160, Au/N-TiO_2 180, and Au/N-TiO_2 200.

4.2.5 Structural Characterization

The sample morphologies were examined with a transmission electron microscope (TEM, Philips CM300) operated at 300 kV. X-ray photoelectron spectroscopic (XPS) measurements were carried out with a PHI 5400/XPS instrument equipped with an Al K_α source operated at 350 W and 10^{-9} Torr. Diffuse reflectance UV-vis spectra were acquired with a Perkin-Elmer Lambda 35 spectrometer. X-ray diffraction (XRD) measurements were performed with a Rigaku Miniflex powder diffractometer using Cu K_α radiation with a Ni filter (λ = 0.154059 nm at 30 kV and 15 mA) that features a detection limit of 0.04. For EPR measurements, samples were prepared by filling quartz EPR tubes (Wilmad, 4 mm outer diameter) with one centimeter of powdered materials and centering the sample in the cavity resonator for data collection. Spectra were recorded at room temperature with a Bruker EMX EPR spectrometer operating at the X-band frequency (~9.4 GHz) using an ER 4122SHQE resonator (Bruker). All spectra were recorded at a power of 1 mW, a modulation amplitude of 1 G, and a modulation frequency of 100 KHz.

4.2.6 Electrochemistry

Electrochemical experiments were carried out with a CHI 710 Electrochemical Workstation with a glassy-carbon disk and gold ring electrode, a graphite rod counter electrode, and a Ag/AgCl reference electrode. A catalyst ink was prepared by adding 10 mg of the nanocomposites prepared above and 40 mg of carbon black dispersed in 500 mL of ethanol and 5 μL of Nafion (corresponding to a nanocomposite concentration of 20 wt.%). The ink was then dropcast onto the glassy carbon disk at a nanocomposite loading of ca. 20 mg, and dried in air before being immersed into electrolyte solutions for data acquisition.

4.3 Results and Discussion

4.3.1 Structural Characterization and Assignment

Morphologies of the nanocomposites were first examined using TEM, shown in Figure 4.1. In panel (A), a representative image of Au/N-TiO_2 is shown. In the image there seems to be dark contrast circles which are attributed to the gold nanoparticles and light contrast circles which are the TiO_2 nanoparticles. The gold nanoparticles are somewhat aggregated, but very dispersed on the TiO_2 nanoparticles which are heavily aggregated. Taking a closer look at the interface of the Au and TiO_2, panel (B) shows an HRTEM image of the Au/N-TiO_2 sample. The darker contrast spots are Au nanoparticles with lattice fringes of 0.239 nm, which are attributed to the Au(111) facet.[18] At the edge of the darker contrast spots, lattice fringes for anatase TiO_2 (200)

were found at 0.186 nm. When taking a closer look at the interface, the lattice fringes of the TiO_2 extend onto the gold nanoparticles, showing that they have good contact between the two.[19] In panel (C), the histogram of sizes for gold nanoparticles is shown. It is apparent that the distribution of gold is very large having an average diameter of 16.752 ± 7.088 nm. In panel (D), a representative TEM image of the Au/N-TiO_2 sample is shown. It seems that after hydrothermal heating with ascorbic acid, the particles become more dispersed showing even distribution of dark and light contrast spots. In panel (E), the HRTEM image of the interface of Au and TiO_2 is shown. After hydrothermal heating with ascorbic acid, the crystallinity of the interface decreases as shown by less well-defined lattice fringes. A 0.239 nm lattice is shown again for Au(111)[18] and 0.357 nm lattice is shown for anatase TiO_2 (101).[20] Finally in panel (F), the histogram for gold nanoparticle size distribution is shown. The diameter of the particles seems to have decreased with a more monodisperse size distribution with an average diameter of 8.305 ± 2.367 nm.

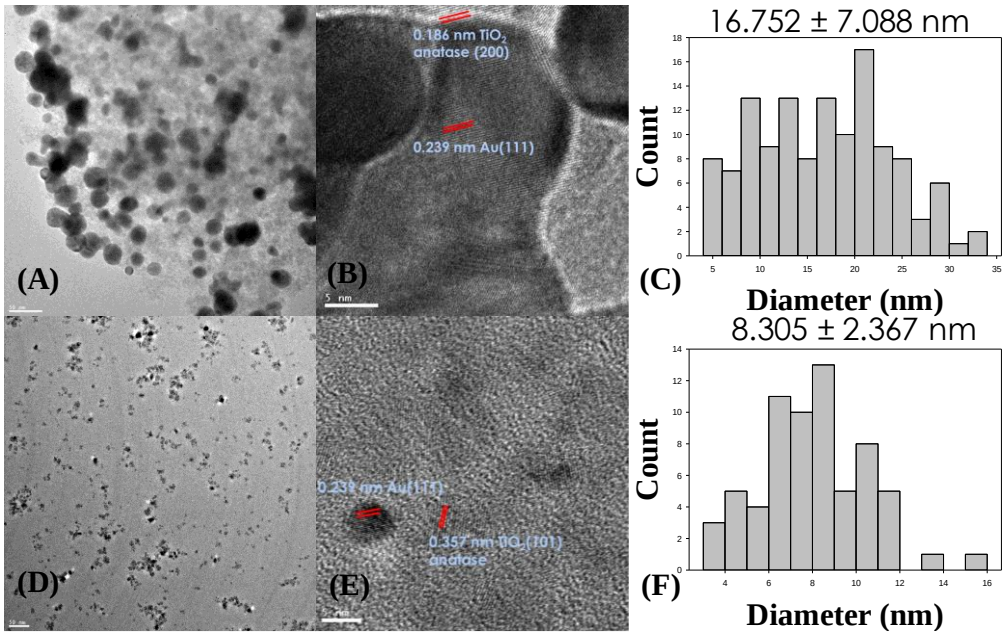

Figure 4.1 (A) Representative TEM image of Au/N-TiO_2 with a scale bar of 50 nm, **(B)** HRTEM image of interface of Au/N-TiO_2 with a scale bar of 5 nm, **(C)** Histogram of gold nanoparticle size on N-TiO_2, **(D)** Representative TEM image of Au/N-TiO_2 180 with a scale bar of 50 nm, **(E)** HRTEM image of interface of Au/N-TiO_2 180 with a scale bar of 5 nm, **(F)** Histogram of gold nanoparticle size on N-TiO_2 180

Structural characterization was further manifested in XRD measurements which are shown in Figure 4.2 of (A) N-TiO_2, (B) TiO_2, (C) Au/N-TiO_2, (D) Au/TiO_2, (E) Au/N-TiO_2 140, (F) Au/N-TiO_2 160, (G) Au/N-TiO_2 180, and (H) Au/N-TiO_2 200 respectively. N-TiO_2 and TiO_2 show peaks at 24.2°, 38.4°, 48.3°, 55.0°, and 63.7° corresponding to the anatase (101), (004), (200), (211), and (204) planes respectively (JCPDS no. 21-1272).[21] The N-TiO_2 sample's peaks are very broad and almost indistinguishable. This means that the nitrogen doping causes a decrease in crystallinity

of the TiO_2.[22] One gold is deposited onto the oxides, peaks appear at 38.1°, 44.4°, 64.4°, 77.5°, and 81.5° corresponding to the Au (111), (200), (220), (311), and (222) planes respectively (JCPDS no. 4-784).[23] The TiO_2 seem to disappear because of the apparent higher crystallinity of the gold and due to the hydrothermal heating in ascorbic acid. This confirms the TEM data. Another observation is with the change in temperature, the peaks do not change position and no new peaks appear which means the heating and the ascorbic acid don't affect the overall crystal structure of the Au/N-TiO_2 nanocomposites.

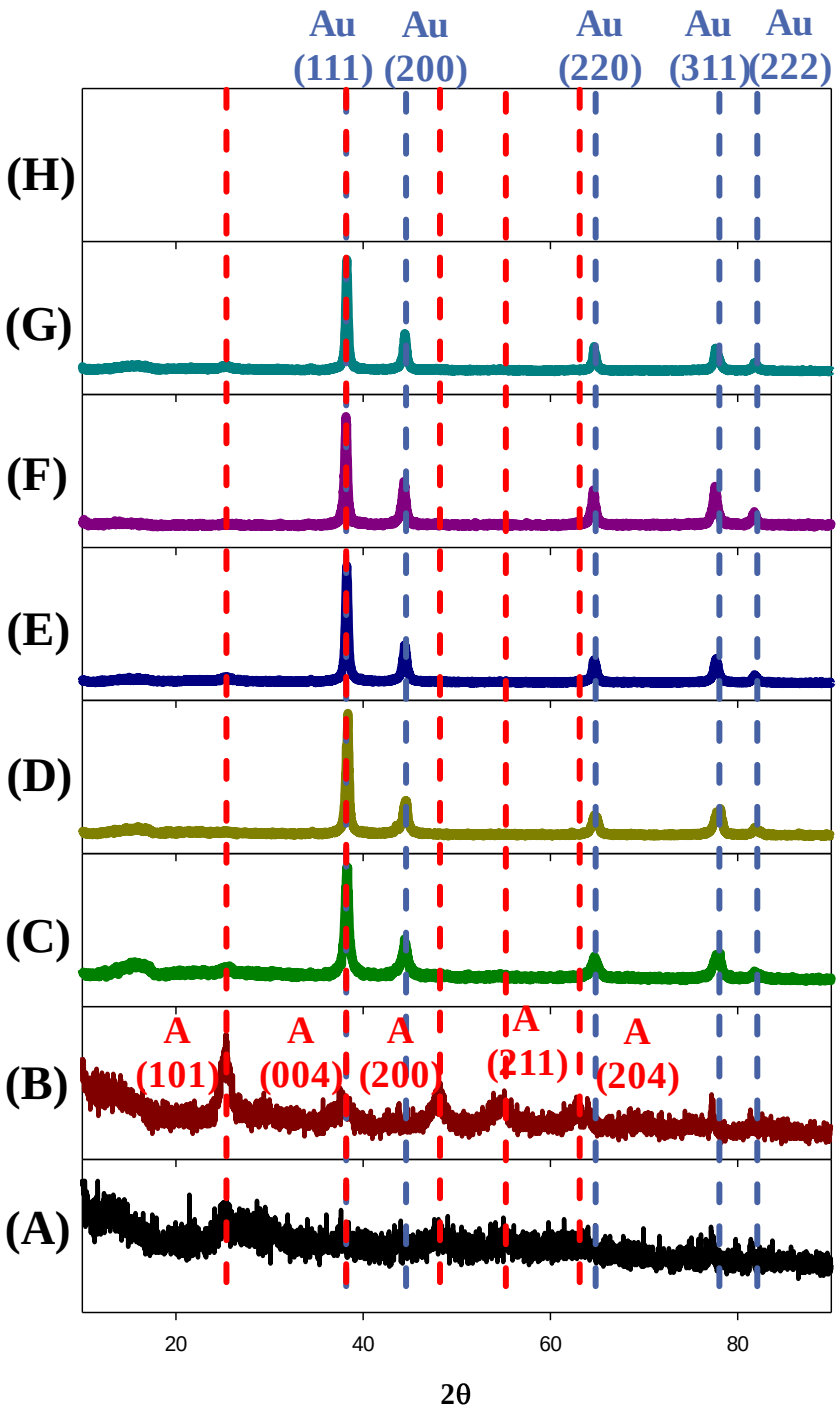

Figure 4.2 XRD spectra of **(A)** N-TiO_2, **(B)** TiO_2, **(C)** Au/N-TiO_2, **(D)** Au/TiO_2, **(E)** Au/N-TiO_2 140, **(F)** Au/N-TiO_2 160, **(G)** Au/N-TiO_2 180, and **(H)** Au/N-TiO_2 200

4.3.2 Optical and Electronic Characterization and Assignment

In Figure 4.3, diffuse reflectance UV-Vis spectra of all samples are shown to look at optical properties. Both N-TiO_2 and TiO_2 nanoparticles show an exponential decay profile. This means that the defects in both samples cause some absorption in the visible range.[24] Once gold is deposited onto the oxide substrates, there is complete absorption in the visible range and a peak appears at 530 nm which is due to the localized surface plasmon resonance (LSPR) of gold.[25-27] The temperature and the ascorbic acid treatment cause the LSPR to disappear.

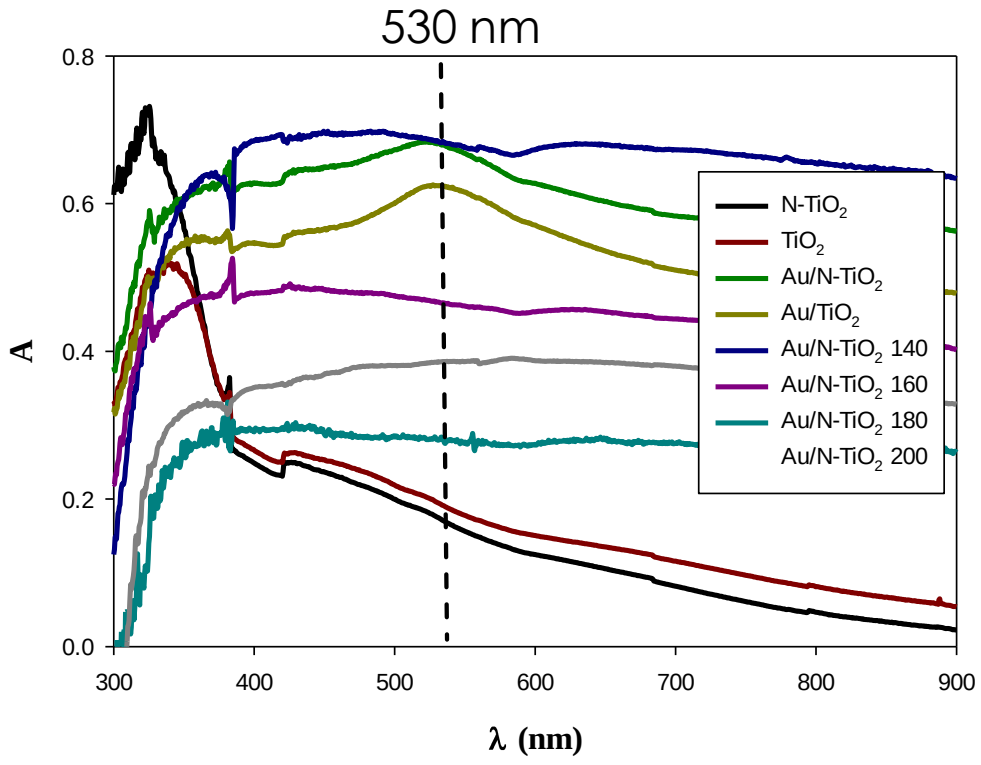

Figure 4.3 Diffuse reflectance UV-Vis spectra of all samples.

Electronic characterization was further manifested in high resolution Au 4f XPS, which is shown in Figure 4.4. All of the samples have at least one pair of peaks at 87.58 and 83.93 eV for Au/N-TiO_2, 87.79 and 84.15 eV for Au/N-TiO_2 140, 87.70 and 84.04 eV for Au/N-TiO_2 160, 87.61 and 83.97 eV for Au/N-TiO_2 180, and 87.72 and 84.09 eV Au/N-TiO_2 200. In contrast, the Au/TiO_2 samples has two pairs of peaks at 88.22 and 83.45 eV and 86.26 and 82.56 eV. All of the ascorbic acid-treated samples have a slightly higher Au 4f binding energy that the Au/N-TiO_2 treated sample. This means that after ascorbic acid treatment the gold becomes more oxidized overall.[28] As the temperature increases for hydrothermal heating, the Au 4f binding energy decreases then increases slightly. This means that the gold is slightly more reducing as the temperature increases to 180 and then beyond that it becomes more oxidizing.[28] For the Au/TiO_2 sample, the higher binding energy pair of peaks seems to be much more oxidized and the lower binding energy pair of peaks seems to be much more reduced.

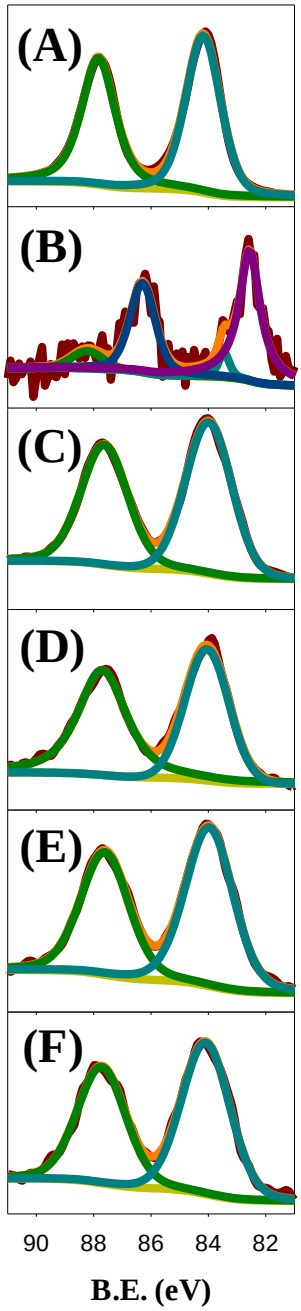

Figure 4.4 High resolution Au 4f XPS spectra of Au/TiO_2 nanocomposites **(A)** Au/N-TiO_2, **(B)** Au/TiO_2, **(C)** Au/N-TiO_2 140, **(D)** Au/N-TiO_2 160, **(E)** Au/N-TiO_2 180, and **(F)** Au/N-TiO_2 200

Characterization of the nitrogen doping was further studied by taking a closer look at high resolution N 1s spectra as shown in Figure 4.5. All of the samples except Au/N-TiO_2 180 have 1 peak at 400.18 eV for N-TiO_2, 399.15 eV for Au/N-TiO_2, 400.81 eV for Au/N-TiO_2 140, 400.08 eV for Au/N-TiO_2 160, and 400 eV for Au/N-TiO_2 200. Au/N-TiO_2 180 has two peaks at 400.09 eV and 397.68 eV. The peak at ~397 eV is ascribed to the substitutional nitrogen doping and the Ti-N bond. The peak at ~399-400 eV is ascribed to the interstitial nitrogen doping or the Ti-O-N bond.[29] It seems that the deposition of gold does not affect the nitrogen doping type and the only temperature that seemed to affect the type of nitrogen doping is 180°C.

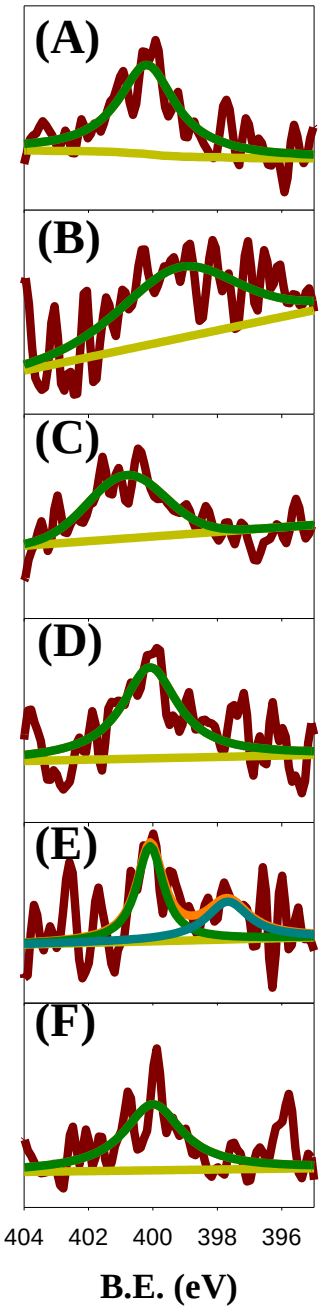

Figure 4.5 High resolution XPS N 1s of nitrogen-doped samples **(A)** N-TiO_2, **(B)** Au/N-TiO_2, **(C)** Au/N-TiO_2 140, **(D)** Au/N-TiO_2 160, **(E)** Au/N-TiO_2 180, and **(F)** Au/N-TiO_2 200.

Finally, electronic characterization was finished by looking at high resolution O 1s and Ti 2p spectra shown in Figure 4.6. Before hydrothermal heating, the O 1s spectra shows two peaks at 532.02 and 530.14 eV for N-TiO_2, 532.65 and 530.79 eV for TiO_2, 532.11 and 530.56 eV for Au/N-TiO_2, and 533.06 and 530.79 eV for Au/TiO_2. The peak at ~532-533 eV is labeled as the peak for surface -OH groups bound to the TiO_2 and the peak ~530 eV is for the O_2^{2-} in the lattice of TiO_2.[28] The ratio of the intensities of these two peaks are 0.317, 0.477, 0.350, and 2.22 for N-TiO_2, TiO_2, for Au/N-TiO_2, and Au/TiO_2 respectively. The first thing to notice is when gold is deposited on either TiO_2, the hydroxide concentration increases which could be due to the strong-metal-support interaction between gold and TiO_2.[30] It also seems there are more surface hydroxides when there is no nitrogen doping which does not make sense because nitrogen doping helps break down organic molecules in photocatalysis.[10] After hydrothermal heating in ascorbic acid, all the samples now have three peaks at 533.18, 531.48, and 530.03 eV for Au/N-TiO_2 140; 533.19, 531.69, and 530.11 eV Au/N-TiO_2 160; 533.22, 531.62, and 529.95 eV for Au/N-TiO_2 180; and 533, 531.38, and 529.78 eV for Au/N-TiO_2 200. The highest binding energy and third peak formed is due to water trapped in the lattice which comes from the hydrothermal heating.[28] The ratio of -OH groups to O_2^{2-} for these samples are 0.944, 0.732, 1.02, 0.740 for 140, 160, 180, and 200 respectively. There seems to be no trend with these samples.

Next the right column, of the Ti 2p peaks are shown with all samples except Au/N-TiO_2 180 having 1 pair of peaks and that sample having 2 pairs of peaks. The

peaks are located at 464.42 and 458.73 eV for N-TiO_2, 465.02 and 459.22 eV for TiO_2, 464.92 and 459.19 eV for Au/N-TiO_2, 465.04 eV and 459.21 eV for Au/TiO_2, 464.57 and 458.86 eV for Au/N-TiO_2 140, 464.51 and 458.84 eV for Au/N-TiO_2 160, and 464.36 and 458.7 for Au/N-TiO_2 200. Au/N-TiO_2 180's peaks are at 465.04, 459.2, 463.9, and 458.44 eV. It seems that Au/N-TiO_2 180 is the only sample with a Ti^{3+} signal.[28] Un-doped TiO_2 samples have more oxidized TiO_2 which relates to the one set of peaks of Au 4f that are more reduced. Once gold is deposited on the N-TiO_2, the Ti becomes more oxidized, which means the Ti is transferring charge to the Au. After hydrothermal heating in ascorbic acid, there seems to be no trend between the temperature and the Ti signal. Next the ratio of N:Ti was calculated to be 0.0404, 0.153, 0.124, 0.103, 0.133, and 0.136 for N-TiO_2, Au/N-TiO_2, Au/N-TiO_2 140, Au/N-TiO_2 160, Au/N-TiO_2 180, and Au/N-TiO_2 200 respectively. The only substantial difference between any of the ratios is between the N-TiO_2 and Au/N-TiO_2 samples which means the gold signal affected the nitrogen signal. After hydrothermal heating the N content doesn't change based on XPS so the temperature does not affect the amount of nitrogen doping. Finally, Au:Ti ratio was calculated to be 0.763, 0.1, 0.373, 0.147, 0.361, and 0.125 for Au/N-TiO_2, Au/TiO_2, Au/N-TiO_2 140, Au/N-TiO_2 160, Au/N-TiO_2 180, and Au/N-TiO_2 200 respectively. Because of the large contrast in gold content, the ORR could be affected.

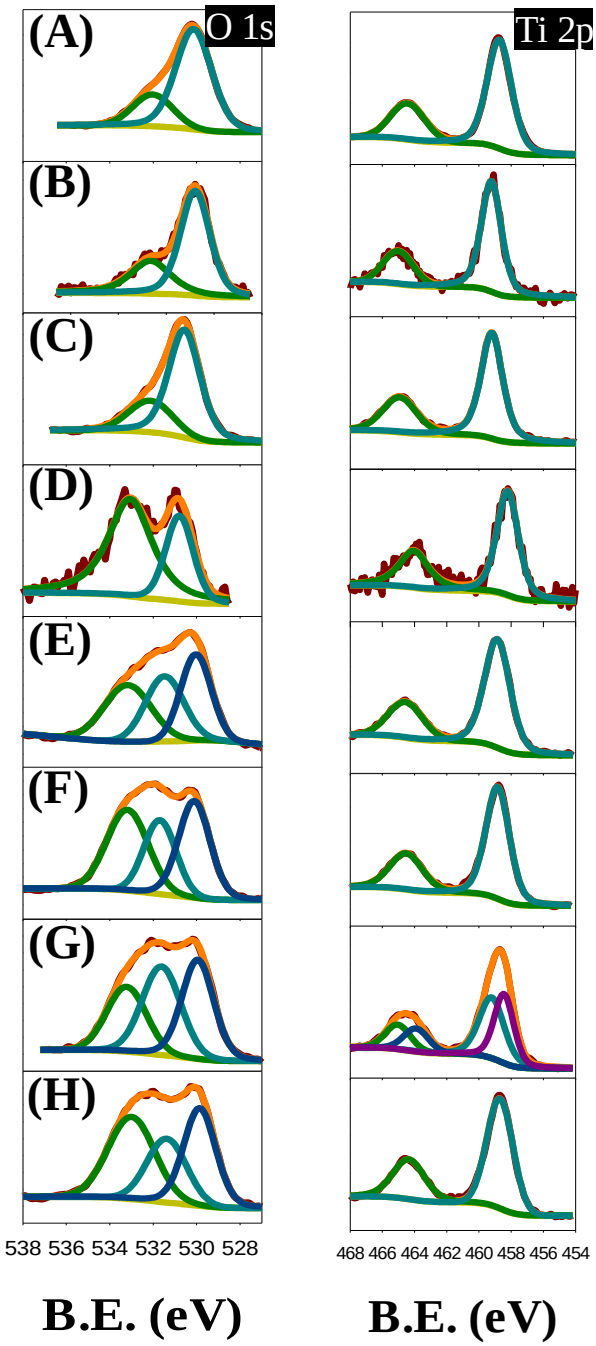

Figure 4.6 High resolution O1s and Ti 2p XPS of all samples **(A)** N-TiO_2, **(B)** TiO_2, **(C)** Au/N-TiO_2, **(D)** Au/TiO_2, **(E)** Au/N-TiO_2 140, **(F)** Au/N-TiO_2 160, **(G)** Au/N-TiO_2 180, and **(H)** Au/N-TiO_2 200

4.3.3 Electrocatalytic Activity for the ORR

In Figure 4.7, electrocatalytic activity is shown. Panel (A) shows cyclic voltammograms of Au/TiO_2 nanocomposites in N_2 saturated 0.1 M KOH at a scan rate of 10 mV/s. For all he samples in the cathodic scan, there appears to be 2 peaks at around 1.2 V vs. RHE and 0.8 V vs. RHE. The first peak's position is at 1.215, 1.145, 1.211, 1.207, 1.137, and 1.140 V vs. RHE for $Au/N\text{-}TiO_2$, Au/TiO_2, $Au/N\text{-}TiO_2$ 140, $Au/N\text{-}TiO_2$ 160, $Au/N\text{-}TiO_2$ 180, and $Au/N\text{-}TiO_2$ 200 respectively. This peak is due to the reduction of the AuO monolayer that is formed, shown by the oxidation peak in the anodic scan at 1.3 V vs. RHE. All of the nitrogen doped samples have a more positive AuO peak than the Au/TiO_2. After hydrothermal heating, as the temperature increases, the peak position decreases overall. This implies that as the temperature increases, the reduction of AuO becomes harder. From the AuO reduction peak, an electrochemical surface area can be calculated dividing the charge by the charge density of 390 $\mu C/cm^2$.[31] The electrochemical surface area is 0.0873, 0.271, 0.142, 0.0851, 0.122, and 0.0812 cm^2 for $Au/N\text{-}TiO_2$, Au/TiO_2, $Au/N\text{-}TiO_2$ 140, $Au/N\text{-}TiO_2$ 160, $Au/N\text{-}TiO_2$ 180, and $Au/N\text{-}TiO_2$ 200 respectively. The second peak position is 0.872, 0.852, 0.883, 0.872, 0.814, and 0.802 V vs. RHE $Au/N\text{-}TiO_2$, Au/TiO_2, $Au/N\text{-}TiO_2$ 140, $Au/N\text{-}TiO_2$ 160, $Au/N\text{-}TiO_2$ 180, and $Au/N\text{-}TiO_2$ 200 respectively. This peak is due to a second AuO species.

In panel (B), rotating-ring-disk voltammograms normalized to geometric surface area of the electrode (0.247 cm^2) of the Au/TiO_2 samples are shown. The disk

current seems to be 4x higher than the ring current, suggesting that the samples mainly don't form the peroxide intermediate.[32] From the voltammogram, the onset potential was determined to be 0.98, 0.97, 0.95, 0.95, 0.92, and 0.9 V vs. RHE for Au/N-TiO_2, Au/TiO_2, Au/N-TiO_2 140, Au/N-TiO_2 160, Au/N-TiO_2 180, and Au/N-TiO_2 200 respectively. The half-wave potential can also be determined from the graph. It is 0.85, 0.84, 0.85, 0.84, 0.78, and 0.75 V vs. RHE for Au/N-TiO_2, Au/TiO_2, Au/N-TiO_2 140, Au/N-TiO_2 160, Au/N-TiO_2 180, and Au/N-TiO_2 200 respectively. The sample with the highest onset potential and half-wave potential is Au/N-TiO_2.

In panel (C), the electrons transferred vs. disk potential is plotted from the data from panel (B). The electrons transferred are calculated from Equation 4.1:

$$n = \frac{4I_D}{I_D + \frac{I_R}{N}} \tag{4.1}$$

where n is the electrons transferred, I_D is the disk current, I_R is the ring current, and N is the collection efficiency of the electrode (calculated to be 0.41 from RRDE measurements in potassium ferrocyanide).[33,34] From this equation, the electrons transferred were calculated to be 3.5, 3.7, 3.2, 3.3, 3.5, and 3.7 electrons for Au/N-TiO_2, Au/TiO_2, Au/N-TiO_2 140, Au/N-TiO_2 160, Au/N-TiO_2 180, and Au/N-TiO_2 200 respectively. All of the samples seem to follow the 4-electron pathway for oxygen reduction mostly with with Au/TiO_2 and Au/N-TiO_2 having the closest numbers to 4.[34]

Finally, from Koutecky-Levich analysis[34] in panel (D), a Tafel Plot was created. At 0.90 V vs. RHE, the mass activity was determined to be 3.76, 2.74, 2.7, 2.7, and 1.83 A/g for Au/N-TiO_2, Au/TiO_2, Au/N-TiO_2 140, Au/N-TiO_2 160, and Au/N-TiO_2 180 respectively. All of these numbers were plotted in a bar graph which is shown in the inset of panel (D). From these graphs, the Au/N-TiO_2 sample was determined to have the highest kinetic current for the ORR. From this graph, the Tafel Slope was also calculated to be -160, -125, -110, -118, -166, and -168 mV/dec. Since all of these numbers are close to the value of -120 mV/dec, each sample showed the that the rate determining step for this reaction was the first electron transfer step.[35]

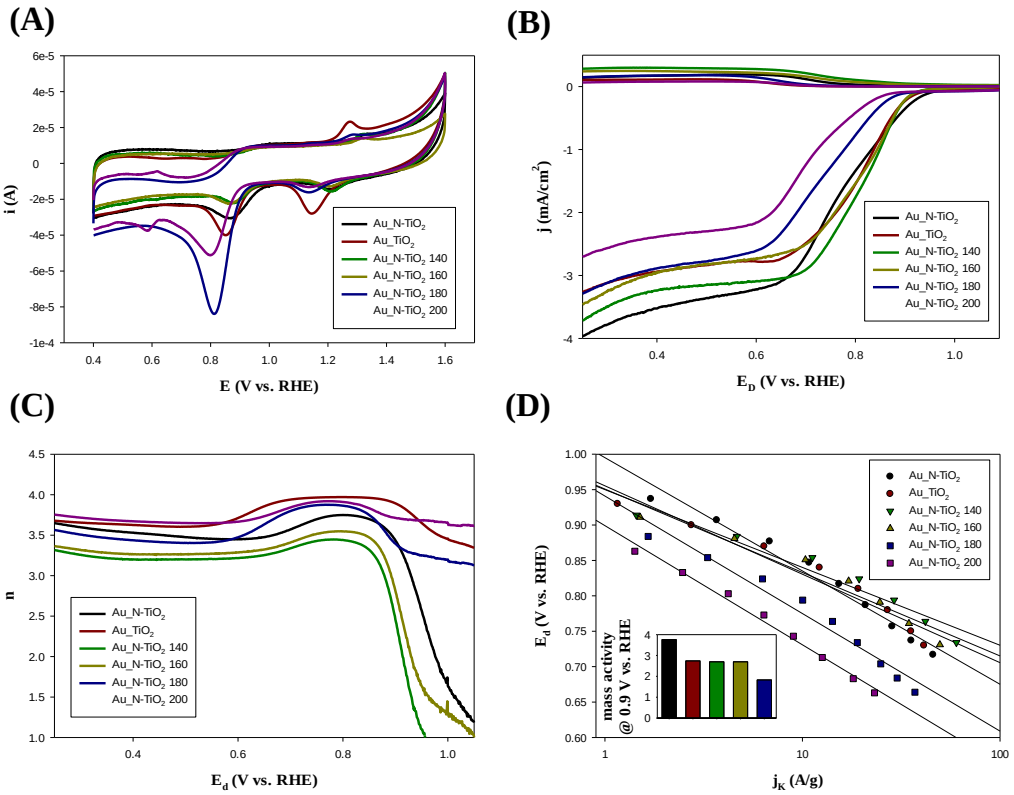

Fig 4.7 – **(A)** Cyclic voltammagrams of Au/TiO_2 nanocomposites in N_2 saturated 0.1 M KOH at a scan rate of 10 mV/s. **(B)** Rotating-ring-disk voltammgrams normalized to geometric surface area of the electrode (0.247 cm^2) of Au/TiO_2 nanocomposites in O_2 saturated 0.1 M KOH at a scan rate of 10 mV/s, rotation rate of 1600 rpm, and catalyst loading of 20 µg. **(C)** Variation of the number of electron transfer (n) with disk electrode potential. Data were obtained from the voltammograms in panel **(B)**. **(D)** Tafel plots of the Au/TiO_2 nanocomposite catalysts.

From all of these measurements it seems that the best sample for the ORR is $Au/N\text{-}TiO_2$. Overall, nitrogen doping seems to have some effect on the ORR kinetics. However, the XPS data not having a strong correlation shows that we cannot provide good evidence for this claim. Also, it seems that the activity decreased after hydrothermal heating. This is probably due to the decrease in the gold content which is shown by XPS. Our group has shown this before that having too low of a gold loading will affect the ORR kinetics.[17]

4.4 Conclusions

From this study it can be see that nitrogen doping has an effect on the properties of TiO_2. XPS measurements showed that there was some electron transfer, but not a good enough trend to show the trend in ORR activity.

4.5 References

(1) Wang, Y. G.; Yoon, Y.; Glezakou, V. A.; Li, J.; Rousseau, R.: The role of reducible oxide-metal cluster charge transfer in catalytic processes: new insights on the catalytic mechanism of CO oxidation on Au/TiO_2 from ab initio molecular dynamics. *Journal of the American Chemical Society* **2013**, *135*, 10673-83.

(2) Liu, X.; Liu, M. H.; Luo, Y. C.; Mou, C. Y.; Lin, S. D.; Cheng, H.; Chen, J. M.; Lee, J. F.; Lin, T. S.: Strong metal-support interactions between gold nanoparticles and ZnO nanorods in CO oxidation. *Journal of the American Chemical Society* **2012**, *134*, 10251-8.

(3) Jaksic, M. M.; Botton, G. A.; Papakonstantinou, G. D.; Nan, F. H.; Jaksic, J. M.: Primary Oxide Latent Storage and Spillover Enabling Electrocatalysts with Reversible Oxygen Electrode Properties and the Alterpolar Revertible (PEMFC versus WE) Cell. *Journal of Physical Chemistry C* **2014**, *118*, 8723-8746.

(4) Duan, Z. Y.; Henkelman, G.: CO Oxidation at the Au/TiO_2 Boundary: The Role of the Au/Ti-5c Site. *Acs Catal* **2015**, *5*, 1589-1595.

(5) Widmann, D.; Behm, R. J.: Activation of molecular oxygen and the nature of the active oxygen species for CO oxidation on oxide supported Au catalysts. *Accounts of chemical research* **2014**, *47*, 740-9.

(6) Fu, Q.; Li, W. X.; Yao, Y. X.; Liu, H. Y.; Su, H. Y.; Ma, D.; Gu, X. K.; Chen, L. M.; Wang, Z.; Zhang, H.; Wang, B.; Bao, X. H.: Interface-Confined Ferrous Centers for Catalytic Oxidation. *Science* **2010**, *328*, 1141-1144.

(7) Comotti, M.; Li, W. C.; Spliethoff, B.; Schuth, F.: Support effect in high activity gold catalysts for CO oxidation. *Journal of the American Chemical Society* **2006**, *128*, 917-924.

(8) Lin, C.; Song, Y.; Cao, L.; Chen, S.: Oxygen reduction catalyzed by Au-TiO_2 nanocomposites in alkaline media. *ACS applied materials & interfaces* **2013**, *5*, 13305-11.

(9) Chen, W.; Ny, D.; Chen, S.: SnO_2–Au hybrid nanoparticles as effective catalysts for oxygen electroreduction in alkaline media. *Journal of Power Sources* **2010**, *195*, 412-418.

(10) Wang, W.; Tade, M. O.; Shao, Z. P.: Nitrogen-doped simple and complex oxides for photocatalysis: A review. *Prog Mater Sci* **2018**, *92*, 33-63.

(11) Lynch, J.; Giannini, C.; Cooper, J. K.; Loiudice, A.; Sharp, I. D.; Buonsanti, R.: Substitutional or Interstitial Site-Selective Nitrogen Doping in TiO_2 Nanostructures. *J Phys Chem C* **2015**, *119*, 7443-7452.

(12) Reddy, P. A. K.; Reddy, P. V. L.; Kim, K. H.; Kumar, M. K.; Manvitha, C.; Shim, J. J.: Novel approach for the synthesis of nitrogen-doped titania with variable phase composition and enhanced production of hydrogen under solar irradiation. *J Ind Eng Chem* **2017**, *53*, 253-260.

(13) Asahi, R.; Morikawa, T.: Nitrogen complex species and its chemical nature in TiO_2 for visible-light sensitized photocatalysis. *Chem Phys* **2007**, *339*, 57-63.

(14) Barkul, R. P.; Koli, V. B.; Shewale, V. B.; Patil, M. K.; Delekar, S. D.: Visible active nanocrystalline N-doped anatase TiO_2 particles for photocatalytic mineralization studies. *Mater Chem Phys* **2016**, *173*, 42-51.

(15) Sweeney, S. W.; Roseman, G.; Deming, C. P.; Wang, N.; Nguyen, T. A.; Millhauser, G. L.; Chen, S. W.: Impacts of oxygen vacancies on the electrocatalytic activity of $AuTiO_2$ nanocomposites towards oxygen reduction. *Int J Hydrogen Energ* **2016**, *41*, 18005-18014.

(16) Liu, K.; Song, Y.; Chen, S. W.: Defective TiO_2-supported Cu nanoparticles as efficient and stable electrocatalysts for oxygen reduction in alkaline media. *Nanoscale* **2015**, *7*, 1224-1232.

(17) Lin, C.; Song, Y.; Cao, L. X.; Chen, S. W.: Oxygen Reduction Catalyzed by Au-TiO_2 Nanocomposites in Alkaline Media. *Acs Appl Mater Inter* **2013**, *5*, 13305-13311.

(18) Lyu, S. B.; Lei, D. Y.; Liu, W. Q.; Yao, H. J.; Mo, D.; Chen, Y. H.; Hu, P. P.; Sun, Y. M.; Liu, J.; Duan, J. L.: Cyanide-free preparation of gold nanowires: controlled crystallinity, crystallographic orientation and enhanced field emission. *Rsc Adv* **2015**, *5*, 32103-32109.

(19) Liu, E. Z.; Xue, P.; Jia, J.; Zhang, X. Z.; Ji, Z.; Fan, J.; Hu, X. Y.: CdSe modified TiO_2 nanotube arrays with Ag nanoparticles as electron transfer channel and plasmonic photosensitizer for enhanced photoelectrochemical water splitting. *J Phys D Appl Phys* **2018**, *51*.

(20) Sutradhar, N.; Biswas, A.; Pahari, S. K.; Ganguly, B.; Panda, A. B.: Fluoride free synthesis of anatase TiO_2 nanocrystals with exposed active {001} facets. *Chem Commun* **2014**, *50*, 11529-11532.

(21) Sridhar, S.; Arunnellaiappan, T.; Rameshbabu, N.; Mika, S.; Viswanathan, A.: Solar photocatalytic activity of nitrogen doped TiO_2 coating by micro-arc oxidation. *Surf Eng* **2017**, *33*, 779-786.

(22) Cheng, X. W.; Yu, X. J.; Xing, Z. P.; Yang, L. S.: Synthesis and characterization of N-doped TiO_2 and its enhanced visible-light photocatalytic activity. *Arab J Chem* **2016**, *9*, S1706-S1711.

(23) Kang, J. X.; Zhang, D. F.; Guo, G. C.; Yu, H. J.; Wang, L. H.; Huang, W. F.; Wang, R. Z.; Guo, L.; Han, X. D.: Au Catalyzed Carbon Diffusion in Ni: A Case of Lattice Compatibility Stabilized Metastable Intermediates. *Adv Funct Mater* **2018**, *28*.

(24) Smirniotis, P. G.; Boningari, T.; Inturi, S. N. R.: Single-step synthesis of N-doped TiO_2 by flame aerosol method and the effect of synthesis parameters. *Aerosol Sci Tech* **2018**, *52*, 913-922.

(25) Urrutia, A.; Goicoechea, J.; Rivero, P. J.; Pildain, A.; Arregui, F. J.: Optical fiber sensors based on gold nanorods embedded in polymeric thin films. *Sensor Actuat B-Chem* **2018**, *255*, 2105-2112.

(26) Zhang, J.; Feng, Y. H.; Mi, J. L.; Shen, Y. T.; Tu, Z. G.; Liu, L.: Photothermal lysis of pathogenic bacteria by platinum nanodots decorated gold nanorods under near infrared irradiation. *J Hazard Mater* **2018**, *342*, 121-130.

(27) Chandrasekhar, P. S.; Parashar, P. K.; Swami, S. K.; Dutta, V.; Komarala, V. K.: Enhancement of Y123 dye-sensitized solar cell performance using plasmonic gold nanorods. *Phys Chem Chem Phys* **2018**, *20*, 9651-9658.

(28) Kruse, N.; Chenakin, S.: XPS characterization of Au/TiO_2 catalysts: Binding energy assessment and irradiation effects. *Appl Catal a-Gen* **2011**, *391*, 367-376.

(29) Boningari, T.; Inturi, S. N. R.; Suidan, M.; Smirniotis, P. G.: Novel one-step synthesis of nitrogen-doped TiO_2 by flame aerosol technique for visible-light photocatalysis: Effect of synthesis parameters and secondary nitrogen (N) source. *Chem Eng J* **2018**, *350*, 324-334.

(30) Krstajic, N. V.; Vracar, L. M.; Neophytides, S. G.; Jaksic, J. M.; Murase, K.; Tunold, R.; Jaksic, M. M.: Supported interactive electrocatalysts for hydrogen and oxygen electrode reactions. *J New Mat Electr Sys* **2006**, *9*, 83-97.

(31) Trasatti, S.; Petrii, O. A.: Real Surface-Area Measurements in Electrochemistry. *Pure Appl Chem* **1991**, *63*, 711-734.

(32) Fu, W.; Wang, X. L.; Yang, X. X.; He, X. Q.: $MnCo_2O_4$ Anchored on Nitrogen-Doped Carbon Nanomaterials as an Efficient Electrocatalyst for Oxygen Reduction. *Chemistryselect* **2018**, *3*, 4228-4236.

(33) Jiang, R. Z.; Dong, S.: Rotating-Ring-Disk Electrode Theory Dealing with Nonstationary Electrocatalysis - Study of the Electrocatalytic Reduction of Dioxygen at Cobalt Protoporphyrin Modified Electrode. *J Phys Chem-Us* **1990**, *94*, 7471-7476.

(34) Shao, M. H.; Chang, Q. W.; Dodelet, J. P.; Chenitz, R.: Recent Advances in Electrocatalysts for Oxygen Reduction Reaction. *Chem Rev* **2016**, *116*, 3594-3657.

(35) Holewinski, A.; Linic, S.: Elementary Mechanisms in Electrocatalysis: Revisiting the ORR Tafel Slope. *J Electrochem Soc* **2012**, *159*, H864-H870.

Chapter 5

Ag/TiO_xN_{1-x} Nanocomposites for Studying the Electrooxidation of Carbon Monoxide

Abstract

As the demand for more energy efficient devices increases, more stable and cost-efficient catalysts are needed. One demand is to make more CO-tolerant catalysts to further increase the power output of fuel cells. In this study we synthesized an electrocatalyst with Ag nanoparticles deposited onto oxidized TiN (TiO_xN_{1-x}). Structural analysis shows that Ag nanoparticles nucleated in areas of the oxidized surface, with the bulk structure mainly being TiN. XPS shows a charge transfer Ag to TiO_xN_{1-x} allowing for a more oxidizing surface of Ag. Finally, we found an optimal oxidation time that correlated to the best CO electrooxidation activity, Ag/TiO_xN_{1-x} 1h.

5.1 Introduction

With the ever increase in energy demands, new devices have been looked at to reduce the carbon footprint. One of such devices is the proton exchange membrane fuel cell (PEMFC). A big problem with the commercialization of these devices is if a little carbon monoxide (CO) is present, it will block the active sites of the platinum catalysts and decrease the overall output potential. Platinum group metals (PGMs), including Pd, Pt, Rh, Ir, and Ni are most susceptible to carbon monoxide poisoning because of their

high electrocatalytic activity.[1-4] One solution to this problem has been to operate fuel cells at higher temperatures to promote desorption of the carbon monoxide. However, this proves to not be a good solution due to the higher costs of operation, lowered activity for reactions, and higher likeliness for metal sintering.[5,6] Thereby, it is of the utmost importance to find a catalyst that has a high electrocatalytic activity for fuel cell reactions, but has a high tolerance for CO.

One area researchers have investigated is making Pt-based catalysts more CO tolerant. Recently, Rizo and coworkers developed a PtSn alloy catalyst that showed tolerance for CO monoxide due to activation of H_2O by Sn/SnO_x complexes.[7] The actual Sn content did not shift the onset potential of CO oxidation, but rather the type of support greatly influenced the onset potential of CO oxidation. Carbon nanofibers seemed to outperform the functionalized Vulcan carbons in both acid and base media. Another method of creating more tolerant Pt-based CO catalysts is by changing the support.

After Haruta and co-workers[8] showed the excellent activity of Au/transition metal oxide nanocomposites for CO electrooxidation especially at lower temperatures, many studies have been done to understand more about this reaction. It has become apparent that CO oxidation over Au catalysts is highly dependent on the 1) type of support, 2) the size of the Au, and 3) the structure of the interface.[9-11] The exact mechanism of CO oxidation has been a debate over the past 30 years, but it is clear that the interface between Au and the support and the interaction between Au and the

support are very important.[12] Understanding this interaction is critical developing more CO tolerant catalysts.

However, for the purposes of fuel cell applications, transition metal oxides typically have lower conductivity and contribute to lower fuel cell performance. TiN is an interesting support because of its higher conductivity, higher oxidation resistance, and higher corrosion stability.[13] Haldorai et al. synthesized a Pt@TiN/rGO nanocomposite that showed excellent electrocatalytic activity, long-term stability, and better carbon monoxide tolerance for the electrooxidation of methanol. This became apparent in the higher electrochemical surface area and higher peak current densities for methanol oxidation. They attributed this to the formation of -OH groups and oxy-nitrides on the surface, suppressing the poisoning effects of carbon monoxide on the surface.[14]

In addition, gold is expensive and rare and the need for cheaper catalysts is ever the more critical. Another promising metal which is cheaper and has similar properties to that of Au is Ag. Like Au, Ag's activity is also influenced by the nature of the support. Xu and coworkers developed Ag/SiO_2-based catalysts and tested their catalytic activity for the CO oxidation reaction. It was shown that the nature of the support affected the mobilization and aggregation of Ag nanoparticles and thus affecting the catalytic activity towards CO oxidation.[15] Zhang et al. synthesized Ag nanoparticles deposited onto Al incorporated SBA supports with a combined effect for better CO oxidation. This was due to the CO restructuring the surface of the catalyst thus improving its catalytic activity.[16]

In this study we have created a hybrid catalyst of Ag nanoparticles deposited on top of titanium nitride (TiN) that has small amounts of TiO_2 present which we refer to as titanium oxynitride (TiO_xN_{1-x}) powders. The effect of oxidation time of the surface was studied by changing the heating time of the TiN powders and then depositing Ag nanoparticles on top of the powders. It was shown that the Ag nanoparticles deposit on the TiO_2 areas, thereby making the Ag more oxidized over time and the TiN more oxidized over time. We employed an anodic CO stripping scheme to understand CO electrooxidation and at the same time understand its fuel cell characteristics.[17] This correlated to changing the activity of the CO oxidation with the 1 h time having the best catalytic activity.

5.2 Materials and Methods

5.2.1 Chemicals

Titanium Nitride ~325 mesh powder (Alfa Aesar, 99.5%), silver nitrate (LabChem, ACS), and sodium borohydride VenPure^{TM} SF granules (Acros Organics, 99%) were used as received. Solvents were purchased from typical commercial sources at their highest purity and used without further treatment. Water was supplied from a Barnstead Nanopure Water System (18.3 MΩ cm).

5.2.2 Synthesis of TiO_xN_{1-x} powders

Synthesis of the oxidized TiN was a solid state synthesis that has been published previously.[18] In brief, about 100 mg of TiN powder was weighed out into a ceramic

boat and placed in a Thermolyne 1500 furnace and heated to 450°C at 2°C/min for different amounts of time and then cooled down to room temperature at 2°C/min. The heating time was changed to produce different amounts of oxidation of the TiN. The samples were used as produced and labeled based on their times. Samples are TiO_xN_{1-x} 0 min, TiO_xN_{1-x} 30 min, TiO_xN_{1-x} 1 h, TiO_xN_{1-x} 2 h, and TiO_xN_{1-x} 3 h.[18]

5.2.3 Synthesis of Ag/ TiO_xN_{1-x} composites

Deposition of the silver was done by modifying a previous wet chemical reduction synthesis. In brief, 10 mg of the as synthesized TiO_xN_{1-x} powder was weighed out and placed in a 100 mL round bottom flask. Then around 130 mg of $AgNO_3$ in 60 mL of water was added to the flask and the suspension was cooled down to 0°C for 30 min. Then a cold aqueous solution of $NaBH_4$ (about 40 mg in 10 mL cold water) was added dropwise and the reaction was stirred overnight. The grey precipitate was washed with methanol and vacuum dried to afford the Ag/ TiO_xN_{1-x} composites. Samples are Ag/TiO_xN_{1-x} 0 min, Ag/TiO_xN_{1-x} 30 min, Ag/TiO_xN_{1-x} 1 h, Ag/TiO_xN_{1-x} 2 h, and Ag/TiO_xN_{1-x} 3 h.[19-21]

5.2.4 Structural Characterization

The sample morphologies were examined with a transmission electron microscope (TEM, Philips CM300) operated at 300 kV. X-ray photoelectron spectroscopic (XPS) measurements were carried out with a PHI 5400/XPS instrument equipped with an Al Kα source operated at 350 W and 10□9 Torr. X-ray diffraction

(XRD) measurements were performed with a Rigaku Miniflex powder diffractometer using Cu Kα radiation with a Ni filter (λ = 0.154059 nm at 30 kV and 15 mA) that features a detection limit of 0.04°.

5.2.5 CO electrooxidation

All electrochemical were measurements were done using a Gamry Reference 600^{TM} potentiostat/galvanostat/ZRA. The working electrode was a modified glassy carbon electrode and was polished with a 3 μ Al_2O_3 slurry and washed with milliq water and dried with nitrogen. Inks for modification of the glassy carbon electrode were made by sonication of a 20 μg/3 μL suspension in ethanol with 1% Nafion© addition and drop-casted onto the electrode and dried. Then 3 μL of 20% Nafion© in ethanol (w/w) solution was drop-casted onto the electrode on top the of the catalyst suspension and dried. All measurements were run in 0.5 M H_2SO_4 solution with a graphite counter electrode and Ag/AgCl reference electrode. For comparison, cyclic voltammetry measurements were run in a nitrogen saturated environment for all the samples. To run carbon monoxide electrooxidation measurements, the solution was purged with high purity CO for 15 min and then chronoamperometric measurements were done at -0.3 V vs. Ag/AgCl for 30 min to adsorb CO onto the surface of the catalyst. Then impedance measurements with an AC voltage at 15 mV rms were done at DC voltages of 0.1, 0.2, 0.3, 0.4, 0.5, and 0.6 V vs. Ag/AgCl in the frequency range of 1e6 Hz to 0.1 Hz. Then another chronoamperometric step at -0.3 V vs. Ag/AgCl was done to re-adsorb the CO on the surface. The solution was then purged with N_2 gas for 5 min to

remove excess CO. Finally, CO stripping was done using cyclic voltammetry in the potential range of 0.1 V to 0.6 V to strip the CO from the surface and an electrochemical surface area was calculated based upon the charge from this peak. Impedance measurements Nyquist plots that were fitted equivalent circuit models and the charge transfer resistance was determined for each potential.

5.3 Results and Discussion

5.3.1 Structural Characterization

Nanocomposite morphologies were manifested in TEM measurements. Figure 5.1 portrays of representative TEM images of Ag/TiO_xN_{1-x} nanocomposites. From panels (A_1) and (B_1), it can be seen that the Ag/TiO_xN_{1-x} 1 h and the Ag/TiO_xN_{1-x} 2 h samples are aggregated and polydisperse and it hard to determine the size of the particles. Both samples seem to have similar morphologies showing that the heat and $NaBH_4$ do not affect the morphology of the nanocomposites. Panels (A_2) and (B_2) are HRTEM images of Ag/TiO_xN_{1-x} 1 h and Ag/TiO_xN_{1-x} 2 h respectively. The images show an intimate contact between the Ag and the TiO_xN_{1-x} due to the lattice spacing of the TiO_xN_{1-x} continues onto the Ag spacing. Interplanar distances in panel (A_2) are 0.232 nm and 0.324 nm which are attributed to Ag (111)[22-24] and Rutile TiO_2 (110)[25-27] respectively. In addition, the TiO_2 lattice spacing is only close to the Ag, which means the TiN only oxidized at the surface and the Ag only deposited on the TiO_2 which is further shown by XRD and XPS measurements (vide infra). Interplanar distances in panel (B_2) are 0.243 nm and 0.216 nm which is attributed to TiN(111) and

TiN(200) respectively.[28,29] In this panel, it was very hard to find Ag and TiO_2 which means that the Ag is not monodisperse on the TiO_xN_{1-x} substrate.

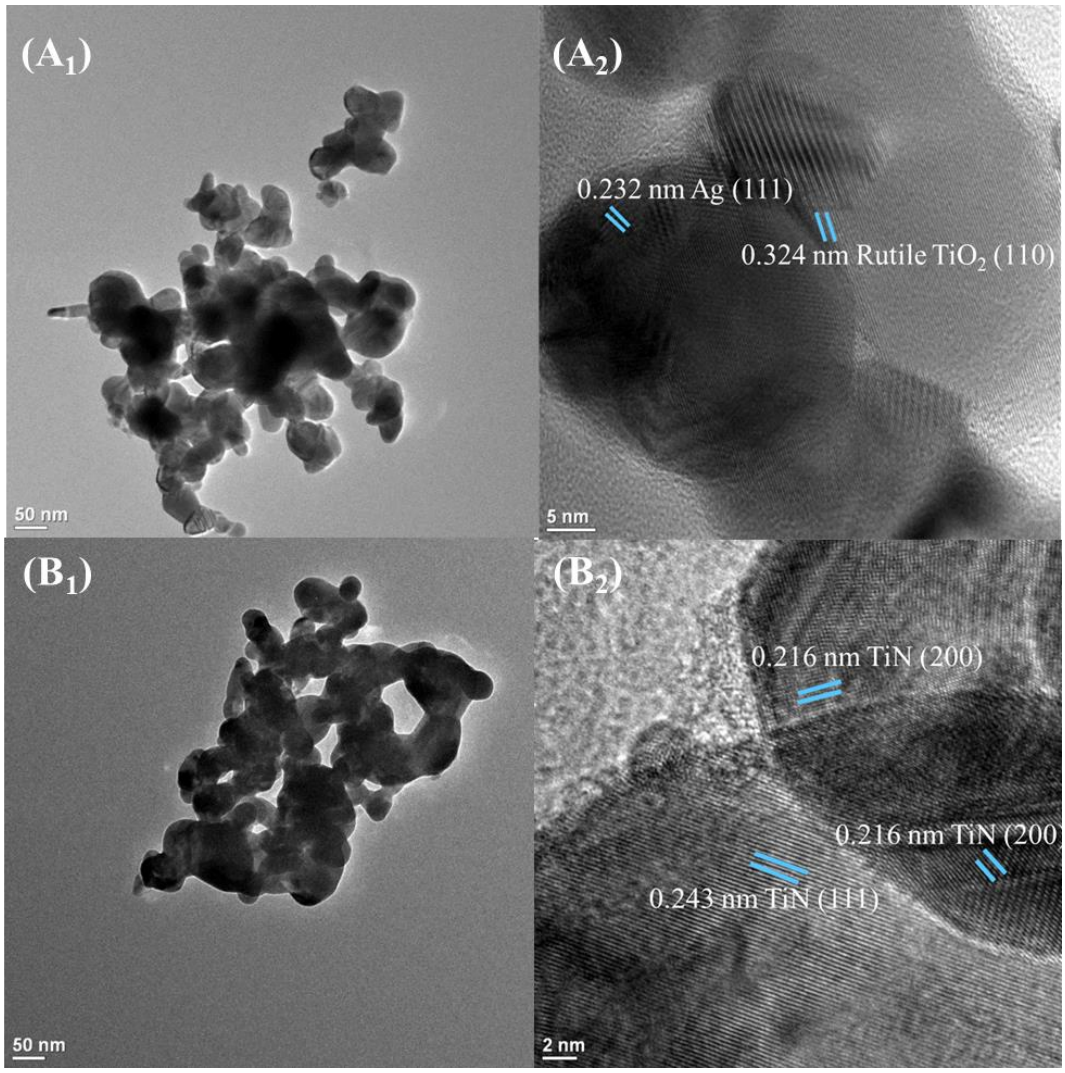

Figure 5.1 Representative TEM images of Ag/TiO_xN_y nanocomposites **(A_1)** and **(A_2)** Ag/TiO_xN_{1-x} 1 h, **(B_1)** and **(B_2)** Ag/TiO_xN_{1-x} 2 h. Scale bars are 50 nm on **(A_1)** and **(B_1)**, 5 nm on **(A_2)**, and 2 nm **(B_2)**.

The Ag/TiO_xN_{1-x} nanocomposite morphologies were then further confirmed by XRD measurements. When looking at Figure 5.2 (A), one can see that there are a series well-defined peaks at $2\theta = 36.8°$ for TiN(111), 42.6° for TiN(200), 61.5° for TiN(220), 74.2° for TiN(311), and 78.2° for TiN(222) (JCPDS no. 38-1420).[30-32] As the oxidation time increases, there also appears to be small diffraction peaks appearing for anatase and Rutile TiO_2 at $2\theta = 25.3°$ for anatase TiO_2(101) (JCPDS no. 00-021-1272)[33], 27.5° for rutile TiO_2(110), and 54.3° for rutile TiO_2(211) (JCPDS no. 21-1276)[34] which agrees with TEM and XPS measurements (vide infra). In Figure 5.2 (B), there are a series of well defined peaks at $2\theta = 38.2°$ for Ag(111), 44.3° for Ag(200), 64.5° for Ag(220), 77.6° for Ag(311), and 81.7° for Ag(222) (JCPDS no. 04-0783).[35-37] All the peaks do not change shape or change position with oxidation time meaning that the oxidation of the TiN does not affect the Ag crystallinity. Figure 5.2 (C) shows a comparison of oxidation time and depsition of silver. Both samples with Ag show the TiN peaks which means that the Ag is in close contact with the substrate which agrees with the TEM measurements. However, there are no peaks for TiO_2 in the samples deposited with Ag which could be that the Ag is blocking the TiO_2.

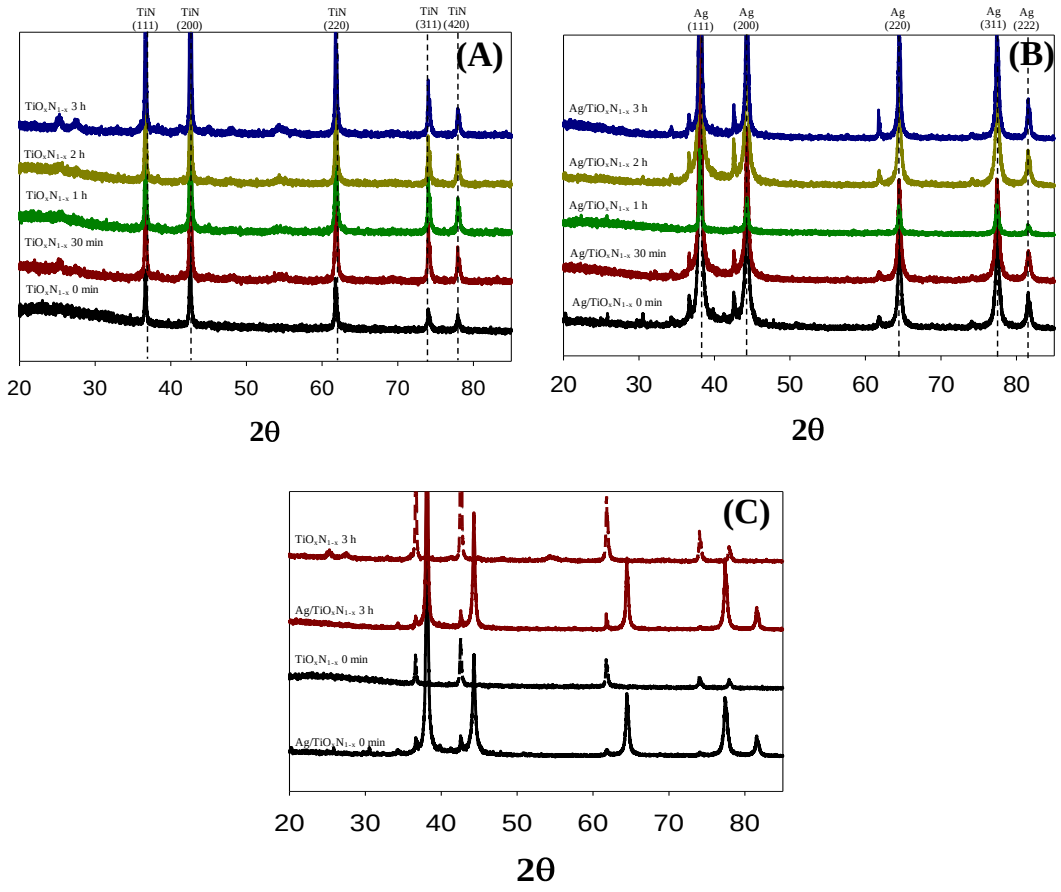

Figure 5.2 XRD spectra of **(A)** TiO_xN_{1-x} nanoparticles oxidized at different times, **(B)** Ag/TiO_xN_{1-x} nanocomposites oxidized at different times, and **(C)** Ag/TiO_xN_{1-x} before and after oxidation and before and after Ag deposition comparison.

5.3.2 Electronic Characterization

The samples were further characterized for charge transfer comparison by doing some XPS measurements. Figure 5.3 shows the survey spectra of all the samples. The spectra revealed peaks at around 280, 370, 400, 460, and 530 eV which correspond to C 1s, Ag 3d, N 1s, Ti 2p, and O 1s electrons.

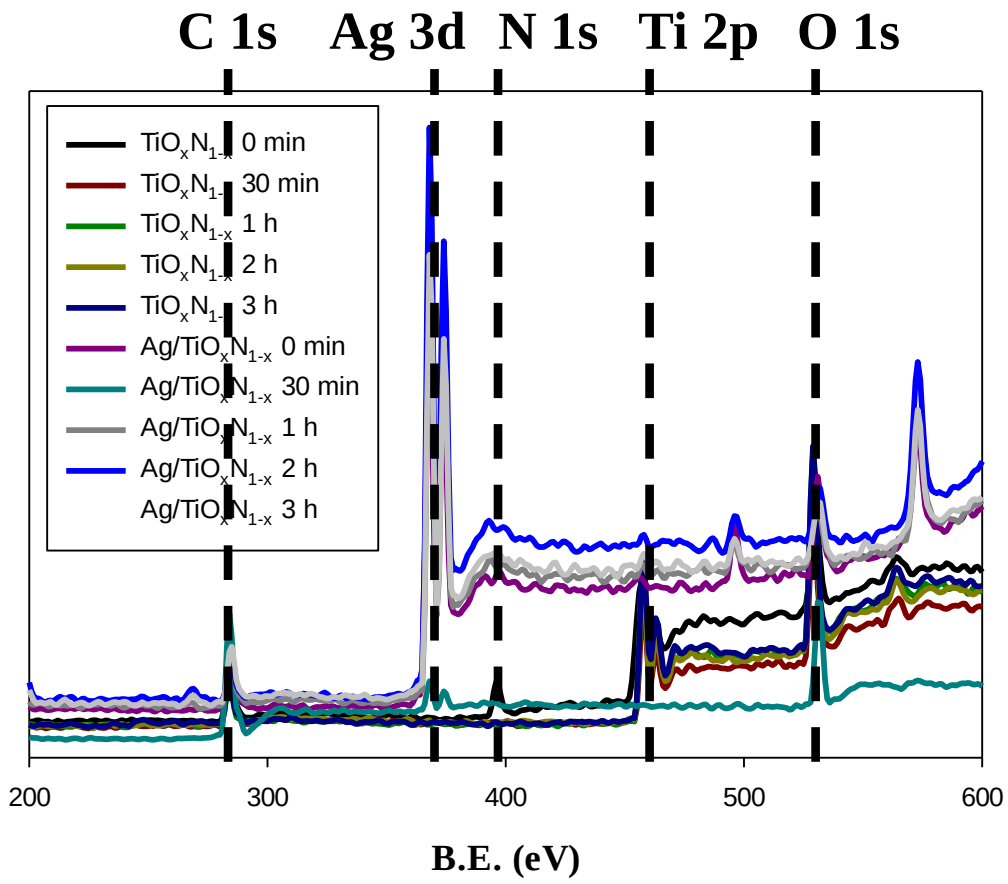

Figure 5.3 XPS survey spectra of all samples.

Elemental analysis and charge transfer were further studied in high resolution XPS measurements. In Figure 3.4, samples without Ag are shown. In the first column, the high resolution spectra of N 1s are shown with the first graph showing two peaks at 399.94 and 397.17 eV for the (A) TiO_xN_{1-x} 0 min sample which are very close to the peak positions of around 399 and 397 eV which corresponds to the TiO_xN_{1-x} and TiN peaks respectively. The rest of the samples show one peak at 399.82 eV, 399.27 eV, 399.31 eV, and 399.31 eV for samples (B) TiO_xN_{1-x} 30 min, (C) TiO_xN_{1-x} 1 h, (D)

TiO_xN_{1-x} 2 h, and (E) TiO_xN_{1-x} 3 h respectively. In addition, the N:Ti atomic ratios are 0.78, 0.11, 0.034, 0.028, and 0.025 for (A) TiO_xN_{1-x} 0 min (B) TiO_xN_{1-x} 30 min, (C) TiO_xN_{1-x} 1 h, (D) TiO_xN_{1-x} 2 h, and (E) TiO_xN_{1-x} 3 h respectively. After the oxidation time the disappearance of the TiN peak and the decreasing N:Ti shows that the surface is being oxidized to TiO_2.[38-40] This confirms the XRD spectra showing peaks for TiO_2 and TiN (*vide infra*). The second column shows the high resolution spectra of O 1s. All of the samples show two peaks at 531.6 and 529.88 eV, 530.98 and 529.48 eV, 531.15 and 529.84 eV, 530.87 and 529.79, and 530.76 and 529.8 eV for (A) TiO_xN_{1-x} 0 min (B) TiO_xN_{1-x} 30 min, (C) TiO_xN_{1-x} 1 h, (D) TiO_xN_{1-x} 2 h, and (E) TiO_xN_{1-x} 3 h respectively. The peak at the higher binding energy around 531-532 eV corresponds to the surface hydroxyl groups deposited on TiO_2 compounds. The peak at the lower binding energy between 528-529 eV corresponds to lattice O_2^{2-} in TiO_2.[41] The atomic ratio between the two peaks for all the samples are 1.89, 0.61, 0.87, 0.83, and 0.66 for (A) TiO_xN_{1-x} 0 min (B) TiO_xN_{1-x} 30 min, (C) TiO_xN_{1-x} 1 h, (D) TiO_xN_{1-x} 2 h, and (E) TiO_xN_{1-x} 3 h respectively. Overall, the amount of surface hydroxides is decreasing with oxidation time. Finally, the last column shows the high resolution Ti 2p XPS spectra for all the samples. The TiO_xN_{1-x} 0 min sample has two pairs of peaks that appear at 464.2, 458.18, 461.91, and 455.94 eV. The first set of peaks that appear correspond to TiO_2 and the second pair of peaks correspond to TiN.[38-41] After the TiN is oxidized the remain samples only have one pair of peaks at 463.96 and 458.28 eV, 464.26 and 458.61 eV, 464.24 and 458.58 eV, and 464.18 and 458.52 eV for samples (B) TiO_xN_{1-}

$_x$ 30 min, (C) TiO_xN_{1-x} 1 h, (D) TiO_xN_{1-x} 2 h, and (E) TiO_xN_{1-x} 3 h respectively. As the oxidation time increases, the Ti is becoming more reduced then oxidized.

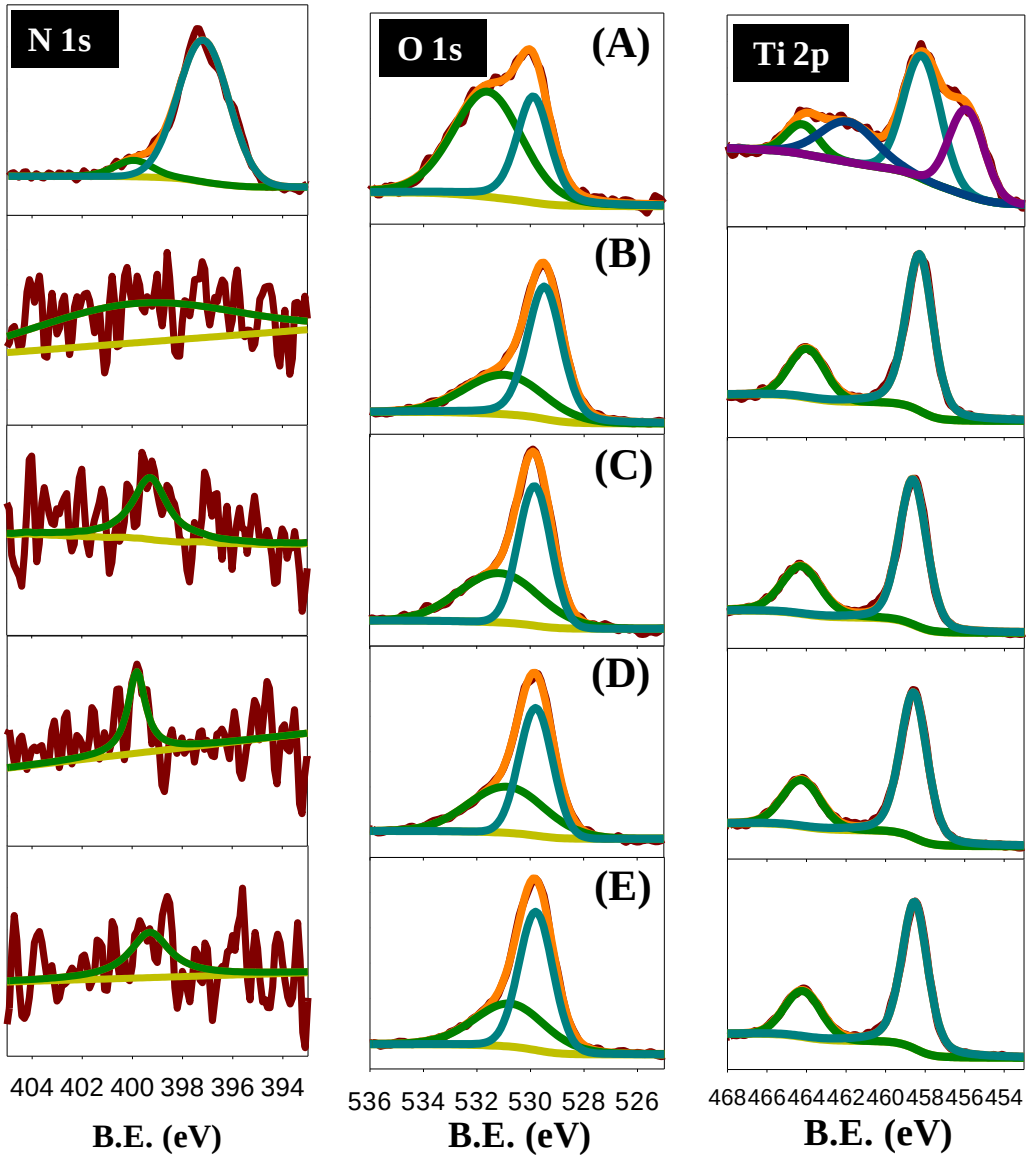

Figure 5.4 High resolution XPS spectra of N 1s, O 1s, and Ti 2p for **(A)** TiO_xN_{1-x} 0 min, **(B)** TiO_xN_{1-x} 30 min, **(C)** TiO_xN_{1-x} 1 h, **(D)** TiO_xN_{1-x} 2 h, and **(E)** TiO_xN_{1-x} 3 h.

XPS measurements of samples with silver deposited onto them are shown in Figure 5.5. In the first column, the high resolution spectra of Ag 3d for all the samples is shown. (A) Ag/TiO_xN_{1-x} 0 min shows two pairs of peaks at 374.75 and 368.77 eV and 373.57 and 367.64 eV. The pair of peaks at the higher binding energy we assign to a Ag^0 species and the second pair of peaks at the lower binding enery we assign to the $Ag^{2=}$ state.[42] So it seems that TiN causes two kids of silver species to be formed when Ag is deposited onto it. The other samples have 1 pair of peaks at 374.82 and 368.79 eV, 374.66 and 368.66 eV, 374.52 and 368.52 eV, and 374.84 and 368.84 eV for (B) Ag/TiO_xN_{1-x} 30 min, (C) Ag/TiO_xN_{1-x} 1 h, (D) Ag/TiO_xN_{1-x} 2 h, and (E) Ag/TiO_xN_{1-x} 3 h respectively. These samples have silver species that correspond to the Ag^0 species. Overall, as the oxidation time increases there is an overall decrease in the binding energy which is showing that the silver is being oxidized.[42] The atomic ratio of Ag:Ti was also found to be 9.34, 2.01, 8.84, 8.45, and 6.81 for (A) Ag/TiO_xN_{1-x} 0 min, (B) Ag/TiO_xN_{1-x} 30 min, (C) Ag/TiO_xN_{1-x} 1 h, (D) Ag/TiO_xN_{1-x} 2 h, and (E) Ag/TiO_xN_{1-x} 3 h respectively. Because these numbers seemed high, we double checked by doing some ICP-OES measurements and found the wt% of Ag in the samples (Figure 5.6). The analysis showed that the samples have 10.6%, 8.79%, 12.8%, 17.0%, and 7.72% wt/wt of Ag for Ag/TiO_xN_{1-x} 0 min, Ag/TiO_xN_{1-x} 30 min, Ag/TiO_xN_{1-x} 1 h, Ag/TiO_xN_{1-x} 2 h, and Ag/TiO_xN_{1-x} 3 h respectively. Since the silver loadings were not the same, the electrochemical data is normalized to this mass to account for changes in activity due to different loadings of silver (*vide infra*).

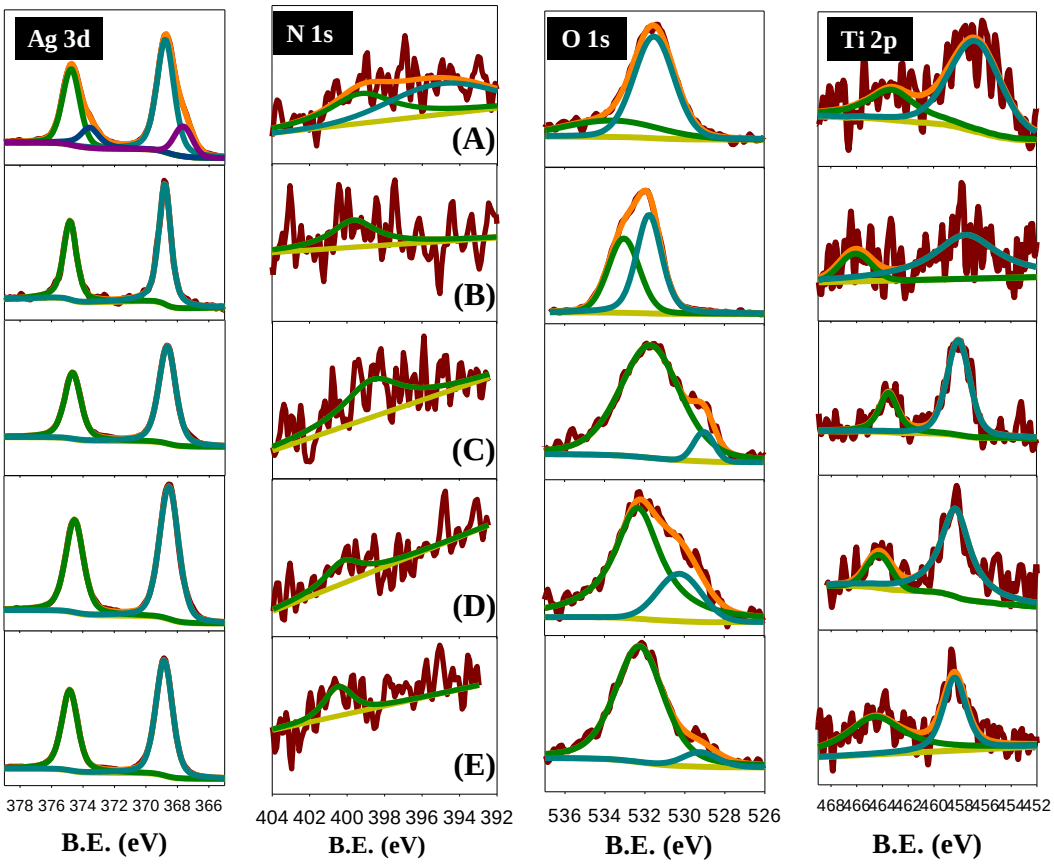

Figure 5.5 High resolution XPS spectra of N 1s, O 1s, and Ti 2p for **(A)** Ag/TiO_xN_{1-x} 0 min, **(B)** Ag/TiO_xN_{1-x} 30 min, **(C)** Ag/TiO_xN_{1-x} 1 h, **(D)** Ag/TiO_xN_{1-x} 2 h, and **(E)** Ag/TiO_xN_{1-x} 3 h.

In the second column, high resolution N 1s spectra are shown. (A) Ag/TiO_xN_{1-x} 0 min shows two peaks at 399.24 and 394.98 eV corresponding to the TiO_xN_{1-x} and TiN peaks respectively. The rest of the samples have one peak at 400.32 eV, 398.66 eV, 400.21 eV, and 400.47 eV for (B) Ag/TiO_xN_{1-x} 30 min, (C) Ag/TiO_xN_{1-x} 1 h, (D)

Ag/TiO_xN_{1-x} 2 h, and (E) Ag/TiO_xN_{1-x} 3 h respectively which corresponds to the TiO_xN_{1-x} species. The fact that the TiN peak disappears after the samples are oxidized means that the surface is becoming oxidized and converting to TiO_2. The N:Ti ratios for the samples were calculated to get a rough estimate of the nitgroen content in the samples. They are 4.27, 5.85, 1.39, 0.55, and 0.48 for (A) Ag/TiO_xN_{1-x} 0 min, (B) Ag/TiO_xN_{1-x} 30 min, (C) Ag/TiO_xN_{1-x} 1 h, (D) Ag/TiO_xN_{1-x} 2 h, and (E) Ag/TiO_xN_{1-x} 3 h respectively. Overall, the N:Ti ratio decreases with oxidation time which means the nitrogen content decreases with oxidation time. This is consistent with the samples becoming more oxidized with oxidation time. In the third column, the high resolution O 1s spectra for the Ag/TiO_xN_{1-x} samples were shown. All the samples have two peaks that appear at 533.62 and 531.52 eV, 533.04 and 531.77 eV, 531.71 and 529.02 eV, 532.33 and 530.23 eV, and 532.27 and 529.23 eV for (A) Ag/TiO_xN_{1-x} 0 min, (B) Ag/TiO_xN_{1-x} 30 min, (C) Ag/TiO_xN_{1-x} 1 h, (D) Ag/TiO_xN_{1-x} 2 h, and (E) Ag/TiO_xN_{1-x} 3 h respectively. The peaks at the higher binding energy have been assigned to the surface hydroxyl groups that deposit on TiO_2 and the peaks at the lower binding energy have been assigned to the O_2^{2-} in the lattice of TiO_2. For almost all the samples it seems the surface hydroxyl group peak is shifted to higher binding energies. The atomic ratio between these two peaks was also calculated to be 0.36, 0.84, 13.13, 3.71, and 11.88 (A) Ag/TiO_xN_{1-x} 0 min, (B) Ag/TiO_xN_{1-x} 30 min, (C) Ag/TiO_xN_{1-x} 1 h, (D) Ag/TiO_xN_{1-x} 2 h, and (E) Ag/TiO_xN_{1-x} 3 h respectively. The surface hydroxyl group content seems to fluctuate between samples as the oxidation time increases. The last column shown the high resolution Ti 2p spectra of the samples. All the samples have one pair of peaks

at 463.27 and 452.76 eV, 466.1 and 457.5 eV, 463.54 and 458.09 eV, 464.28 and 458.33 eV, and 464.58 and 458.4 eV for (A) Ag/TiO_xN_{1-x} 0 min, (B) Ag/TiO_xN_{1-x} 30 min, (C) Ag/TiO_xN_{1-x} 1 h, (D) Ag/TiO_xN_{1-x} 2 h, and (E) Ag/TiO_xN_{1-x} 3 h respectively. Overall, the samples seem to have an increase in binding energy which means the samples are being oxidized as oxidation time is increasing. This implicates a charge transfer from the Ag to the titanium oxynitride.[43,44]

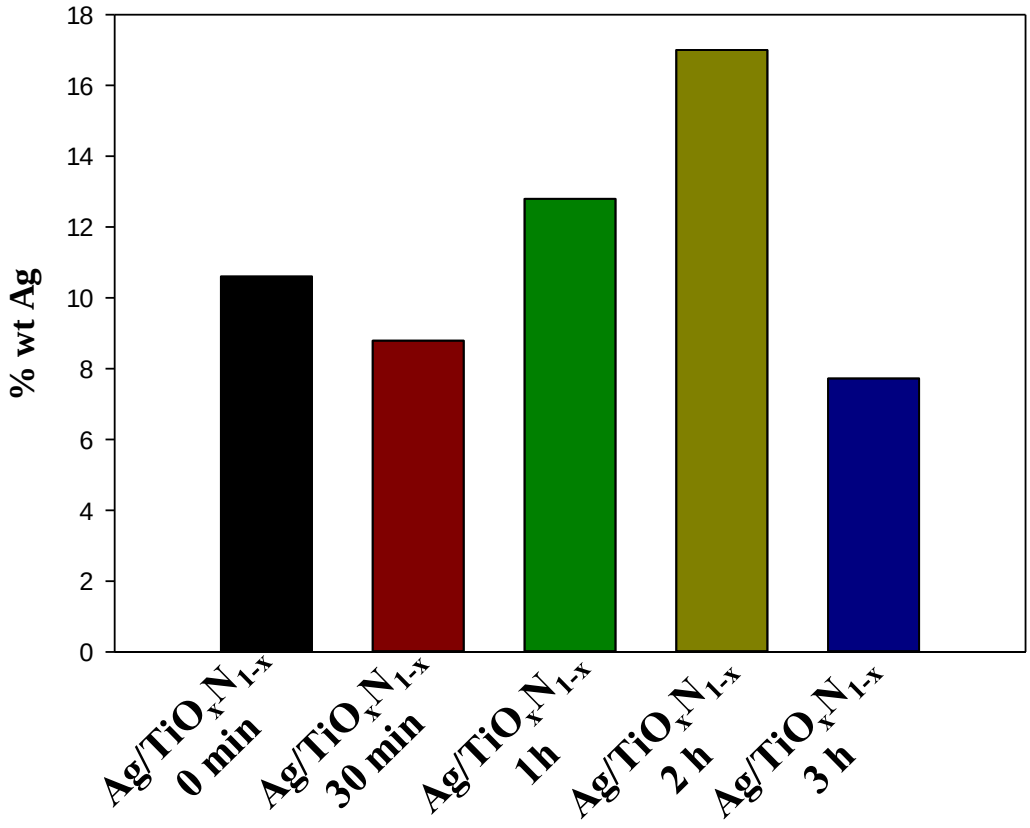

Figure 5.6 ICP-OES analysis of Ag/TiO_xN_{1-x} samples.

5.3.3 CO Electrooxidation

Electrochemical behavior for electrooxidation of carbon monoxide was studied using cyclic voltammetry measurements. As a comparison, a commercial Pt/C catalyst was studied to compare metals and silver nanoparticles were deposited on carbon black labeled as Ag/C was studied to understand the effects of using titanium oxynitride as a support. In Figure 5.7 (A), N_2 saturated cyclic voltammetry measurements were done in 0.5 M H_2SO_4 at 10 mV/s are shown. For the silver samples, the cyclic voltammograms were scanned between -0.1 V and 0.8 V vs. Ag/AgCl and for the Pt/C sample it was scanned between -0.3 and 0.9 V vs. Ag/AgCl. For the silver samples, the voltammogram does not show any peaks in the given range. For comparison, the samples without Ag were scanned in the same samples as those with Ag (Figure 5.7 (B)). In it apparent that are also no peaks shown in both voltammograms. This shows that in this range there is no activity that interferes with CO electrooxidation.[45] For the Pt/C sample, there appears to be the typical Pt butterfly showing H_2 adsorption/desorption and O_2 adsorption/desorption.[46-48] In Figure 5.7 (C), CO stripping measurements done in a N_2 saturated 0.5 M H_2SO_4 solution are shown. For all the samples have one peak appearing at 0.304 V vs. Ag/AgCl, 0.328 V vs. Ag/AgCl, 0.292 V vs. Ag/AgCl, 0.310 V vs. Ag/AgCl, 0.294 V vs. Ag/AgCl, 0.612 V vs. Ag/AgCl, and 0.322 V vs. Ag/AgCl for Ag/TiO_xN_{1-x} 0 min, Ag/TiO_xN_{1-x} 30 min, Ag/TiO_xN_{1-x} 1 h, Ag/TiO_xN_{1-x} 2 h, Ag/TiO_xN_{1-x} 3 h, Pt/C, and Ag/C respectively. The peaks for Ag correlate well with literature data.[49] For comparison, CO stripping measurements done in N_2 saturated 0.5 M H2SO4 at 10 mV/s for all TiO_xN_{1-x} samples are shown in Figure 5.7 (D). None of the samples have any major peaks shown in the

voltammogram which means that the CO electrooxidation requires an interaction between the Ag and TiO_xN_{1-x}. A final comparison between scans in shown in Figure 5.7 (E) which is a representative image of all the samples. In the black solid line of the first scan, it's apparent that the Ag/TiO_xN_{1-x} 2 h sample has a pronounced CO stripping peak. In the black dotted curve of the 2nd scan, that peak as disappeared showing that all the CO is removed from the first scan. The red curve is the N_2 saturated scan shown for comparison which shows that the 2nd scan of the CO stripping becomes just like that scan. This means that these samples don't hold onto CO for very long.

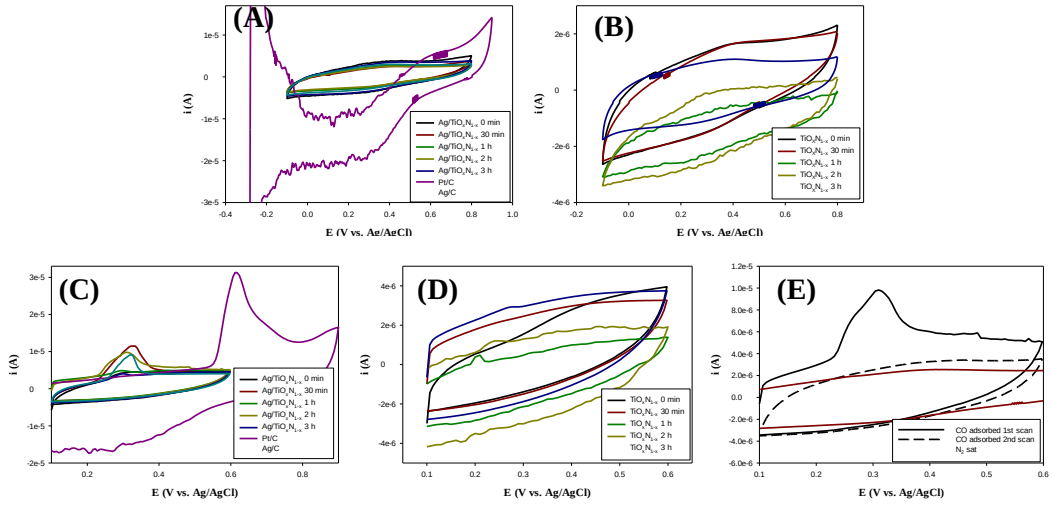

Figure 5.7 (A) N_2 saturated cyclic voltammetry measurements done in 0.5 M H_2SO_4 at 10 mV/s for all samples with metals deposited on them. **(B)** N_2 saturated cyclic voltammetry measurements done in 0.5 M H_2SO_4 at 10 mV/s for all TiO_xN_{1-x} samples. **(C)** CO stripping measurements done in N_2 saturated 0.5 M H_2SO_4 at 10 mV/s for all samples with metals deposited on them. **(D)** CO stripping measurements done in N2 saturated 0.5 M H2SO4 at 10 mV/s for all TiO_xN_{1-x} samples. **(E)** Representative CO

stripping voltammagram of Ag/TiO_xN_{1-x} 2 h's 1st and 2nd scan in N_2 saturated 0.5 M H_2SO_4 compared to just N_2 saturated scan.

Figure 5.8 shows bar graphs of the values of the peak potential (A), peak current density (B), and electrochemical surface area (C). When comparing the peak potential, overall as oxidation time increases the peak potential becomes more negative and reaches an optimal peak potential at 1 h and then slightly becomes more positive. The current at the peak potential was divided by the mass loading calculated from ICP-OES measurements and was determined to be 2.07, 10.7, 1.91, 2.89, 2.58, 19.4, and 0.4580 A/cm^2 Ag/TiO_xN_{1-x} 0 min, Ag/TiO_xN_{1-x} 30 min, Ag/TiO_xN_{1-x} 1 h, Ag/TiO_xN_{1-x} 2 h, Ag/TiO_xN_{1-x} 3 h, Pt/C, and Ag/C respectively.. It seems as the oxidation time increases there is a decrease in peak current density and then an increase in the peak current density. Finally, the electrochemical surface areas of all the samples were 0.305, 0.605, 0.248, 0.576, 0.193, 1.046, and 0.346 cm^2 for Ag/TiO_xN_{1-x} 0 min, Ag/TiO_xN_{1-x} 30 min, Ag/TiO_xN_{1-x} 1 h, Ag/TiO_xN_{1-x} 2 h, Ag/TiO_xN_{1-x} 3 h, Pt/C, and Ag/C respectively. Based on these measurements, it seems that the Ag/TiO_xN_{1-x} has the best activity for this reaction.

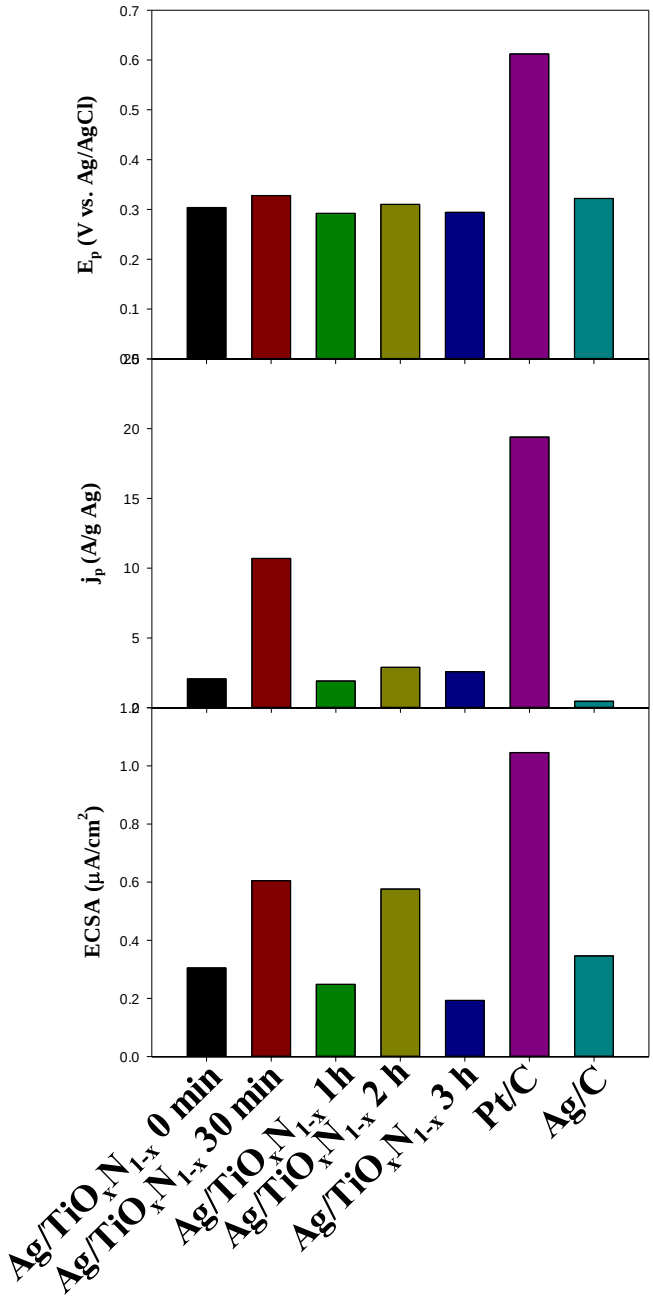

Figure 5.8 Bar graphs for summary of CV results of Ag/TiO_xN_{1-x} samples.

CO electrooxidation was further studied using Impedance measurements to make Nyquist plots which are shown in Figure 5.9 for a DC voltage of 0.3 V vs. Ag/AgCl. Figure 5.10 shows the equivalent circuit model used to fit the Nyquist plot for the DC voltage of 0.3 V vs. Ag/AgCl. This circuit was used because there seems to be a significant diffusion component which is attributed to the O_2 adsorption in the CO oxidation mechanism.[50-52] The first thing to notice is the typical semicircle is not present this is due to the fast reaction kinetics of this reaction due to fast proton transfer.[38] Across the potentials, it is shown from the Nyquist plots that the Pt/C sample has the highest charge transfer resistance, which is shown by the largest diameter of the semicircle. This correlates back to the CO stripping measurements because the Pt/C sample had the most positive peak potential. The next thing to notice, is the Ag samples all had roughly similar charge transfer resistances that correlates to the very close anodic CO stripping peak potential. This result is further indicative that Ag is a better catalyst than Pt when reactions involve CO.

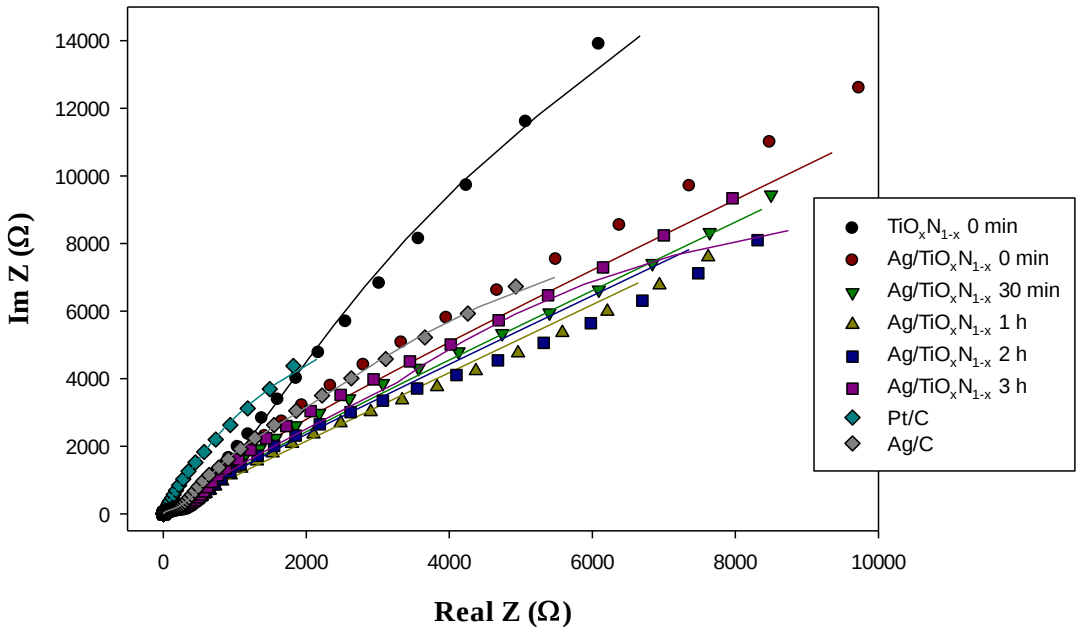

Figure 5.9 Nyquist Plots for all Ag/TiO_xN_{1-x} samples made from impedance measurements taken in CO saturated 0.5 M H_2SO_4 done at DC voltage of 0.3 V vs. Ag/AgCl.

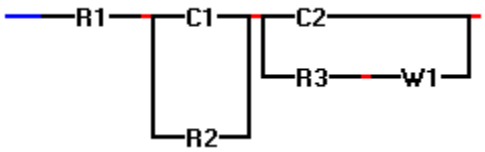

Figure 5.10 Equivalent circuit model used for a DC voltage of 0.3 V vs. Ag/AgCl.

Taking a closer look at the impedance results, the charge transfer resistance of the samples was plotted in Figure 5.11. Again, overall all the Ag samples have lower charge transfer resistances than Pt except for the Ag/C sample which again shows that

Ag is better at oxidizing CO. Another interesting observation is that the charge transfer resistance decreases then increases with oxidation time having Ag/TiO_xN_{1-x} 1h having the lowest charge transfer resistance. This correlate back to the CV data because Ag/TiO_xN_{1-x} 1h had the most negative CO oxidation peak potential. This also further affirms that the nature of the support affects the reaction kinetics. When compared to the Ag/C sample, the charge transfer resistance in the Ag/C is much higher than all the TiO_xN_{1-x} samples. This shows that transition metal oxynitrides are much better supports for this reaction than carbons are.

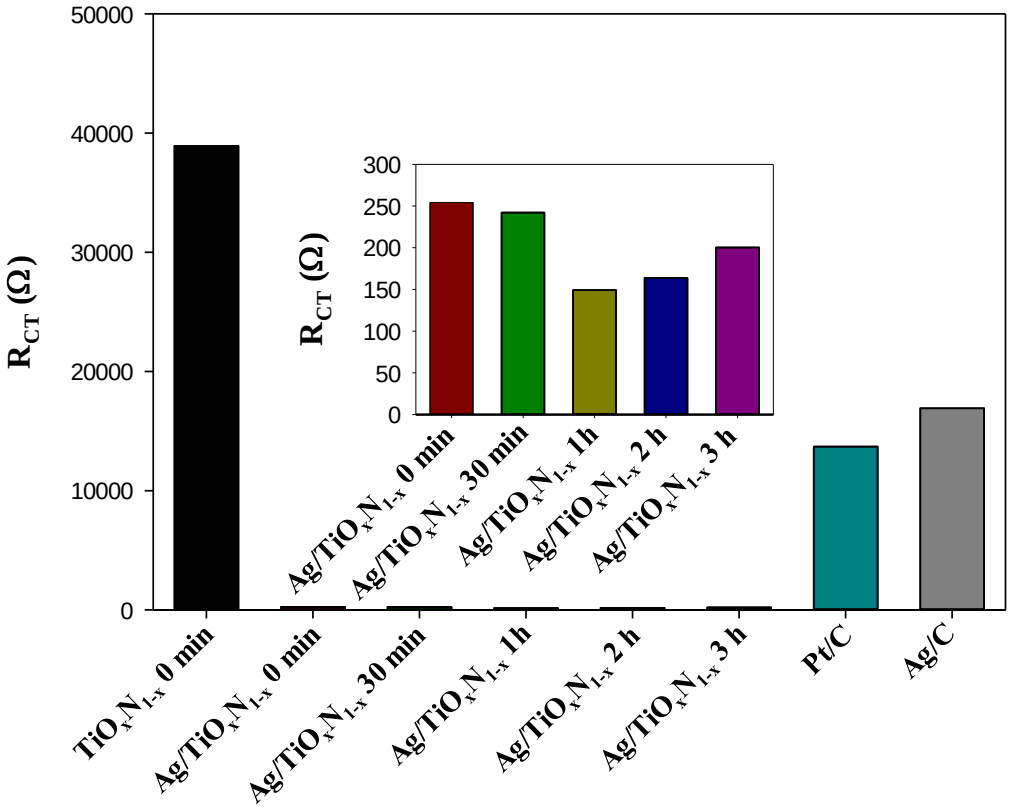

Figure 5.11 Charge transfer resistance of Ag/TiO_xN_{1-x} samples at a DC voltage of 0.3 V vs. Ag/AgCl.

Overall, this study further proves that the nature of the support is very important for CO electrooxidation and designing fuel cell catalysts. Structural analysis showed that we have Ag nanoparticles deposited onto TiO_xN_{1-x} powders with only the surface being oxidized. TEM showed that the Ag tended to nucleate near the TiO_2 areas (or oxidized areas) due to the strong-metal-support-interaction between Ag and TiO_2.[53] Further exploring the structure, as the oxidation time increased, the surface of the powders changed by becoming more reduced due to a charge transfer from the Ag to the TiO_xN_{1-x}. This in turn affected the activity of CO electrooxidation by allowing for an optimal amount of oxidation of the surface, being 1 h having the most negative CO stripping potential which also correlates to the impedance analysis with having a relatively lower charge transfer resistance. It has been shown in a previous study that CO adsorption is favored[54] when the interface is oxidized thereby oxidizing the interface of the nanopowders we have changed the CO binding energy to the interface. Based on this finding, the CO electrooxidation behavior is directly correlated to the CO binding energy at the interface, with an optimal CO binding energy and thus optimal CO electrooxidation activity.

5.4 Conclusion

We have successfully synthesized Ag/TiO_xN_{1-x} powders for studying the electrooxidation of CO by nature of changing the support. Structural characterization shows that Ag nanoparticles are deposited onto oxidized areas of the TiN with the bulk structure mainly being TiN. This allowed for a change in the oxidation state of the Ag nanoparticles and in turn changing the electrooxidation behavior of the nanopowders. Thus, we have found the optimal oxidation time to be 1 hour.

5.5 References

(1) Baschuk, J. J.; Li, X. G.: Carbon monoxide poisoning of proton exchange membrane fuel cells. *Int J Energ Res* **2001**, *25*, 695-713.

(2) Ciapina, E. G.; Santos, S. F.; Gonzalez, E. R.: Electrochemical CO stripping on nanosized Pt surfaces in acid media: A review on the issue of peak multiplicity. *J Electroanal Chem* **2018**, *815*, 47-60.

(3) Zinola, C. F.: A Method for the Synthesis of Platinum Nanoparticles with Defined Crystalline Orientations and Their Catalytic Activity towards Nitrogen and Carbon Monoxide Oxidations. *J Electrochem Soc* **2017**, *164*, H170-H182.

(4) Sadhukhan, M.; Kundu, M. K.; Bhowmik, T.; Barman, S.: Highly dispersed platinum nanoparticles on graphitic carbon nitride: A highly active and durable electrocatalyst for oxidation of methanol, formic acid and formaldehyde. *Int J Hydrogen Energ* **2017**, *42*, 9371-9383.

(5) Darby, M. T.; Sykes, E. C. H.; Michaelides, A.; Stamatakis, M.: Carbon Monoxide Poisoning Resistance and Structural Stability of Single Atom Alloys. *Top Catal* **2018**, *61*, 428-438.

(6) Sondergaard, S.; Cleemann, L. N.; Jensen, J. O.; Bjerrum, N. J.: Influence of carbon monoxide on the cathode in high-temperature polymer electrolyte membrane fuel cells. *Int J Hydrogen Energ* **2017**, *42*, 3309-3315.

(7) Rizo, R.; Sebastian, D.; Lazaro, M. J.; Pastor, E.: On the design of Pt-Sn efficient catalyst for carbon monoxide and ethanol oxidation in acid and alkaline media. *Appl Catal B-Environ* **2017**, *200*, 246-254.

(8) Haruta, M.; Yamada, N.; Kobayashi, T.; Iijima, S.: Gold Catalysts Prepared by Coprecipitation for Low-Temperature Oxidation of Hydrogen and of Carbon-Monoxide. *J Catal* **1989**, *115*, 301-309.

(9) Haruta, M.; Tsubota, S.; Kobayashi, T.; Kageyama, H.; Genet, M. J.; Delmon, B.: Low-Temperature Oxidation of CO over Gold Supported on TiO_2, Alpha-Fe_2O_3, and Co_3O_4. *J Catal* **1993**, *144*, 175-192.

(10) Haruta, M.; Kobayashi, T.; Sano, H.; Yamada, N.: Novel Gold Catalysts for the Oxidation of Carbon-Monoxide at a Temperature Far Below 0-Degrees-C. *Chem Lett* **1987**, 405-408.

(11) Laoufi, I.; Saint-Lager, M. C.; Lazzari, R.; Jupille, J.; Robach, O.; Garaudee, S.; Cabailh, G.; Dolle, P.; Cruguel, H.; Bailly, A.: Size and Catalytic Activity of Supported Gold Nanoparticles: An in Operando Study during CO Oxidation. *J Phys Chem C* **2011**, *115*, 4673-4679.

(12) Saavedra, J.; Pursell, C. J.; Chandler, B. D.: CO Oxidation Kinetics over Au/TiO_2 and Au/Al_2O_3 Catalysts: Evidence for a Common Water-Assisted Mechanism. *J Am Chem Soc* **2018**, *140*, 3712-3723.

(13) Li, H. P.; Pan, W.; Zhang, W.; Huang, S. Y.; Wu, H.: TiN Nanofibers: A New Material with High Conductivity and Transmittance for Transparent Conductive Electrodes. *Adv Funct Mater* **2013**, *23*, 209-214.

(14) Haldorai, Y.; Arreaga-Salas, D.; Rak, C. S.; Huh, Y. S.; Han, Y. K.; Voit, W.: Platinized titanium nitride/graphene ternary hybrids for direct methanol fuel cells and titanium nitride/graphene composites for high performance supercapacitors. *Electrochim Acta* **2016**, *220*, 465-474.

(15) Xu, J.; Zhang, J. Y.; Peng, H. G.; Xu, X. L.; Liu, W. M.; Wang, Z.; Zhang, N.; Wang, X.: Ag supported on meso-structured SiO_2 with different morphologies for CO oxidation: On the inherent factors influencing the activity of Ag catalysts. *Micropor Mesopor Mat* **2017**, *242*, 90-98.

(16) Zhang, X. D.; Dong, H.; Wang, Y.; Liu, N.; Zuo, Y. H.; Cui, L. F.: Study of catalytic activity at the Ag/Al-SBA-15 catalysts for CO oxidation and selective CO oxidation. *Chem Eng J* **2016**, *283*, 1097-1107.

(17) Vidakovic, T.; Christov, M.; Sundmacher, K.: The use of CO stripping for in situ fuel cell catalyst characterization. *Electrochim Acta* **2007**, *52*, 5606-5613.

(18) Wu, Z. B.; Dong, F.; Zhao, W. R.; Guo, S.: Visible light induced electron transfer process over nitrogen doped TiO_2 nanocrystals prepared by oxidation of titanium nitride. *J Hazard Mater* **2008**, *157*, 57-63.

(19) Lu, B. Z.; Yao, B.; Roseman, G.; Deming, C. P.; Lu, J. E.; Millhauser, G. L.; Li, Y.; Chen, S. W.: Ethanol Oxidation Reaction Catalyzed by Palladium Nanoparticles Supported on Hydrogen-Treated TiO_2 Nanobelts: Impact of Oxygen Vacancies. *Chemelectrochem* **2017**, *4*, 2211-2217.

(20) Sweeney, S. W.; Roseman, G.; Deming, C. P.; Wang, N.; Nguyen, T. A.; Millhauser, G. L.; Chen, S. W.: Impacts of oxygen vacancies on the electrocatalytic activity of $AuTiO_2$ nanocomposites towards oxygen reduction. *Int J Hydrogen Energ* **2016**, *41*, 18005-18014.

(21) Liu, K.; Song, Y.; Chen, S. W.: Defective TiO_2-supported Cu nanoparticles as efficient and stable electrocatalysts for oxygen reduction in alkaline media. *Nanoscale* **2015**, *7*, 1224-1232.

(22) Wen, T.; Zhang, D. X.; Liu, J.; Zhang, H. X.; Zhang, J.: Facile synthesis of bimetal Au-Ag nanoparticles in a Cu(I) boron imidazolate framework with mechanochromic properties. *Chem Commun* **2015**, *51*, 1353-1355.

(23) Sareen, S.; Mutreja, V.; Singh, S.; Pal, B.: Highly dispersed Au, Ag and Cu nanoparticles in mesoporous SBA-15 for highly selective catalytic reduction of nitroaromatics. *Rsc Adv* **2015**, *5*, 184-190.

(24) Qian, T. T.; Li, J. H.; Min, X.; Guan, W. M.; Deng, Y.; Ning, L.: Enhanced thermal conductivity of PEG/diatomite shape-stabilized phase change materials with Ag nanoparticles for thermal energy storage. *J Mater Chem A* **2015**, *3*, 8526-8536.

(25) Shen, Z. F.; Wang, G. Q.; Tian, H.; Sunarso, J.; Liu, L. H.; Liu, J.; Liu, S. M.: Bi-layer photoanode films of hierarchical carbon-doped brookite-rutile TiO_2 composite and anatase TiO_2 beads for efficient dye-sensitized solar cells. *Electrochim Acta* **2016**, *216*, 429-437.

(26) Liu, Y.; Zhou, S.; Li, J. M.; Wang, Y. J.; Jiang, G. Y.; Zhao, Z.; Liu, B.; Gong, X. Q.; Duan, A. J.; Liu, J.; Wei, Y. C.; Zhang, L. Q.: Photocatalytic reduction of CO_2 with water vapor on surface La-modified TiO_2 nanoparticles with enhanced CH_4 selectivity. *Appl Catal B-Environ* **2015**, *168*, 125-131.

(27) Liu, J.; Yu, X. L.; Liu, Q. Y.; Liu, R. J.; Shang, X. K.; Zhang, S. S.; Li, W. H.; Zheng, W. Q.; Zhang, G. J.; Cao, H. B.; Gu, Z. J.: Surface-phase junctions of branched TiO_2 nanorod arrays for efficient photoelectrochemical water splitting. *Appl Catal B-Environ* **2014**, *158*, 296-300.

(28) Qin, P.; Li, X. X.; Gao, B.; Fu, J. J.; Xia, L.; Zhang, X. M.; Huo, K. F.; Shen, W. L.; Chu, P. K.: Hierarchical TiN nanoparticles-assembled nanopillars for flexible supercapacitors with high volumetric capacitance. *Nanoscale* **2018**, *10*, 8728-8734.

(29) Zhang, Q. T.; Wang, Y. H.; Wang, Y. C.; Al-Enizi, A. M.; Elzatahry, A. A.; Zheng, G. F.: Myriophyllum-like hierarchical TiN@Ni_3N nanowire arrays for bifunctional water splitting catalysts. *J Mater Chem A* **2016**, *4*, 5713-5718.

(30) Ishii, S.; Sugavaneshwar, R. P.; Nagao, T.: Titanium Nitride Nanoparticles as Plasmonic Solar Heat Transducers. *J Phys Chem C* **2016**, *120*, 2343-2348.

(31) Lin, L. L.; Starostin, S. A.; Wang, Q.; Hessel, V.: An atmospheric pressure microplasma process for continuous synthesis of titanium nitride nanoparticles. *Chem Eng J* **2017**, *321*, 447-457.

(32) Tang, D. H.; Yi, R.; Gordin, M. L.; Melnyk, M.; Dai, F.; Chen, S. R.; Song, J. X.; Wang, D. H.: Titanium nitride coating to enhance the performance of silicon nanoparticles as a lithium-ion battery anode. *J Mater Chem A* **2014**, *2*, 10375-10378.

(33) Wu, L. M.; Buchholz, D.; Bresser, D.; Chagas, L. G.; Passerini, S.: Anatase TiO_2 nanoparticles for high power sodium-ion anodes. *J Power Sources* **2014**, *251*, 379-385.

(34) Zhang, D. Q.; Wen, M. C.; Zhang, S. S.; Liu, P. J.; Zhu, W.; Li, G. S.; Li, H. X.: Au nanoparticles enhanced rutile TiO_2 nanorod bundles with high visible-light photocatalytic performance for NO oxidation. *Appl Catal B-Environ* **2014**, *147*, 610-616.

(35) Wang, S. L.; Liu, N. S.; Tao, J. Y.; Yang, C. X.; Liu, W. J.; Shi, Y. L.; Wang, Y. M.; Su, J.; Li, L. Y.; Gao, Y. H.: Inkjet printing of conductive patterns and supercapacitors using a multi-walled carbon nanotube/Ag nanoparticle based ink. *J Mater Chem A* **2015**, *3*, 2407-2413.

(36) Ge, M. Z.; Cao, C. Y.; Li, S. H.; Tang, Y. X.; Wang, L. N.; Qi, N.; Huang, J. Y.; Zhang, K. Q.; Al-Deyab, S. S.; Lai, Y. K.: In situ plasmonic Ag nanoparticle anchored TiO_2 nanotube arrays as visible-light-driven photocatalysts for enhanced water splitting. *Nanoscale* **2016**, *8*, 5226-5234.

(37) Obeydavi, A.; Dastafkan, K.; Rahimi, M.; Dezfouli, M. A. G.: Insights into post-annealing and silver doping effects on the internal microstructure of ZnO nanoparticles through X-ray diffraction probe. *Solid State Sci* **2017**, *69*, 71-81.

(38) Achour, A.; Porto, R. L.; Soussou, M. A.; Islam, M.; Boujtita, M.; Aissa, K. A.; Le Brizoual, L.; Djouadi, A.; Brousse, T.: Titanium nitride films for micro-supercapacitors: Effect of surface chemistry and film morphology on the capacitance. *J Power Sources* **2015**, *300*, 525-532.

(39) Hasegawa, G.; Kitada, A.; Kawasaki, S.; Kanamori, K.; Nakanishi, K.; Kobayashi, Y.; Kageyama, H.; Abe, T.: Impact of Electrolyte on Pseudocapacitance and Stability of Porous Titanium Nitride (TiN) Monolithic Electrode. *J Electrochem Soc* **2015**, *162*, A77-A85.

(40) Zhou, X. M.; Zolnhofer, E. M.; Nguyen, N. T.; Liu, N.; Meyer, K.; Schmuki, P.: Stable Co-Catalyst-Free Photocatalytic H_2 Evolution From Oxidized Titanium Nitride Nanopowders. *Angew Chem Int Edit* **2015**, *54*, 13385-13389.

(41) Bertoti, I.; Mohai, M.; Sullivan, J. L.; Saied, S. O.: Surface Characterization of Plasma-Nitrided Titanium - an XPS Study. *Appl Surf Sci* **1995**, *84*, 357-371.

(42) Van Viet, P.; Phan, B. T.; Mott, D.; Maenosono, S.; Sang, T. T.; Thi, C. M.; Van Hieu, L.: Silver nanoparticle loaded TiO_2 nanotubes with high photocatalytic and antibacterial activity synthesized by photoreduction method. *J Photoch Photobio A* **2018**, *352*, 106-112.

(43) Xin, B. F.; Jing, L. Q.; Ren, Z. Y.; Wang, B. Q.; Fu, H. G.: Effects of simultaneously doped and deposited ag on the photocatalytic activity and surface states of TiO_2. *J Phys Chem B* **2005**, *109*, 2805-2809.

(44) Yu, J. G.; Xiong, J. F.; Cheng, B.; Liu, S. W.: Fabrication and characterization of Ag-TiO_2 multiphase nanocomposite thin films with enhanced photocatalytic activity. *Appl Catal B-Environ* **2005**, *60*, 211-221.

(45) Giovanni, M.; Pumera, M.: Size Dependant Electrochemical Behavior of Silver Nanoparticles with Sizes of 10, 20, 40, 80 and 107 nm. *Electroanal* **2012**, *24*, 615-617.

(46) Luo, M. H.; Yao, W. F.; Huang, C. P.; Wu, Q.; Xu, Q. J.: Shape effects of Pt nanoparticles on hydrogen production via Pt/CdS photocatalysts under visible light. *J Mater Chem A* **2015**, *3*, 13884-13891.

(47) Do, C. L.; Pham, T. S.; Nguyen, N. P.; Tran, V. Q.: Properties of Pt/C nanoparticle catalysts synthesized by electroless deposition for proton exchange membrane fuel cell. *Adv Nat Sci-Nanosci* **2013**, *4*.

(48) Baron, R.; Campbell, F. W.; Streeter, I.; Xiao, L.; Compton, R. G.: Facile method for the construction of random nanoparticle arrays on a carbon support for the development of well-defined catalytic surfaces. *Int J Electrochem Sc* **2008**, *3*, 556-565.

(49) Hu, C. Y.; Mu, X. L.; Fan, J. M.; Ma, H. B.; Zhao, X. J.; Chen, G. X.; Zhou, Z. Y.; Zheng, N. F.: Interfacial Effects in PdAg Bimetallic Nanosheets for Selective Dehydrogenation of Formic Acid. *Chemnanomat* **2016**, *2*, 28-32.

(50) Lepage, G.; Albernaz, F. O.; Perrier, G.; Merlin, G.: Characterization of a microbial fuel cell with reticulated carbon foam electrodes. *Bioresource Technol* **2012**, *124*, 199-207.

(51) Froschl, T.; Hormann, U.; Kubiak, P.; Kucerova, G.; Pfanzelt, M.; Weiss, C. K.; Behm, R. J.; Husing, N.; Kaiser, U.; Landfester, K.; Wohlfahrt-Mehrens, M.: High surface area crystalline titanium dioxide: potential and limits in electrochemical energy storage and catalysis. *Chem Soc Rev* **2012**, *41*, 5313-5360.

(52) Haruta, M.: Nanoparticulate gold catalysts for low-temperature CO oxidation. *J New Mat Electr Sys* **2004**, *7*, 163-172.

(53) Duan, Y. Y.; Luo, J. M.; Zhou, S. C.; Mao, X. Y.; Shah, M. W.; Wang, F.; Chen, Z. H.; Wang, C. Y.: TiO_2-supported Ag nanoclusters with enhanced visible light activity for the photocatalytic removal of NO. *Appl Catal B-Environ* **2018**, *234*, 206-212.

(54) Duan, Z. Y.; Henkelman, G.: Calculations of CO Oxidation over a Au/TiO_2 Catalyst: A Study of Active Sites, Catalyst Deactivation, and Moisture Effects. *Acs Catal* **2018**, *8*, 1376-1383.

Chapter 6

Summary and Future Work

6.1 Summary

In conclusion manipulating the defects in TiO_2 and TiN have been described in the preceding chapters. Chapters 2-4 deal with looking at TiO_2 as a support and understanding how the defects play a role in the kinetics of the oxygen reduction reaction. Chapter 5 employs the use of TiO_xN_y substrate how its oxidation affects the carbon monoxide oxidation reaction.

6.2 Summary of Impacts of Defects in TiO_2 in ORR

In Chapter 2, we looked at the effect of the oxide substrate on the gold nanoparticles during the oxygen reduction reaction. TiO_2 nanoparticles were synthesized using a two phase high-pressure/high-temperature method and then SiO_2 nanoparticles were synthesized using sonication. After both substrates were synthesized, gold nanoparticles were deposited onto the supports by using photoreduction. All of the characterization methods showed that the support played a role in the electron-transfer properties of gold. Raman showed a new peak that was only present in the TiO_2-supported samples for the Ti^{3+} signal. EPR showed a signal for the oxygen vacancies that was only present in TiO_2. XPS showed a charge transfer from Au to SiO_2 and then TiO_2 gold. Finally, when testing ORR activity the TiO_2 based

samples proved to have the best activity showing that TiO_2 is the optimal support for ORR because of the defects present.

In Chapter 3, we looked at manipulating the concentration of defects in TiO_2 and seeing how that impacts the electrocatalytic activity for the ORR. TiO_2 was synthesized using the same two-phase high-pressure/high temperature method. Then the gold was deposited onto the TiO_2 by using a wet chemical reduction method. Finally, the concentration of oxygen vacancies was controlled by adding increasing amounts of ascorbic acid and heating it with the Au/TiO_2 nanocomposites hydrothermally. Structurally speaking, the defect concentration does not change the bulk structure. However, by EPR, we could see a direct correlation by adding more ascorbic acid the oxygen vacancy signal increased, meaning the concentration of defects increased as more ascorbic acid is added. When testing the electrocatalytic activity, as the amount of defects increased, the electrocatalytic activity for the ORR showed a volcanic-like behavior. This is because as the amount of defects increased, the binding energy of oxygen onto the TiO_2 increased, but it reached a point where the binding energy of oxygen was too much and therefore decreased the electrocatalytic activity.

Finally, in Chapter 4, the different kinds of doping in nitrogen and their effect on the activity towards the oxygen reduction reaction was studied. $N\text{-}TiO_2$ nanoparticles were synthesized using a sol-gel method. As a control TiO_2 nanoparticles were made using the same method, but the nitrogen source was not added. Then the gold was deposited onto the TiO_2 and $N\text{-}TiO_2$ using the same wet-chemical reduction

method as before. Then the Au/N-TiO_2 was heated hydrothermally at different temperatures with the same amount of ascorbic acid. XRD and UV-Vis measurements showed that the nitrogen doping had a more defective bulk structure. The temperature change did not seem to affect the overall bulk structure. What we were hoping to see is that the temperature change would actually affect the kinds of nitrogen doping and be a way to control the different amounts. However, the XPS showed that all of the nitrogen doping was the same throughout the samples and there was no general trend in charge transfer. ORR activity of the N-TiO_2-supported gold nanoparticles had the best activity, but we couldn't figure out why.

6.3 Future Work for Looking at Defects in Au/TiO_2

6.3.1 Better Control of Au deposition

One of the advantages of depositing the gold directly onto the TiO_2 is that there is no need for a ligand in the synthesis. The use of ligands allows for size control of the particles, however, the particle surface is not bare and the ligand has to be removed so that the active species can access the surface. In most cases, the ligand is removed by electrochemical cycling, but the particle size and surface and thus change. Here, we can deposit the nanoparticles directly on the TiO_2, but the size is so hard to control. What an area would be is looking into other methods to control the size of the gold particles and the dispersity on the substrate and that affects the defects.

6.3.2 Use of Nanoclusters or Single Atoms

Our lab has done a previous study where the size of gold was changed and the effect on the ORR. It was found that as the size decreases, the activity increases. In the future, it would be interesting to try and deposit gold nanoclusters or single atoms onto the TiO_2 and see their interaction with the oxygen vacancies.

6.3.3 Other types of doping

Doping provides interesting properties for the TiO_2. It would be interesting to look at the different types of doping for example sulfur or carbon doping.

6.3.4 Controlled studies with the use of carbon

Currently, Pt has not been able to be replaced as the catalyst for the ORR. Therefore, we need to start creating more complex molecules with multiple active sites. Au/TiO_2 can provide a start in this area because the active site is at the interface between the TiO_2 and gold. Utilizing carbon as well is helpful because it can also provide more conductivity.

6.4 Summary of CO Electrooxidation of TiO_xN_y

In this study, TiN powder was heated in oxygen at the same temperature for different amounts of time. This allowed for the oxidation of the TiN. After this, Ag nanoparticles were deposited on the different TiO_xN_y using a wet-chemical reduction method. TEM, XRD, and XPS revealed that only the surface of the powder was oxidized by showing TiO_2 signals, but the bulk of the material was TiN. There seemed

to be an apparent charge transfer from the Ag to the TiN. When comparing the electrooxidation of carbon dioxide there seemed to be an apparent trend whereas the oxidation time increased, there was a volcanic behavior for CO electrooxidation.